The Astrophysical Journal Letters, 969:L2 (32pp), 2024 July 1 https://doi.org/10.3847/2041-8213/ad4495

The Complete CEERS Early Universe Galaxy Sample: A Surprisingly Slow Evolution of the Space Density of Bright Galaxies at $z \sim 8.5$–14.5

Steven L. Finkelstein[1], Gene C. K. Leung[1], Micaela B. Bagley[1], Mark Dickinson[2], Henry C. Ferguson[3], Casey Papovich[4,5], Hollis B. Akins[1], Pablo Arrabal Haro[2], Romeel Davé[6,7], Avishai Dekel[8], Jeyhan S. Kartaltepe[9], Dale D. Kocevski[10], Anton M. Koekemoer[3], Nor Pirzkal[11], Rachel S. Somerville[12], L. Y. Aaron Yung[3,13,44], Ricardo O. Amorín[14,15], Bren E. Backhaus[16], Peter Behroozi[17,18], Laura Bisigello[19,20], Volker Bromm[1], Caitlin M. Casey[1], Óscar A. Chávez Ortiz[1], Yingjie Cheng[21], Katherine Chworowsky[1,43], Nikko J. Cleri[4,5], M. C. Cooper[22], Kelcey Davis[16], Alexander de la Vega[23], David Elbaz[24], Maximilien Franco[1], Adriano Fontana[25], Seiji Fujimoto[26,27], Mauro Giavalisco[21], Norman A. Grogin[3], Benne W. Holwerda[28], Marc Huertas-Company[29,30,31], Michaela Hirschmann[32], Kartheik G. Iyer[33], Shardha Jogee[1], Intae Jung[34], Rebecca L. Larson[1,43], Ray A. Lucas[34], Bahram Mobasher[23], Alexa M. Morales[1], Caroline V. Morley[1], Sagnick Mukherjee[35], Pablo G. Pérez-González[36], Swara Ravindranath[13,37], Giulia Rodighiero[20,38], Melanie J. Rowland[1], Sandro Tacchella[39,40], Anthony J. Taylor[1], Jonathan R. Trump[16], and Stephen M. Wilkins[41,42]

[1] Department of Astronomy, The University of Texas at Austin, Austin, TX 78712, USA; stevenf@astro.as.utexas.edu
[2] NSF's National Optical-Infrared Astronomy Research Laboratory, 950 N. Cherry Ave., Tucson, AZ 85719, USA
[3] Space Telescope Science Institute, Baltimore, MD 21218, USA
[4] Department of Physics and Astronomy, Texas A&M University, College Station, TX 77843-4242 USA
[5] George P. and Cynthia Woods Mitchell Institute for Fundamental Physics and Astronomy, Texas A&M University, College Station, TX 77843-4242, USA
[6] Institute for Astronomy, University of Edinburgh, Blackford Hill, Edinburgh, EH9 3HJ, UK
[7] Department of Physics and Astronomy, University of the Western Cape, Robert Sobukwe Rd, Bellville, Cape Town 7535, South Africa
[8] Racah Institute of Physics, The Hebrew University of Jerusalem, Jerusalem 91904, Israel
[9] Laboratory for Multiwavelength Astrophysics, School of Physics and Astronomy, Rochester Institute of Technology, 84 Lomb Memorial Drive, Rochester, NY 14623, USA
[10] Department of Physics and Astronomy, Colby College, Waterville, ME 04901, USA
[11] ESA/AURA Space Telescope Science Institute, USA
[12] Center for Computational Astrophysics, Flatiron Institute, 162 5th Avenue, New York, NY 10010, USA
[13] Astrophysics Science Division, NASA Goddard Space Flight Center, 8800 Greenbelt Rd., Greenbelt, MD 20771, USA
[14] ARAID Foundation, Centro de Estudios de Física del Cosmos de Aragón (CEFCA), Unidad Asociada al CSIC, Plaza San Juan 1, E–44001 Teruel, Spain
[15] Departamento de Astronomía, Universidad de La Serena, Av. Juan Cisternas 1200 Norte, La Serena 1720236, Chile
[16] Department of Physics, 196 Auditorium Road, Unit 3046, University of Connecticut, Storrs, CT 06269, USA
[17] Department of Astronomy and Steward Observatory, University of Arizona, Tucson, AZ 85721, USA
[18] Division of Science, National Astronomical Observatory of Japan, 2-21-1 Osawa, Mitaka, Tokyo 181-8588, Japan
[19] Dipartimento di Fisica e Astronomia "G.Galilei," Universitá di Padova, Via Marzolo 8, I-35131 Padova, Italy
[20] INAF–Osservatorio Astronomico di Padova, Vicolo dell'Osservatorio 5, I-35122, Padova, Italy
[21] University of Massachusetts Amherst, 710 North Pleasant Street, Amherst, MA 01003-9305, USA
[22] Department of Physics & Astronomy, University of California, Irvine, 4129 Reines Hall, Irvine, CA 92697, USA
[23] Department of Physics and Astronomy, University of California, 900 University Ave., Riverside, CA 92521, USA
[24] Université Paris-Saclay, Université Paris Cité, CEA, CNRS, AIM, 91191, Gif-sur-Yvette, France
[25] INAF—Osservatorio Astronomico di Roma, via di Frascati 33, 00078 Monte Porzio Catone, Italy
[26] Cosmic Dawn Center (DAWN), Jagtvej 128, DK2200 Copenhagen N, Denmark
[27] Niels Bohr Institute, University of Copenhagen, Lyngbyvej 2, DK2100 Copenhagen Ø, Denmark
[28] Physics & Astronomy Department, University of Louisville, Louisville, KY 40292 USA
[29] Instituto de Astrofísica de Canarias, La Laguna, Tenerife, Spain
[30] Universidad de la Laguna, La Laguna, Tenerife, Spain
[31] Université Paris-Cité, LERMA—Observatoire de Paris, PSL, Paris, France
[32] Institute of Physics, Laboratory of Galaxy Evolution, Ecole Polytechnique Fédérale de Lausanne (EPFL), Observatoire de Sauverny, 1290 Versoix, Switzerland
[33] Dunlap Institute for Astronomy & Astrophysics, University of Toronto, Toronto, ON M5S 3H4, Canada
[34] Space Telescope Science Institute, 3700 San Martin Drive, Baltimore, MD 21218, USA
[35] Department of Astronomy and Astrophysics, University of California, Santa Cruz, CA 95064, USA
[36] Centro de Astrobiología (CAB), CSIC-INTA, Ctra. de Ajalvir km 4, Torrejón de Ardoz, E-28850, Madrid, Spain
[37] Center for Research and Exploration in Space Science and Technology II, Department of Physics, Catholic University of America, 620 Michigan Ave. NE, Washington, DC 20064, USA
[38] Department of Physics and Astronomy, Università degli Studi di Padova, Vicolo dell'Osservatorio 3, I-35122, Padova, Italy
[39] Kavli Institute for Cosmology, University of Cambridge, Madingley Road, Cambridge, CB3 0HA, UK
[40] Cavendish Laboratory, University of Cambridge, 19 JJ Thomson Avenue, Cambridge, CB3 0HE, UK
[41] Astronomy Centre, University of Sussex, Falmer, Brighton BN1 9QH, UK
[42] Institute of Space Sciences and Astronomy, University of Malta, Msida MSD 2080, Malta
Received 2023 November 4; revised 2024 February 28; accepted 2024 March 19; published 2024 June 20

[43] NSF Graduate Fellow.
[44] NASA Postdoctoral Fellow.

Abstract

We present a sample of 88 candidate $z \sim 8.5$–14.5 galaxies selected from the completed NIRCam imaging from the Cosmic Evolution Early Release Science survey. These data cover ∼90 arcmin^2 (10 NIRCam pointings) in six broadband imaging filters and one medium-band imaging filter. With this sample we confirm at higher confidence early JWST conclusions that bright galaxies in this epoch are more abundant than predicted by most theoretical models. We construct the rest-frame ultraviolet luminosity functions at $z \sim 9$, 11, and 14 and show that the space density of bright ($M_{\rm UV} = -20$) galaxies changes only modestly from $z \sim 14$ to $z \sim 9$, compared to a steeper increase from $z \sim 8$ to $z \sim 4$. While our candidates are photometrically selected, spectroscopic follow-up has now confirmed 13 of them, with only one significant interloper, implying that the fidelity of this sample is high. Successfully explaining the evidence for a flatter evolution in the number densities of UV-bright $z > 10$ galaxies may thus require changes to the dominant physical processes regulating star formation. While our results indicate that significant variations of dust attenuation with redshift are unlikely to be the dominant factor at these high redshifts, they are consistent with predictions from models that naturally have enhanced star formation efficiency and/or stochasticity. An evolving stellar initial mass function could also bring model predictions into better agreement with our results. Deep spectroscopic follow-up of a large sample of early galaxies can distinguish between these competing scenarios.

Unified Astronomy Thesaurus concepts: Early universe (435); Galaxy formation (595); Galaxy evolution (594); Luminosity function (942)

Supporting material: figure sets, machine-readable tables

1. Introduction

The first 500 million years of cosmic time ($z \gtrsim 10$), when the first stars and galaxies formed, began to grow, and kick-started the process of reionization, was largely hidden from view until recently. The depth achievable with JWST near-infrared imaging, along with the capability to deeply probe beyond ∼1.6 μm for the first time, was expected to revolutionize our understanding of this early epoch. As soon as the first data from JWST were released in 2022 July, this renaissance in our understanding unfolded immediately.

Prior to JWST, the high-redshift community had debated about the evolution of the rest-frame ultraviolet (UV) luminosity function (and, by extension, the cosmic star formation rate (SFR) density) at $z > 8$. While there was good agreement that these quantities evolved smoothly downward from $z = 4$ to $z = 8$ (e.g., Bouwens et al. 2015; Finkelstein et al. 2015), results differed at $z > 8$, with some advocating for continued evolution with the same declining slope from lower redshifts (e.g., Finkelstein 2016; McLeod et al. 2016), while others claimed evidence of an accelerated decline toward higher redshifts (e.g., Oesch et al. 2018; Bouwens et al. 2019). Early JWST surveys, including the Cosmic Evolution Early Release Science Survey (CEERS; PID 1345, PI Finkelstein) and the GLASS (PID 1324, PI Treu) survey, were designed in part to determine which of these evolutionary possibilities was correct.

In defiance of expectations, several studies immediately reported the presence of bright ($m \lesssim 27.5$) galaxies at $z > 10$ from the CEERS and GLASS surveys (e.g., Finkelstein et al. 2022b; Naidu et al. 2022b; Castellano et al. 2022; Donnan et al. 2023a). These galaxies were both brighter and at higher redshifts than expected from these early surveys, which were neither extremely wide nor extremely deep. While some early results changed owing to the uncertain characterization of the NIRCam photometric zero-point (Boyer et al. 2022), within a few months more robust samples of galaxies were in place (e.g., Harikane et al. 2023a; Finkelstein et al. 2023; McLeod et al. 2024).

These first studies with larger samples (∼20 objects) agreed that the abundance of $z \gtrsim 10$ galaxies was in excess of both theoretical and empirical predictions, with explanations including an evolving initial mass function (IMF), changes in star formation efficiency (SFE), changes in dust attenuation, contribution from active galactic nuclei (AGNs), rampant sample contamination (e.g., Mason et al. 2023; Harikane et al. 2023a; Dekel et al. 2023; Ferrara et al. 2023; Finkelstein et al. 2023), and even changes to the underlying cosmology (e.g., Boylan-Kolchin 2023; Liu & Bromm 2022). Such explanations are compelling, yet these early data sets spanned small dynamic ranges in UV luminosity, with few galaxies yet included.

Here we report the results from a search for $z \geqslant 8.5$ galaxies over the completed CEERS data set. This follows on the work of Finkelstein et al. (2023, hereafter F23), who did a similar search, finding 26 galaxies over the first four CEERS pointings. Importantly, here we combine our results with those from Leung et al. (2023), who used a near-identical analysis procedure to identify a sample of 38 galaxies at similarly high redshift from the deep Next Generation Deep Extragalactic Exploratory Public (NGDEEP; Bagley et al. 2024b) survey NIRCam imaging, extending our dynamic range 1.5 mag fainter.

In Section 2 we describe our imaging data set and give a detailed explanation of our photometry procedure, which has evolved from F23 to increase our color and flux accuracy. In Section 3 we outline our photometric redshift sample selection procedure and discuss the available spectroscopy for our candidate galaxies. Our results are presented in Section 4; in Section 4.2 we compare the observed surface density of galaxies to prelaunch predictions, and in Section 4.3 we calculate the rest-UV luminosity functions at $z \sim 9$, 11, and 14. We discuss these results in the context of a variety of more recent simulation predictions in Section 5, and we present our conclusions in Section 6. We assume the latest Planck flat ΛCDM cosmology with $H_0 = 67.36$ km s^{-1} Mpc^{-1}, $\Omega_m = 0.3153$, and $\Omega_\Lambda = 0.6847$ (Planck Collaboration et al. 2020). All magnitudes are in the absolute bolometric system (AB; Oke & Gunn 1983).

2. Data

The CEERS NIRCam imaging survey consists of 10 NIRCam pointings in the CANDELS Extended Groth Strip

(EGS) field, done in parallel with prime MIRI and NIRSpec observations. These data were taken in two epochs. On 2022 June 21–22 four NIRCam pointings were obtained (known as pointings NIRCam 1, 2, 3, and 6; results presented in F23). The remaining six pointings (NIRCam 4, 5, 7, 8, 9, and 10) were completed on 2022 December 20–24. All 10 pointings include the same filter coverage of F115W, F150W, and F200W in the short-wavelength channel and F277W, F356W, F410M, and F444W in the long-wavelength channel. In this analysis we make use of the official CEERS publicly released mosaics (DR0.5 for the June data and DR0.6 for the December data). These images are available on the CEERS website (https://ceers.github.io/releases.html) and on MAST as High Level Science Products via 10.17909/z7p0-8481.

2.1. Data Reduction

We reduce the NIRCam imaging following the procedures outlined in Bagley et al. (2023), which we briefly summarize here. We use the JWST Calibration Pipeline (Bushouse et al. 2022) with custom modifications and additional steps needed to remove features such as snowballs, wisps, and $1/f$ noise. Our reduction process is the same for all images, though we use different Pipeline and Calibration Reference Data System (CRDS) versions for the two epochs of CEERS NIRCam imaging: Pipeline version 1.7.2 and CRDS context 0989 for the Epoch 1 images (CEERS DR0.5, obtained in 2022 June, and including pointings NIRCam 1, 2, 3, and 6), and Pipeline version 1.8.5 and CRDS context 1023 for the Epoch 2 images (CEERS DR0.6, obtained in 2022 December, and including pointings NIRCam 4, 5, 7, 8, 9, and 10). There were no major changes between these pipeline+CRDS versions that we would expect to affect the photometry.

For our astrometric alignment and analysis we make use of the archival Hubble Space Telescope (HST) imaging from the All-wavelength Extended Groth Strip International Survey (AEGIS; Davis et al. 2007), the Cosmic Assembly Deep Extragalactic Legacy Survey (CANDELS; Grogin et al. 2011; Koekemoer et al. 2011), and the 3D-HST (Momcheva et al. 2016) survey. The entire CEERS field is covered by F606W, F814W, F125W, F140W, and F160W; portions are covered by F105W (we note that the F140W imaging is very shallow [800 s]; thus, while we include it in our catalog, we do not include these data in any figures below). We use the CEERS v1.9[45] HST EGS mosaics, which are created from these data sets, aligned to Gaia DR3, and on a 30 mas pixel scale. We use a modified version of the `TweakReg` routine to align the images, using the HST F160W mosaic as the astrometric reference in all pointings except NIRCam 3 and 9. In these two pointings, a low-level guide star tracking issue in the HST imaging caused a sub–point-spread function (PSF) shift across a portion of the F160W mosaic, and so we use the NIRCam F277W (pointing 3) and F356W (pointing 9) mosaics as the absolute references. In all pointings, the rms of the relative, NIRCam-to-NIRCam astrometry is ∼5–10 mas.

We create mosaics on a 30 mas pixel scale in all filters and extract smaller cutouts of the HST mosaics to match the footprints of the drizzled NIRCam images, providing pixel-aligned imaging in up to 13 filters per field from ∼0.5 to 5 μm. Finally, we perform a global, two-dimensional background subtraction on the mosaics to remove any residual background variations. This method first performs a tiered source detection to identify progressively smaller sources in each filter. Then, the source masks in each filter, including all available HST images, are combined into a single merged mask such that pixels with source flux identified in any filter are excluded when measuring the background. See Bagley et al. (2023) and F23 for more information on the background method and details on the method's performance in CEERS images.

2.2. Photometry

We perform photometry on all 10 CEERS fields using SExtractor (Bertin & Arnouts 1996). Photometry is performed on each of the 10 pointings independently (the high-redshift galaxy sample is screened for duplicates in the small overlapping areas, as discussed below). The photometry process here is similar to that in F23, with some key differences designed to improve the photometric validity, as described below. Our fiducial photometry is measured in elliptical Kron apertures, using a Kron factor = 1.1 and a minimum radius = 1.6, following F23. These small Kron apertures result in optimal signal-to-noise ratio (S/N). We derive accurate colors in these apertures by matching the image PSFs between different filters, and we calculate accurate total fluxes via a two-step simulation-based aperture correction process.

2.2.1. PSF Matching

We create empirical PSFs in each filter by stacking stars. We select stars by identifying the stellar locus in a plot of half-light radius versus magnitude in a preliminary SExtractor run in each filter. Each star is then inspected to ensure that it appears to be a nonsaturated point source in a noncrowded region. We make a single PSF per filter by stacking stars across all 10 pointings (as all observations used the same dither pattern). For each star, we extract a 101 × 101 pixel box, upsample by a factor of 10, measure the centroid, and shift the star to be centered in this upsampled image. We then downsample back to the native resolution, rotate the star by a random position angle (to account for situations when the position angle of the observations was not identical), and normalize the star's peak flux to unity. The final PSF is made by median-combining the individual stars. The final PSFs have a centroiding accuracy of ∼0.05–0.1 pixels.

We then use these PSFs to derive kernels to match the PSFs in images with PSF FWHMs smaller than that of F277W to the F277W PSF. This includes the NIRCam F115W, F150W, and F200W images and the HST/Advanced Camera for Surveys (ACS) F606W and F814W images. Kernels were created with the `PYPHER` Python routine[46] (Boucaud et al. 2016). The NIRCam F356W, F410M, and F444W filters, along with all four HST/WFC3 filters, F105W, F125W, F140W, and F160W, have PSF FWHMs larger than that of the NIRCam F277W filter. To correct for missing flux when performing aperture photometry on these larger PSF images, we first convolve the F277W image to match the PSF of a given larger PSF image and then derive source-specific correction factors as the ratio of the F277W flux prior to convolution to that after convolution (where the larger PSF images will have less flux in the aperture). These correction factors are then applied to photometry measured on the larger PSF images, to account

[45] ceers.github.io/releases.html#hdr1

[46] https://pypher.readthedocs.io

for the missing flux. We tested our PSF-matching process by measuring curves of growth of the PSF stars in the images, finding that the median enclosed flux at an aperture diameter of 0.″3 was within 5% (and often less) of the F277W value for all filters.

In F23 we did not employ these correction factors, as we matched all NIRCam bands to the F444W PSF. However, by matching here to the smaller-PSF F277W image, we better optimize S/N by not smoothing to the largest PSF. Additionally, as the HST/WFC3 images have larger PSFs than even F444W, in F23 we devised correction factors by comparing the HST fluxes to previous HST catalogs. Our updated method here is independent of other catalogs and is thus more self-consistent. We confirm that our fluxes here are consistent to within 5% on average (and often lower) with the fluxes from F23.

2.2.2. Catalog Creation

We use the inverse-variance-weighted sum of the non-PSF-matched F277W and F356W images as our detection image, to better detect faint sources. Using this detection image, we run SExtractor cycling through the seven NIRCam images and six HST images as the measurement image. The key SExtractor parameters were DETECT_THRESH = 1.4, DETECT_MINAREA = 5 pixels, and a top-hat convolution kernel with a width of 4 pixels, similar to F23. We force SExtractor to skip the background subtraction step, as this was previously removed (Section 2.1). We use MAP_RMS for the source weighting. As the pipeline-produced flux error (ERR) images include Poisson noise, they are not appropriate for source detection. We thus convert the weight map associated with the detection image into an effective rms map by taking 1/sqrt(WHT), and we assign this to the detection image. For the measurement image, we use the pipeline ERR image.

We estimate an aperture correction to the total flux for these small apertures by performing a second run of SExtractor on the F277W image with the Kron parameters set to the default "MAG_AUTO" parameters of (2.5, 3.5), deriving an aperture correction as the ratio between the flux in this larger aperture and that in the smaller aperture for each object in the F277W catalog, which we then applied multiplicatively to the fluxes and uncertainties for all filters (thereby correcting fluxes to an estimated total, but not changing colors or S/N values).

As several previous studies have noted that the default Kron parameters we use for this aperture correction can miss light in the wings of the PSF (e.g., Bouwens et al. 2015; Finkelstein et al. 2022a), we estimate residual aperture corrections using source injection simulations, adding 3000 mock sources to our real images in each field. We add sources from $m = 22$–28.5 mag (to ensure a robust photometric measurement), with a lognormal half-light radius distribution peaking at ∼1.5 pixels (∼0.2 kpc at $z = 10$; compact but modestly resolved, comparable to high-redshift sources) and a lognormal Sérsic parameter distribution peaking at 1.2. These mock sources were generated with GALFIT (Peng et al. 2002) and added at random positions to the F277W and F356W images. In GALFIT, the total flux is calculated such that half the flux is within r_e. We combined the two images to create a detection image, ran SExtractor in the same way as on our real data to generate a F277W catalog, and estimated residual aperture corrections as the ratio of input to recovered fluxes for recovered sources. While in F23 we derived a single factor, here we note that the residual correction needed is magnitude dependent. We thus fit a linear function to the flux ratios as a function of magnitude over $24 < m < 28$, finding a correction ranging from ∼2% at $m < 22$ to ∼20% at $m = 28$. We performed this linear fitting in each field, applying these residual aperture corrections to every source (placing a bound on the corrections applied to be from 1.0 to 1.2). We note that in the magnitude range of $25 < m < 26$ used by F23 we see a similar correction factor (1.08) to the one they derived.

2.2.3. Flux Uncertainties

We derive flux uncertainties empirically based on the number of pixels in an aperture. We fit for the noise as a function of aperture size by measuring the fluxes in circular apertures with 30 different diameters, ranging from 0.″1 (3.33 pixels) to 3″ (100 pixels). We place nonoverlapping apertures randomly, avoiding pixels with zero values in the error image, and positive values in the segmentation map. We do this in two iterations, placing 3000 apertures with diameters <1.″5 and 500 apertures with larger diameters. We measure fluxes at these positions in all aperture sizes, calculating the 1σ noise in each aperture size by measuring the median absolute deviation of the measured flux values (multiplying by 1.48 to convert to a Gaussian-like standard deviation). Finally, we fit a curve to the noise in a given aperture as a function of pixels in that aperture, using the following equation (Gawiser et al. 2006):

$$\sigma_N = \sigma_1(\alpha N^{\beta} + \gamma N^{\delta}), \quad (1)$$

where σ_N is the noise in an aperture containing N pixels and σ_1 is the pixel-to-pixel noise measured in each image as the sigma-clipped standard deviation of all nonobject pixels (see Figure 3 in Finkelstein et al. 2022a for an example of this process). Compared to F23, here we include the second term in parentheses, as we find a better fit to the data. We fit the four free parameters with an IDL implementation of EMCEE (see Finkelstein et al. 2019 for details), taking the median of the posterior as our fiducial values.

We use these functional form fits for each filter to calculate the photometric uncertainties for each object, using both the number of pixels in its Kron aperture (Area = πab, where the semimajor [minor] axis a [b] is equal to the A[B]_IMAGE keywords multiplied by the KRON_RADIUS value) and the area value for a given circular aperture. We scale these values by the ratio of the error image value at the central position of a given source to the median error value of the whole map, thereby allowing the noise to be representative of the noise level around a given galaxy. We refer to these measurements as our "global" noise measurements, which we use as our fiducial value. Finally, to account for variable image noise not captured by the error image value at the central pixel, for each object in our catalog we also calculate a "local" noise measurement. This local noise was calculated in apertures with 0.″2, 0.″3, 0.″4, and 0.″5 diameters, measured as 1.48 times the median absolute deviation of the flux distribution in the 200 closest apertures from the above process.

2.2.4. Multiband Catalog

For each object in the catalog we use astropy.wcs WCS_PIX2WORLD to derive celestial coordinates from the SExtractor x, y positions (SExtractor cannot currently parse the world coordinate system in the JWST data model image headers). We calculate physical fluxes by applying a photometric zero-point to convert the image from MJy sr^{-1} to erg

Table 1
NIRCam Imaging Summary

Field	F115W	F150W	F200W	F277W	F356W	F410M	F444W
CEERS1	29.06	28.91	29.13	29.13	29.13	28.32	28.58
CEERS2	29.04	28.92	29.12	29.13	29.14	28.32	28.56
CEERS3	29.18	29.01	29.16	29.16	29.15	28.37	28.57
CEERS4	29.16	29.02	29.18	29.15	29.13	28.31	28.51
CEERS5	29.37	29.02	29.16	29.15	29.43	28.32	28.50
CEERS6	29.19	29.00	29.15	29.17	29.15	28.38	28.60
CEERS7	29.43	29.04	29.17	29.14	29.41	28.31	28.50
CEERS8	29.43	29.02	29.14	29.16	29.42	28.32	28.52
CEERS9	29.55	28.96	29.16	29.15	29.37	28.31	28.76
CEERS10	29.20	29.00	29.13	29.04	29.12	28.34	28.50
Median	29.20	29.01	29.16	29.15	29.15	28.32	28.56
PSF FWHM	0.″068	0.″072	0.″080	0.″128	0.″143	0.″156	0.″163
Flux Enclosed	0.776	0.775	0.742	0.625	0.574	0.537	0.513

Note. The depths given represent 5σ limiting magnitudes, measured in $d = 0.''2$-diameter circular apertures and corrected to total fluxes assuming a point source. The PSF FWHM and fraction of the flux enclosed in a $0.''2$-diameter circular aperture are given below the horizontal line.

s^{-1} cm^{-2} Hz^{-1}, and we apply both aperture corrections derived above to all flux and flux error estimates. We correct for Galactic extinction using an $E(B-V)$ of 0.006 for the EGS field and a Cardelli et al. (1989) Milky Way attenuation curve.

We create a multiband catalog from the individual-filter catalogs created by SExtractor, including our fiducial Kron apertures and fluxes measured in circular apertures with diameters ranging from $0.''05$ to $2.''0$. For the latter we include fluxes measured from both the PSF-matched and native-resolution images; the latter are used below as a measure of detection significance. These circular apertures are corrected for Galactic attenuation but not corrected to total, as we will use them solely for detection significance. For all flux measurements we calculate the noise per source following the above methods. We flag any sources that had either a zero or NaN in any error column, replacing their flux error with 10^{12} nJy (several orders of magnitude larger than any real source error) such that these flux measurements do not impact any analysis. The final catalog contains only objects with valid measurements in the six broadband filters, excluding the short-wavelength chip gaps, covering a total area of 88.1 $arcmin^2$.

In Tables 1 and 2, we include an estimate of the limiting 5σ magnitude for our catalog. To calculate this, we use the noise functions described above to derive the flux density uncertainty in an aperture of diameter $0.''2$. We then measure the enclosed flux at this radius from the stacked PSF. We then divide the flux uncertainty by the enclosed fraction of flux to estimate the total noise for a point source. Finally, we multiply this value by 5 and convert to an AB magnitude. This final multiband catalog was known as "v0.51" internally to the CEERS team and has been used in a variety of analyses (e.g., Arrabal Haro et al. 2023b; Vega-Ferrero et al. 2024; Arrabal Haro et al. 2023a; Larson et al. 2023a; Ronayne et al. 2023).

3. Sample Selection

3.1. Photometric Redshifts

The final photometric catalog contains 101,808 sources across the entire CEERS field (86.8% of which have S/N greater than 3 in F277W). We create a new numerical identifier as an ascending integer starting at 1 in CEERS1, adding in each field sequentially. We measure photometric redshifts for all sources in our 13-band photometric catalog using EAZY (Brammer et al. 2008). We perform three iterations of EAZY: (1) *fiducial*: using our fiducial Kron, aperture-corrected photometry with a maximum redshift of 20; (2) *low-z*: the same as the fiducial run, but with the maximum redshift set to 7 (allowing visualization of the best-fitting low-redshift model); and (3) *circular*: replacing the Kron fluxes with the flux measured in $d = 0.''2$-diameter apertures, with a maximum redshift of 20 (see Section 3.2.2).

Table 2
HST Imaging Summary

Filter	5σ Limiting Magnitude	FWHM	PSF Enclosed ($d = 0.''2$)
ACS F606W	28.73	0.″118	0.696
ACS F814W	28.50	0.″124	0.625
WFC3 F105W	27.28	0.″235	0.348
WFC3 F125W	27.32	0.″244	0.327
WFC3 F140W	26.66	0.″247	0.317
WFC3 F160W	27.38	0.″254	0.303

Note. Similar to Table 1, but for the HST imaging used. All depths given represent 5σ limiting magnitudes, measured in $d = 0.''2$-diameter circular apertures and corrected to total fluxes assuming a point source.

EAZY fits nonnegative linear combinations of user-supplied templates to derive probability distribution functions (pdf's) for the redshift, based on the quality of fit of the various template combinations to the observed photometry for a given source. We use the same customized template list as F23, including the 12 FSPS (Conroy & Gunn 2010) templates in the recommended "tweak_fsps_QSF_12_v3" set, supplemented with six templates created by Larson et al. (2023b) to span the blue colors expected for early galaxies. We assume a flat prior in luminosity, include a systematic error of 5% of the observed flux values, and fit to our measured total flux and flux error values.

3.2. Selection Criteria

Here we describe the selection criteria we use to identify candidate $z > 8.5$ galaxies. Following our previous work (Finkelstein et al. 2010, 2015, 2022b, 2022a, 2023), we use a

combination of flux detection significance values and quantities derived from the full photometric redshift pdf, denoted $\mathcal{P}(z)$, to select our galaxy sample. We also make use of the peak $\mathcal{P}(z)$ redshift, denoted $z_{\rm best}$. All S/Ns, unless stated otherwise, are measured in 0.″2-diameter apertures in the native-resolution (non-PSF-matched) images. We note that while we primarily use the global empirical noise measurement, we also make use of the local noise measurements with slightly relaxed criteria as described below.

We also make use of S/N criteria in filters blueward of the Lyα break ("dropout" filters, which should contain no significant flux). To identify these filters, for each object we first zero out the $\mathcal{P}(z)$ at $z<7.5$ such that any low-redshift solution does not impact the dropout filter choice (followed by renormalizing the $\mathcal{P}[z]$). We then consider a filter to be a dropout filter if the wavelength corresponding to the red side of the filter transmission's FWHM is less than the observed Lyα wavelength at the 16th percentile of the renormalized $\mathcal{P}(z)$. In this way we make use of the full $\mathcal{P}(z)$ when calculating which bands should be considered a dropout filter. Here we list our selection criteria, separated into two categories:

Detection Significance Criteria:

1. Detection S/N: S/N $>$ 5.5 ($>$5.0) in at least two of the F150W, F200W, F277W, F356W, or F444W filters, using the global (local) empirical noise measurements.
2. Dropout S/N: S/N $<$ 2.0 (3.0) in all bands fully blueward of the Lyα break, and no more than one filter with S/N $>$ 1.5 (2.0), using the global (local) empirical noise measurements. For this we consider the ACS F606W and F814W filters and the NIRCam F115W, F150W, and F200W filters (we note that some candidates have $\sim$1σ–3σ flux measurements in WFC3 bands nominally below the Lyα break; however, we consider these spurious, as such objects show significant non-detections in the deeper, short-wavelength NIRCam bands).
3. Error-map values at the central pixel of the object $<$1000 in the F115W, F150W, F200W, and F277W filters. This ensures valid flux measurements in a minimum set of filters to robustly select $z>9$ galaxies (and explicitly excludes the NIRCam short-wavelength chip gaps).
4. Total F277W magnitude $\leqslant$29.2 as a conservative estimate to limit low-significance sources.

Photometric Redshift Criteria:

1. $\int \mathcal{P}(z>7) \geqslant 0.7$, requiring at least 70% of the integrated $\mathcal{P}(z)$ at $z>7$.
2. $z_{\rm best} > 8.5$.
3. $\mathcal{S}_z \geqslant 9$, where $\mathcal{S}_z$ is calculated as the unit redshift where the integral in a $z\pm0.5$ bin is the maximum compared to all other unit redshift bins.
4. Total $\chi^2 \leqslant 60$ (for the 13 available bands).
5. $\Delta\chi^2 > 4$, calculated as the difference between the lowest χ^2 value at $z<7$ and the best-fitting χ^2 value.

These criteria are very similar to those in F23, with the key differences being the selection of dropout bands, the more conservative S/N <2 dropout criteria (compared to S/N <3 in F23), and the addition of the local noise measurements.

The combination of these sample selection criteria yielded an initial sample of 185 $z>8.5$ galaxy candidates across the full CEERS field. We visually inspected all objects (examining cutout images in all filters, as well as the photometric spectral energy distribution (SED) and the $\mathcal{P}(z)$ curves) to identify any spurious sources, or potential cases where the SExtractor photometry could be questionable (e.g., the presence of a bright neighbor). We removed 91 objects through this screening process. Cutout images for all removed objects, as well as a table of their positions, are shown in Appendix B.

Objects were removed for a variety of reasons, but the vast majority (78/91) were sources of an obvious spurious nature, including 10 sources identified as diffraction spikes, 45 sources associated with image edges, and 23 sources identified as bad pixels. The last had a characteristic observational signature of a compact (few pixel), boxy morphology in the long-wavelength channel images only. We note that a few of our removed bad-pixel sources appear slightly less boxy than the bulk. It is possible that these are real astrophysical objects at $z\gtrsim16$ (where the Lyα break would be redward of F200W). However, as they are visible in the three long-wavelength channels only, it is much more plausible (if indeed they are not bad pixels) that they are faint objects associated with the known $z\sim4.9$ overdensity in this field (Arrabal Haro et al. 2023b), or low-redshift dusty galaxies (e.g., Bisigello et al. 2023), rather than true $z\sim16$ galaxies. Improved outlier pixel rejection in future iterations of our data reduction could reduce the frequency of such objects. Likewise, use of the context map ("CON") extension of the JWST data model could remove the need to manually identify image edges. We do note that in some cases objects removed owing to image edges have legitimate long-wavelength photometry but are adjacent to a short-wavelength chip gap.

The remaining 13 sources were a combination of objects identified as being associated with nearby bright galaxies, inadvertently split into separate objects by SExtractor (10 objects), and objects where the photometric SED did not appear accurate (3 objects), e.g., obvious flux visible in a dropout filter that was not accurately recorded (usually due to crowding). Of the full sample of 91 sources removed, a small number (5) are plausible to still be true high-redshift galaxies. While we conservatively keep them out of our sample, we note them specifically in Table 8 in Appendix B.

Finally, we check this sample for duplicates that could arise, as the 10 NIRCam CEERS pointings have slightly overlapping edges. We find one object that appears in our catalog twice, encouragingly satisfying our sample selection with two independent photometric measures. This object appears in CEERS4 (as ID 42447) and CEERS10 (as ID 93725), with similar $\mathcal{P}(z)$ distributions. As this object has slightly higher S/N in the CEERS4 photometric catalog, we keep ID = 42447 and remove ID = 93725 from our catalog. We note that future work making use of a complete mosaic of all 10 NIRCam pointings will make better use of these near-edge regions by combining the images from both pointings. After removal of the 91 spurious sources and the one duplicate, the sample consisted of 93 candidate galaxies.

3.2.1. Spectroscopic Redshifts

Among the more transformative advances of JWST is NIRSpec's ability to efficiently spectroscopically confirm galaxies via strong [O III] line emission to $z\sim9.5$ and via Lyα spectral breaks to higher redshift. We make use of follow-up spectroscopy from both the CEERS spectroscopic program (which in its second epoch placed NIRSpec slits on some

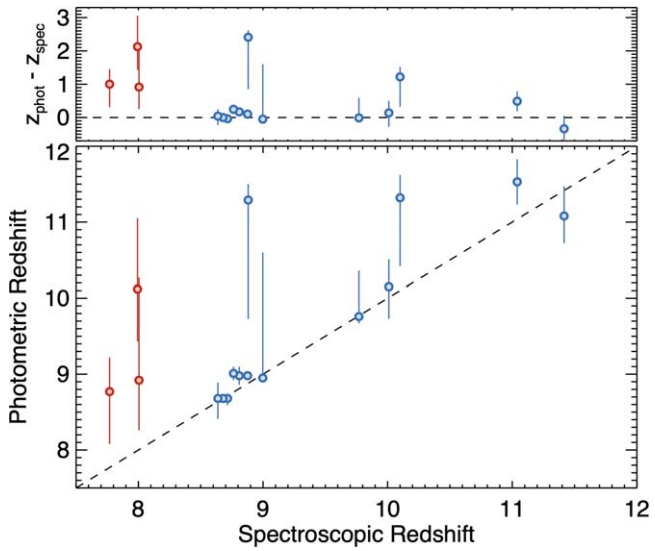

Figure 1. A comparison of the photometric redshifts to the measured spectroscopic redshifts for the 17 galaxies in our initial sample with spectroscopic confirmation. With the exception of the (not shown) $z \sim 16$ candidate at $z_{spec} = 4.9$ (Arrabal Haro et al. 2023b), the agreement is generally good. After removal of three sources (in red) with spectroscopic redshifts below our cut of $z > 8.5$, we find a median (mean) $z_{phot} - z_{spec} = 0.1$ (0.3), with 8/13 sources having $|z_{phot} - z_{spec}| < 0.2$. As noted by Arrabal Haro et al. (2023a) and Fujimoto et al. (2023a), there does appear to be a mild systematic offset toward higher photometric redshifts. We also note that there are four sources with $z_{phot} > 10$ observed with NIRSpec that showed no detectable signatures, which is consistent with $z > 10$, where all strong lines are shifted out of the NIRSpec range.

sources observed in the first epoch) and a Director's Discretionary Time (DDT) program in the CEERS field (PID 2750; PI Arrabal Haro; Arrabal Haro et al. 2023b). Fujimoto et al. (2023a) presented [O III]–based redshifts for sources in the ∼3100 s CEERS second-epoch medium-resolution grating and prism observations, while Arrabal Haro et al. (2023a) presented both Lyα break and [O III]–based redshifts for sources in the ∼3100 s CEERS third-epoch prism observations (additional redshifts were also presented in Larson et al. 2023a and Tang et al. 2023). Arrabal Haro et al. (2023b) presented both Lyα break and line-based ([O II] and [O III]) redshifts for sources in the ∼5 hr prism DDT observations (one of these sources had its redshift of $z = 11.04$ first presented in Harikane et al. 2023a).

Cross-matching our sample of 93 galaxy candidates to these spectroscopic lists, we find 17 sources that have published spectroscopic redshifts. A comparison between the photometric redshifts and spectroscopic redshifts is shown in Figure 1. Not shown in this figure is the single catastrophic redshift failure (defined as $|z_{spec} - z_{phot}|/(1 + z_{spec}) > 0.3$), the galaxy (ID = 13256) originally presented in Donnan et al. (2023a) as having $z \sim 16.5$, with similar redshifts proposed by Harikane et al. (2023a) and F23; a lower redshift of $z_{phot} \sim 4.5$–5 was proposed in Pérez-González et al. (2023a) and Naidu et al. (2022a). As discussed in Arrabal Haro et al. (2023b), this object has a confirmed redshift of $z \sim 4.9$ and is the result of a very pathological situation where at this specific redshift a red galaxy with extreme line emission can mimic a $z \sim 16$ galaxy, as the Hα line falls in all three of the F356W, F410M, and F444W filters, while [O III] enhances F277W (see also discussion in Zavala et al. 2023).

In addition, we remove one object that also has $z_{phot} \sim 16$ (ID = 43382, with a 68% confidence range on the photometric redshift of $z = 15.9$–19.2). While fainter than ID = 13256 (F277W = 28.8 vs. 26.5), its spectral signature is almost identical; thus, we consider it a likely fainter companion to the $z \sim 4.9$ overdensity confirmed in Arrabal Haro et al. (2023b).

We find three additional sources with spectroscopic redshifts below our nominal redshift cut of $z > 8.5$, which we thus remove. These are ID = 4774, ID = 4777, and ID = 23084. ID = 4774 has a photometric redshift 68% confidence limit (CL) of 8.26–10.27, with $z_{spec} = 8.01$. ID = 4777 has a photometric redshift 68% CL of 9.43–11.05, with $z_{spec} = 7.99$. ID = 23084 has a photometric redshift 68% CL of 8.08–9.22, with $z_{spec} = 7.77$. While the spectroscopic redshift is outside the 68% confidence range on the photometric redshift, the redshifts are not catastrophically low. We tabulate the five removed sources, including their celestial coordinates, in Table 9 in Appendix B.

Beyond these five removed sources, we find generally good agreement between the photometric and spectroscopic redshifts, with a median (mean) $z_{phot} - z_{spec} = 0.1$ (0.3), with 8/13 sources having $|z_{phot} - z_{spec}| < 0.2$ (the median offset was 0.2 prior to removal of the five sources in the preceding paragraph). As noted by Arrabal Haro et al. (2023a), there does appear to be a systematic offset toward higher photometric redshifts. One likely explanation for this is that the shape of the Lyα break in these galaxy spectra is more extended than the sharp break assumed in the intergalactic medium (IGM) attenuation models employed by EAZY. This could be due to a variety of factors, including stellar population properties not accounted for by the typically used templates (e.g., Arrabal Haro et al. 2023a), the Lyα damping wing from an increasingly neutral IGM (e.g., Arrabal Haro et al. 2023a; Curtis-Lake et al. 2023; Umeda et al. 2023), and/or extremely dense line-of-sight damped Lyα systems in close proximity to a given galaxy (Heintz et al. 2023; Hsiao et al. 2023). Additionally, some of the spectroscopic redshifts we compare to come from the Lyα break alone, which has additional uncertainties (see discussion in Fujimoto et al. 2023b). It is important to note that several additional sources were spectroscopically observed but not detected (indicated as "Nz" in Tables 3 and 6); this is modest evidence in favor of $z > 9.6$, as at lower redshifts [O III]+Hβ should have been detectable. For the remainder of our analysis, we use the spectroscopic redshift values when they are available, which is the case for 13 of our final sample of 88 candidate galaxies.

3.2.2. Kron Aperture Corrections

During the visual inspection step, we found that some legitimate high-redshift galaxies had Kron apertures that appeared much larger than the galaxy in question, stretched by nearby galaxies. Similar to F23, we devise a correction to ensure that flux from neighboring galaxies does not bias the colors or the total fluxes. To identify sources where this is needed, we explore the ratio between the area of the Kron aperture and the area of a $d = 0.''2$ circular aperture. Our galaxy sample shows a lognormal distribution, with a peak aperture ratio of ∼2, with a tail to higher values. There is a notable gap at a ratio of ∼10; thus, we flag sources with aperture size ratios larger than this as potentially needing a correction.

We find that just one source meets this criterion, ID = 11384 (with an aperture ratio of 14.7; the next highest was 9.3). Upon

Table 3
Summary of $z > 9.7$ Candidate Galaxies

ID	R.A. (J2000)	Decl. (J2000)	$m_{\rm F277W}$ (mag)	M_{1500} (mag)	$\mathcal{C}_{\rm FUV}$ (mag)	$\int_7^{20}\mathcal{P}(z)$	$\Delta\chi^2$	Photometric Redshift	Spectroscopic Redshift
CEERS-90891	214.945818	52.829729	28.3	$-19.8^{+0.3}_{-0.1}$	$-0.12^{+0.16}_{-0.03}$	0.96	4.8	$14.44^{+0.48}_{-1.89}$	⋯
CEERS-64602	215.074304	52.951154	28.8	$-19.3^{+0.3}_{-0.2}$	$0.00^{+0.11}_{-0.15}$	0.99	8.2	$14.32^{+0.75}_{-1.41}$	⋯
CEERS-57438	214.871989	52.845014	28.3	$-19.6^{+0.3}_{-0.2}$	$0.03^{+0.23}_{-0.07}$	0.96	4.2	$13.99^{+0.75}_{-1.35}$	⋯
CEERS-77647	215.054220	52.923839	29.0	$-18.9^{+0.3}_{-0.0}$	$-0.19^{+0.11}_{-0.01}$	1.00	9.4	$12.70^{+-0.09}_{-0.66}$	⋯
CEERS-2067	215.010026	53.013641	27.8	$-20.1^{+0.2}_{-0.0}$	$0.02^{+0.09}_{-0.03}$	1.00	8.3	$12.70^{+-0.09}_{-0.72}$	Nz
CEERS- 36796	214.727248	52.748045	28.2	$-19.9^{+0.2}_{-0.2}$	$-0.11^{+0.11}_{-0.06}$	0.98	6.5	$12.28^{+1.59}_{-0.24}$	⋯
CEERS-70831	215.100921	52.936270	28.1	$-19.6^{+0.3}_{-0.3}$	$0.06^{+0.22}_{-0.08}$	0.93	4.7	$12.07^{+1.98}_{-1.08}$	⋯
CEERS-34925	214.738486	52.765665	28.4	$-19.0^{+0.4}_{-0.4}$	$0.33^{+0.36}_{-0.19}$	1.00	10.5	$11.89^{+1.92}_{-1.68}$	⋯
CEERS-34685	214.700083	52.752419	28.4	$-19.4^{+0.3}_{-0.2}$	$-0.06^{+0.21}_{-0.03}$	0.96	6.1	$11.53^{+0.51}_{-0.72}$	⋯
CEERS-16943	214.943152	52.942442	27.9	$-20.2^{+0.1}_{-0.1}$	$-0.12^{+0.03}_{-0.02}$	1.00	30.2	$11.08^{+0.39}_{-0.36}$	$11.416^{+0.005}_{-0.005}$
CEERS-26112	214.818999	52.865299	28.3	$-19.9^{+0.3}_{-0.1}$	$-0.09^{+0.20}_{-0.01}$	0.93	5.0	$11.38^{+0.30}_{-0.81}$	⋯
CEERS-54306	214.858815	52.850712	28.8	$-19.3^{+0.1}_{-0.1}$	$-0.19^{+0.00}_{-0.00}$	1.00	11.3	$11.23^{+0.36}_{-0.36}$	⋯
CEERS-76686	214.976311	52.873417	28.2	$-19.2^{+0.1}_{-0.2}$	$0.03^{+0.07}_{-0.11}$	1.00	13.6	$11.11^{+0.33}_{-0.36}$	⋯
CEERS-87379	214.932064	52.841873	27.3	$-20.7^{+0.2}_{-0.1}$	$-0.19^{+0.14}_{-0.00}$	1.00	23.7	$11.08^{+0.24}_{-0.48}$	Nz
CEERS-85546	214.885963	52.819060	27.7	$-20.3^{+0.2}_{-0.1}$	$-0.15^{+0.11}_{-0.00}$	1.00	26.3	$11.08^{+0.24}_{-0.60}$	⋯
CEERS-11384	214.906640	52.945504	27.5	$-20.0^{+0.1}_{-0.1}$	$0.20^{+0.09}_{-0.09}$	1.00	11.2	$11.53^{+0.30}_{-0.30}$	$11.043^{+0.003}_{-0.003}$
CEERS-77367	214.989018	52.879278	27.9	$-20.0^{+0.2}_{-0.2}$	$-0.07^{+0.08}_{-0.08}$	0.97	6.7	$10.84^{+0.54}_{-0.51}$	⋯
CEERS-47141	214.910771	52.873928	28.7	$-18.6^{+0.4}_{-0.2}$	$0.12^{+0.36}_{-0.02}$	0.97	6.1	$10.66^{+1.50}_{-0.48}$	⋯
CEERS-16984	214.866488	52.887854	28.5	$-19.2^{+0.1}_{-0.2}$	$-0.10^{+0.11}_{-0.02}$	0.97	7.0	$10.63^{+0.39}_{-0.24}$	⋯
CEERS-54903	214.811119	52.813829	29.0	$-18.3^{+0.2}_{-0.3}$	$0.05^{+0.23}_{-0.08}$	0.93	5.7	$10.60^{+0.81}_{-0.36}$	⋯
CEERS-57400	214.869658	52.843646	28.7	$-19.4^{+0.2}_{-0.2}$	$-0.00^{+0.07}_{-0.15}$	1.00	12.4	$10.60^{+0.60}_{-0.66}$	Nz
CEERS-10332	215.044001	52.994302	28.4	$-19.5^{+0.4}_{-0.1}$	$-0.06^{+0.20}_{-0.01}$	1.00	14.3	$10.57^{+0.18}_{-1.05}$	Nz
CEERS-92463	214.975831	52.841961	28.3	$-18.8^{+0.4}_{-0.1}$	$0.17^{+0.23}_{-0.02}$	1.00	21.1	$10.51^{+0.69}_{-0.60}$	⋯
CEERS-74300	214.969256	52.882119	28.2	$-19.3^{+0.1}_{-0.2}$	$-0.14^{+0.06}_{-0.05}$	1.00	12.3	$10.51^{+0.30}_{-0.57}$	⋯
CEERS-101746	214.881212	52.772963	28.4	$-19.6^{+0.2}_{-0.1}$	$-0.19^{+0.07}_{-0.00}$	1.00	20.4	$10.33^{+0.24}_{-0.72}$	⋯
CEERS-19996	214.922787	52.911529	28.3	$-19.3^{+0.2}_{-0.1}$	$0.18^{+0.04}_{-0.17}$	1.00	11.7	$11.32^{+0.30}_{-0.90}$	$10.10^{+0.13}_{-0.26}$
CEERS-98518	214.817113	52.748343	27.4	$-19.9^{+0.2}_{-0.1}$	$0.21^{+0.08}_{-0.05}$	1.00	17.4	$10.09^{+0.18}_{-0.39}$	⋯
CEERS-35590	214.732525	52.758090	27.7	$-20.2^{+0.1}_{-0.0}$	$-0.07^{+0.06}_{-0.05}$	1.00	34.9	$10.15^{+0.36}_{-0.42}$	$10.01^{+0.14}_{-0.19}$
CEERS-99715	214.811852	52.737110	27.1	$-20.5^{+0.1}_{-0.0}$	$0.06^{+0.06}_{-0.05}$	1.00	37.7	$9.76^{+0.60}_{-0.09}$	$9.77^{+0.37}_{-0.29}$
CEERS-61941	214.850131	52.808053	28.9	$-18.6^{+0.1}_{-0.3}$	$0.08^{+0.07}_{-0.15}$	1.00	12.8	$9.76^{+1.02}_{-0.18}$	⋯

Note. A summary of the key properties for the 30 galaxies in our sample at $z > 9.7$ (the remaining 55 galaxies with $8.5 \leqslant z < 9.7$ are presented in the Appendix A). $\mathcal{C}_{\rm FUV}$ is defined in Section 3.4 as the rest-frame far-UV color. The photometric redshift is "za" from EAZY, which is the redshift where the χ^2 is minimized. The $\int_7^{20}\mathcal{P}(z)$ quantity is the integrated redshift probability density between $z = 7$ and 20, which was used in the sample selection. The $\Delta\chi^2$ compares the best-fitting low-redshift ($0 < z < 7$) model to the best-fitting high-redshift model; a value of $\geqslant$4 was required for selection. Spectroscopic redshifts come from Arrabal Haro et al. (2023b) and Arrabal Haro et al. (2023a); we list "Nz" when an object was spectroscopically observed but no robust redshift was determined. As discussed in the text, this is modest evidence in favor of $z > 9.6$, as at lower redshifts [O III]+$H\beta$ should have been detectable.

(This table is available in machine-readable form.)

inspection of this source, it is very compact but is in a region of high background with a very bright galaxy $\sim$1.″5 to the northwest and a modestly bright galaxy $\sim$0.″5 to the south, resulting in an elongated Kron aperture in the north–south direction. For this object we thus make use of colors measured in $d = 0.''2$ circular apertures. To calculate total fluxes, we derive an aperture correction as the median of the ratio of the total F277W flux to the flux measured in a $d = 0.''2$ circular aperture for all sources in our full photometry catalog with $d = 0.''2$ fluxes within 20% of the F277W $= 0.''2$ flux for this object. We find that this correction factor is 2.9 for ID = 11384, consistent with the values for other sources in our galaxy sample (median of 2.3 ± 0.8).

For this object we then replace its default fluxes with these new values and adopt the photometric redshift results from colors measured in the small circular apertures. This increases the photometric redshift from 10.8–11.4 to 11.2–11.8. Of note is that this source has a spectroscopic redshift of 11.043 (Arrabal Haro et al. 2023b; Harikane et al. 2023a). While the uncorrected photometric redshift is more consistent, the higher value from our improved photometry matches the observed very shallow Lyα break observed in the prism spectrum of this source (the redshift inferred from this break in the prism spectrum is $z \approx 11.4$; Arrabal Haro et al. 2023b), which can lead to minor photometric redshift overestimates as discussed in the previous subsection.

3.2.3. Lyα Break

As a cross-check on our Lyα break criterion, we examine our sample for objects where there is a discrepancy between the primary photometric redshift peak and the S/N in bands nominally below the break; such sources can still satisfy our criterion for inclusion in a high-redshift bin if their $\mathcal{P}(z)$ is bimodal or somewhat broad.

We identify two sources in our nominal $z \sim 11$ sample (see Section 3.4 for sample definitions) that have $\mathcal{P}(z)$ values that exhibit two high-redshift peaks: a larger peak at $z > 9.5$, and a significant secondary peak at $z \sim 9$. These objects are ID = 17898 and 42447 (neither has spectroscopic redshifts). Both objects exhibit S/N > 2 in F115W. As the lower 16th percentile of their $\mathcal{P}(z)$ was at $z < 9.54$ (the redshift of Lyα at the red edge of the F115W filter FWHM), this significant F115W flux did not violate our selection criteria. However, as this flux is measured as significant (S/N = 3.1 and 5.7 for these two objects, respectively), the $z \sim 9$ peak is more likely to be correct. For these two objects, we thus applied a prior to their $\mathcal{P}(z)$, setting them to zero at $z > 9.54$, renormalizing to unity and recomputing the best-fit photometric redshift as the new peak. We find that the peak photometric redshift for these sources changes from $z = 10.45$ to $z = 9.07$ for ID = 17898 and from $z = 10.30$ to $z = 9.13$ for ID = 42447. We confirm that both sources continue to satisfy our selection criterion of $\mathcal{P}(z > 7) > 0.7$.

We also do a similar analysis for sources in our $z > 13$ sample. We find two sources with S/N in F150W > 2. These objects (ID = 2067 with S/N = 2.57, and ID = 77647 with S/N = 2.45) both exhibit a broad $\mathcal{P}(z)$, extending down to $z \sim 11$; thus, this F150W flux did not violate our selection criteria. We apply a similar prior, setting $\mathcal{P}(z > 12.72;$ corresponding to the red edge of F150W) to zero. We find that the peak photometric redshift for these three sources changes from $z = 13.69$ to 12.70 and from $z = 13.57$ to 12.70 (e.g., the new peak is at the edge of the prior).

We acknowledge that while EAZY had knowledge of these observed S/Ns and still found a preferred peak at higher redshift, the obvious real flux in the images left us confident that applying this prior to the $\mathcal{P}(z)$ will result in more accurate redshift estimates. These $\mathcal{P}(z)$ priors were applied in the completeness simulations discussed in Section 4.1. When photometric redshift PDFs are shown in Section 3.4, we show the original $\mathcal{P}(z)$ as a faded black curve for these sources.

3.3. Stellar Contamination

The colors of high-redshift galaxies, especially between 1 and 2 μm, can be degenerate with low-mass stars and substellar objects (e.g., Wilkins et al. 2014; Finkelstein 2016). While the photometric coverage from 1 to 5μm should mitigate this confusion, here we explore whether the colors of our candidate galaxies could plausibly be consistent with low-mass stars or brown dwarfs. We fit each candidate to a grid of low-temperature, cloudy, chemical equilibrium substellar atmosphere models from Sonora-Diamondback (Morley et al. 2024). We explore a range of temperatures $T \sim 900$–2400 K, surface gravities $g = 100$ and 3160, and metallicities [M/H] = 0 and −0.5. We convolve the model SEDs with the HST+JWST filter curves and perform a simple grid-fitting routine, scaling the fluxes of each model to minimize the χ^2. We adopt the model with the lowest χ^2 as the best-fitting stellar model. We estimate the implied distance by scaling the model fluxes and assuming an intrinsic radius of 1 Jupiter radius. We note that we also ran fits with cloud-free model grids extending to particularly cold (Sonora-Bobcat, $T \sim 200$–1300 K; Marley et al. 2021) and low-metallicity (LOWZ, [M/H] = −1; Meisner et al. 2021) parameter spaces; however, none provided a better fit over the Sonora-Diamondback models.

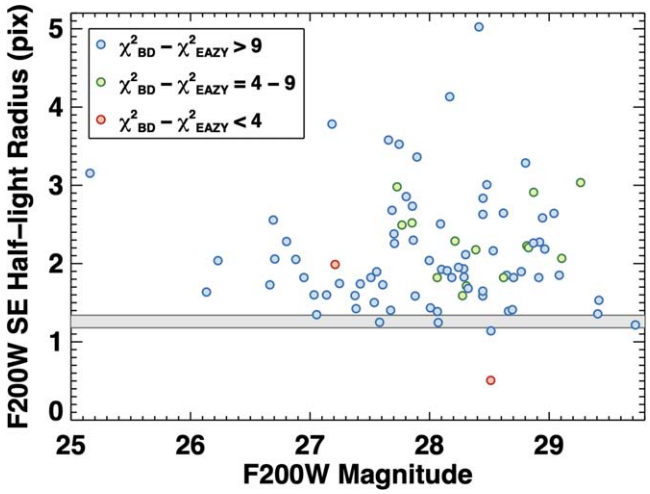

Figure 2. The F200W half-light radius (measured from SExtractor) vs. F200W apparent magnitude. The gray bar shows the half-light radius from stars in the image (with the width showing the 68% spread in the values). The data points are color-coded by the difference in χ^2 between the best-fitting (sub)stellar model and the best-fitting EAZY galaxy model. Most objects are clearly resolved and thus extragalactic in origin. Only one object is formally compact with a stellar χ^2 comparable to the best-fitting EAZY model, though even for this object we conclude that it is likely extragalactic owing to its noncompact appearance in the imaging and the very large (∼4 kpc) implied distance were it stellar. We conclude that stellar contamination is not significant in our sample.

In Figure 2 we show the results of this analysis. Here we plot the SExtractor-measured F200W half-light radius for our 88 candidate galaxies versus their apparent F200W magnitude, compared to the half-light radius of the F200W PSF as measured from stars in the image. One can see that the majority of our galaxy sample is clearly resolved and thus nonstellar in origin. To diagnose the potential stellar nature of the more compact objects, the data points are color-coded by the difference in the goodness of fit (χ^2) between the best-fitting (sub)stellar model and the best-fitting EAZY model. We find that no objects are better fit by the stellar model (e.g., the EAZY χ^2 is always lower). We do find two sources where the difference between the stellar and EAZY χ^2 is <4. One is significantly resolved, but the other object (ID = 34925) is measured by SExtractor as being very compact (in fact, unphysically smaller than the PSF). However, we conclude that this object is much more likely a galaxy. First, examining the imaging of this object, it does not appear to be obviously pointlike; rather, it is faint, barely above our significance thresholds, and thus the SExtractor half-light radius is quite uncertain. Second, due to its faint brightness, its implied distance (were it stellar in origin) would be ∼4 kpc, which would be extremely far into the halo, and thus highly unlikely. We conclude that we find no evidence for stellar contamination in the sources in our sample.

3.4. Sample Summary

After removing visually identified spurious sources, the four sources with $z_{spec} < 8.5$, and the faint $z \sim 16$ candidate that is likely at $z \sim 4.9$, our sample contained 88 candidate $z > 8.5$ galaxies. For our analysis we divide these candidate galaxies into three subsamples: $z \sim 9$, which contains the 58 galaxies with $8.5 \leqslant z_{best} \leqslant 9.7$; $z \sim 11$, which contains the 27 galaxies

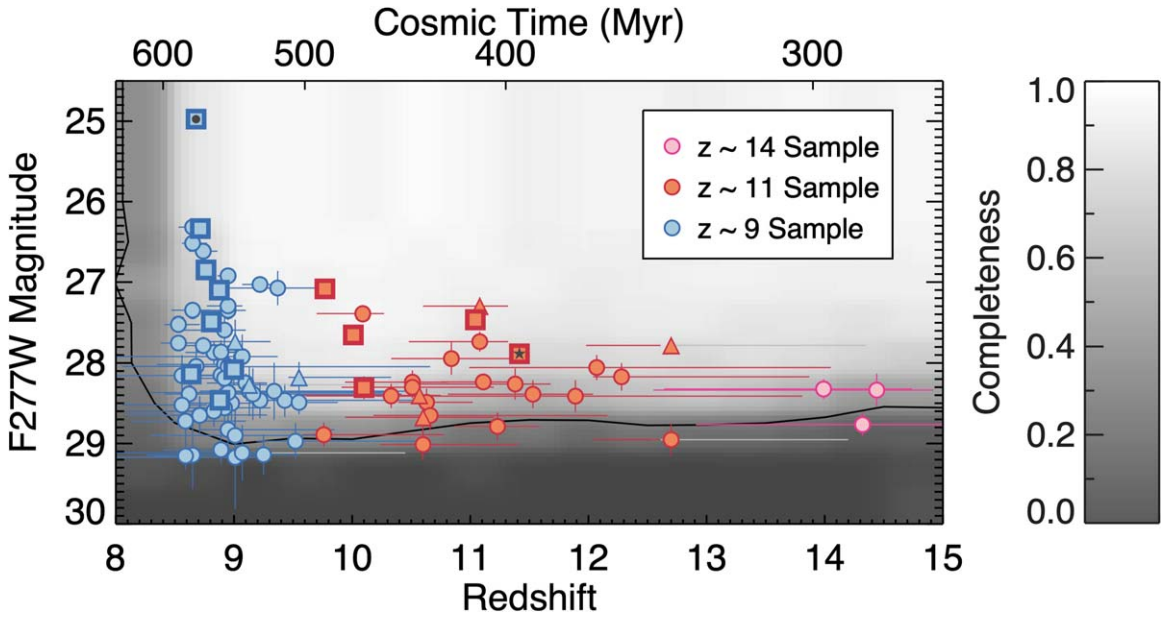

Figure 3. The symbols show our sample of 88 $z > 8.5$ galaxy candidates in a plane of F277W magnitude versus redshift, with the different colors representing the different redshift samples. Squares denote objects with spectroscopic confirmation, while the circles are plotted at the photometric redshifts. Triangles denote objects with spectroscopic observations but no confirmation. The small star denotes Maisie's Galaxy (Finkelstein et al. 2022b), one of the first JWST very high redshift galaxy discoveries, while the small circle denotes CEERS-1019, a confirmed $z = 8.7$ galaxy that appears to have broad Hβ emission, indicative of an active supermassive black hole (Larson et al. 2023a). The background shading shows the completeness (inclusive of both photometric and sample selection completeness) of our sample (for sources with half-light radii of 3.3 pixels), as described in Section 4.1; the black line shows the 20% completeness contour.

with $9.7 < z_{\rm best} \leqslant 13$; and $z \sim 14$, which contains the three galaxies with $z_{\rm best} > 13$.

For all objects in our sample we calculate an observed rest-UV absolute magnitude following Finkelstein et al. (2015). Briefly, we perform a simple round of SED fitting with BC03 (Bruzual & Charlot 2003) models to derive a best-fitting model spectrum. We then calculate the bandpass-averaged flux from this spectrum in a top-hat filter curve spanning 1450–1550 Å in the rest frame, converting to an apparent magnitude and then applying the cosmological distance modulus for a given redshift. As a part of this process, we run Monte Carlo simulations sampling the photometric redshift $\mathcal{P}(z)$, such that the resulting uncertainty on M_{1500} is inclusive of both the photometric scatter and redshift uncertainty. We note that in this process we set $\mathcal{P}(z < 6) = 0$, such that any low-redshift solutions (which are small by design) do not bias the magnitude calculation. During this process, we also calculated a rest-far-UV color (discussed in Section 5), dubbed $\mathcal{C}_{\rm FUV}$, calculated as

$$\mathcal{C}_{\rm FUV} = -2.5 \log_{10}\left(\frac{f_{1470}}{f_{1850}}\right), \quad (2)$$

where f_{1470} and f_{1850} are the bandpass-averaged fluxes in f_ν units in top-hat filters spanning 1430–1510 and 1800-1900, respectively (where these windows were designed to probe the color in the far-UV avoiding strong spectral features).

We show the distribution of our sample in F277W magnitude and photometric redshift in Figure 3. Figures 4, 5, and 6 contain summary figures of sources in the $z \sim 14$, 11, and 9 samples, respectively. The last two are figure sets, with two example objects shown, and with all objects viewable in the electronic version of the manuscript. We tabulate key properties of our sample in Table 3 for $z > 9.7$ and in Table 6 in Appendix A for $z < 9.7$.

3.4.1. Comparison to McLeod et al. (2024) and Adams et al. (2024)

We compare our sample to that of McLeod et al. (2024) and Adams et al. (2024), who have also selected $z \gtrsim 8.5$ galaxies from the full CEERS data set. McLeod et al. (2024) restrict their sample to galaxies with detection S/N greater than 8; thus, their sample is smaller than ours, at 23 galaxies. We find that 14 of these 23 galaxies are in our final sample. We explored the properties of the remaining nine galaxies in our catalog. We find that two of the nine objects have dominant $z > 9$ solutions but fail our $\Delta\chi^2$ criterion. The remaining seven objects all have plausible high-redshift solutions (based on little to no detectable flux in F115W) but have dominant low-redshift solutions.

While Adams et al. (2024) did not provide a catalog in their paper, we obtained the revised version of their sample via private communication. Their final sample of $z > 8.5$ galaxies consists of 55 objects, of which 25 are in our final $z > 8.5$ galaxy sample. All 30 not contained in our sample are present in our parent photometric catalog, all with a plausible redshift solution at $z > 7$ (16/30 have >50% of their integrated $\mathcal{P}(z)$ at $z > 7$ in our catalog). Two of these sources nominally pass all our selection cuts, except their best-fitting photometric redshifts are $z \sim 7.5$–8.2. Of the remaining 28, 26 do not pass our $\Delta\chi^2$ cut, including 18 that do not pass our integrated $\mathcal{P}(z)$ cut. This is likely driven in some cases by weakly positive ($\geqslant 1\sigma$ significance) flux present in F606W and/or F814W in 14/28 objects, down-weighting high-redshift solutions.

3.4.2. Differences from Finkelstein et al. (2023)

In F23 we presented 26 $z > 8.5$ candidates from the first epoch of CEERS, using 4 of the 10 CEERS NIRCam fields used here. As our photometry and sample selection procedures here are slightly updated, we cross-checked our sample with the F23 sample. We find that 20/26 galaxies presented in F23

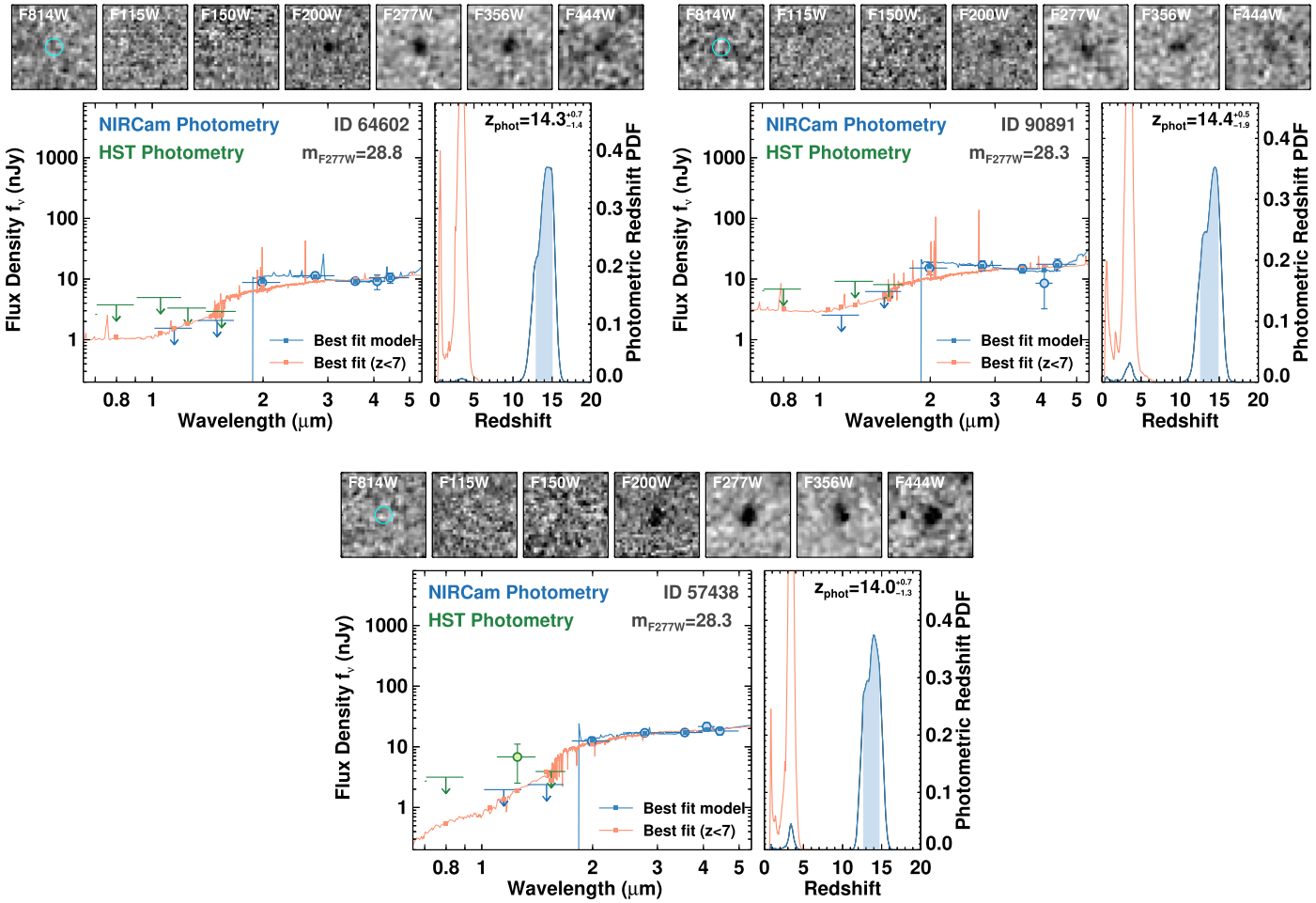

Figure 4. Summary figures of the three objects in our sample with $z_{best} > 13$. The top row shows 1″ cutout images in the F814W, F115W, F150W, F200W, F277W, F356W, and F444W filters (the F410M and remaining HST bands are not shown for brevity). The cyan circle in the first panel shows a 0.″2-diameter circle (the size used to measure detection significance). The bottom left panel shows the SED, with blue (green) points representing photometry from NIRCam (HST). Upper limits shown are 1σ. The bottom right panel shows the photometric redshift distribution in blue (with the corresponding best-fit model in blue in the bottom left panel). The light-red curves show the photometric redshift results when constrained to $z < 7$.

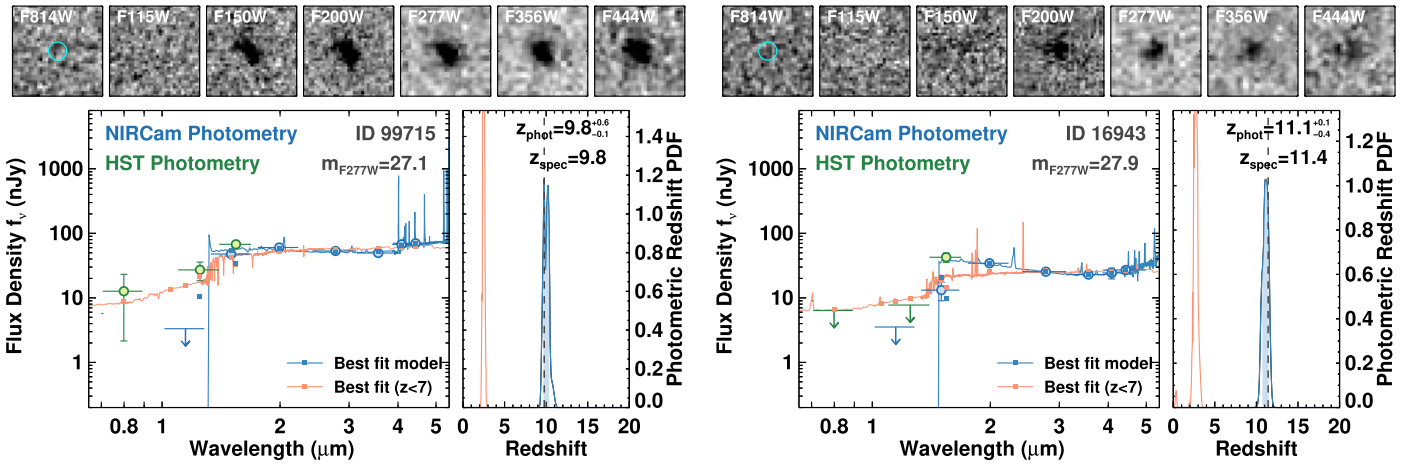

Figure 5. Same as Figure 4, but for two example sources in the $z \sim 11$ galaxy candidate sample. The object on the left has a confirmed spectroscopic measurement via detection of the Lyα break from Arrabal Haro et al. (2023a), while the object on the right is the spectroscopically confirmed Maisie's Galaxy (Finkelstein et al. 2022b; Arrabal Haro et al. 2023b). The complete figure set (27 images) is available in the online journal.

(The complete figure set (27 images) is available.)

are included in our sample here. Of the six galaxies not included here, four of them originally satisfied our sample selection but were removed because they are now known to have spectroscopic redshifts $z_{spec} < 8.5$ (see Section 3.2.1). These are ID = 4774 (F23 ID 3908), 4777 (F23 ID 3910), 13256 (F23 ID 2159), and 23084 (F23 ID 1748). The

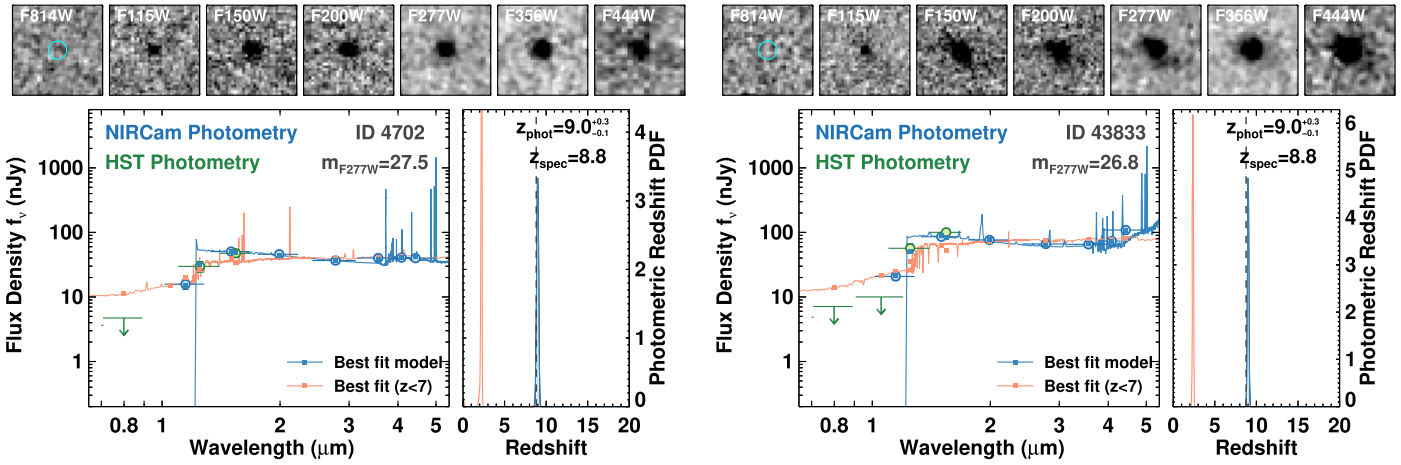

Figure 6. Same as Figure 4, but for two example sources in the $z \sim 9$ galaxy candidate sample. Both example sources have confirmed spectroscopic measurements via [O III] line emission from Fujimoto et al. (2023a). Of note is that both sources were beyond the detection limit of the CANDELS imaging in this field, yet they appear very bright and extended in these ∼2900 s JWST/NIRCam data. The complete figure set (58 images) is available in the online journal.

(The complete figure set (58 images) is available.)

remaining two sources satisfied all sample selection criteria except the S/N below the Lyα break. ID 2241 (F23 ID 1875) has a 1.9σ detection in F606W and 1.98σ detection in F814W, failing that criterion. ID 8497 (F23 ID 7227) has a 2.6σ detection in F115W, which fails this criterion for this object's $\mathcal{P}(z)$ distribution, which peaks at $z = 11.2$.

In our present work, over these four fields we identify 35 $z > 8.5$ candidates, which includes 20 galaxies from F23 and 15 new sources. We explored these new sources to see why they were not included in the F23 sample. All 15 sources are present in the F23 photometric catalog. Of these 15, 11 sources have best-fit photometric redshifts in the F23 catalog of $z > 8.5$. Comparing the photometric redshifts of these 11 sources in this previous catalog to our own, we find a median photometric redshift difference of zero (with a mean difference of 0.11, with the new values being slightly smaller). The majority of these sources (8/11) were previously excluded, as they failed the $\Delta\chi^2$ criterion (with values of ∼1–3). The other three fell just on the other side of the F23 best-fit photo-z, detection threshold, or Lyα break nondetection thresholds. Of the four objects fit at lower redshift, three have significant high-redshift peaks, with $\int \mathcal{P}(z) > 7$ of 0.73 (ID 10545), 0.43 (ID 17898), and 0.66 (ID 61620); the remaining source, ID 20174, has a lower significance peak at $z \sim 9$.

While this comparison makes it apparent that modest changes to photometry procedures can have not insignificant effects on the composition of a high-redshift galaxy sample, the changes we implemented to our procedure here over that from F23 were done to increase photometric accuracy, primarily for the colors of faint galaxies. The fact that all new sources that we select had significant high-redshift solutions in the F23 catalog adds confidence to our sample, though we fully acknowledge that spectroscopic confirmation of a *majority* of this sample is needed for full confidence. Fortunately, with the power of JWST, this is possible.

4. Results

Here we explore constraints on the abundance of galaxies at $z > 8.5$ that we can place with our sample selected from the full CEERS. In Section 4.2 we describe measurements of the cumulative surface density, while in Section 4.3 we describe the rest-frame UV luminosity function. Both measurements require a correction for incompleteness, which we describe in Section 4.1.

4.1. Completeness Simulations

We quantify the completeness of our sample selection, broadly following F23, with an update here to implement an important size dependence. Our completeness estimates come from complete end-to-end source injection simulations, injecting mock galaxies with a range of properties into our images and then performing photometry, photometric redshift measurements, and sample selection procedures in a manner identical to the process performed on the real data. In this way, we account for incompleteness due to both photometric effects, as well as sample selection effects.

For each of the 10 CEERS NIRCam pointings we run 50 simulation iterations. Within each iteration we simulate 1000 sources over a uniform range of redshift from $8 < z < 17$. The majority of the iterations had a lognormal distribution in F277W apparent magnitude peaking at $m \sim 29$; we supplement these with additional simulations with a flat magnitude distribution to boost the number of brighter galaxies. The result is a roughly flat distribution from $m_{F277W} = 22$ to 26, with a larger, lognormal-shaped distribution from $m_{F277W} = 26$ to 30.

To simulate the fluxes in all observed HST and JWST/NIRCam filters, we use BC03 (Bruzual & Charlot 2003) stellar population models with a distribution of stellar population age, dust attenuation, and metallicity tuned to reproduce the expected (and now observed; e.g., Cullen et al. 2023; Morales et al. 2024) blue colors of very high redshift galaxies (see Finkelstein et al. 2015 for details on these models). The result is a lognormal distribution of rest-UV colors, which peaks at F200W–F277W = −0.05, with a 68% spread from F200W–F277W = −0.25 to +0.3, comparable to the measured colors of our observed objects (median of −0.1, 68% spread from −0.3 to 0.3). The resulting model spectrum was then normalized to the F277W magnitude for a given object, with

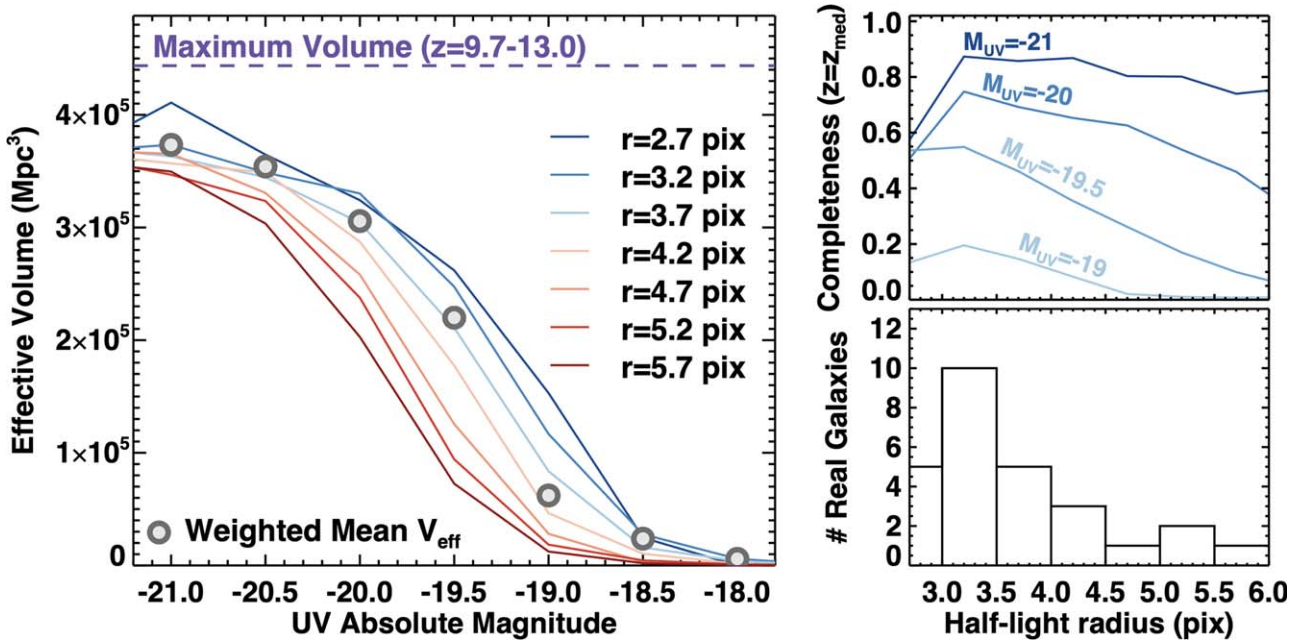

Figure 7. The left panel shows the effective volume for our $z \sim 11$ ($9.7 < z \leqslant 13$) galaxy sample. The purple dashed line shows the maximum volume one would obtain with a 100% completeness over an ideal (though unrealistic) top-hat selection function. The colored curves show our calculated effective volumes as a function of source half-light radii. The circles show the volumes we use, calculated by weighting the volumes by the sizes of galaxies in a given magnitude bin. The size distribution of our $z \sim 11$ galaxy sample is given in the bottom right panel, while the completeness as a function of size at fixed input UV absolute magnitude is shown in the top right panel. The completeness is very sensitive to the size, particularly at fainter magnitudes.

magnitudes in the remaining filters derived by integrating this spectrum through a given bandpass.

Source morphologies were created using GALFIT (Peng et al. 2002) assuming a Sérsic profile with a lognormal distribution in the Sérsic index n (peaking at 1.2, with a minimum of $n = 1$ and a tail to $n = 5$), a lognormal distribution of the axis ratio with a peak at 0.8, and a uniform distribution of the position angle. While in F23 we tuned the half-light radius (r_h) distribution such that the recovered r_h distribution matched that observed in our sample, here we update our procedure to implicitly include the size of galaxies in our sample in the completeness calculation. We thus use a uniform input distribution of r_h from 1 to 8 pixels (0.″03–0.″24). Finally, the empirical PSF described in Section 2 is provided to GALFIT for a given band.

These simulated galaxy images are then created with GALFIT as 101×101 pixel images, which we add at random positions to the real images (avoiding only image edges and regions of extremely high ERR-map values [>1000]). Notably, we do not avoid the positions of real objects, such that our simulations account for incompleteness due to sources along similar lines of sight to high-redshift galaxies. We also create a full-frame image just of the simulated sources in F277W, on which we run SExtractor to measure a "noiseless" version of the recovered SExtractor r_h in this filter for use with the completeness calculations (as we discuss below, the measured SExtractor r_h is biased low from the GALFIT input value, even in the noiseless image).

The result of this process is a version of our data in all filters with these 1000 simulated sources included, as well as a catalog of their input properties (inclusive of the SExtractor r_h measurement of the input image). At this point, we run an identical process on these images to the one we ran on our real data in Sections 2 and 2.1, including creating the array of PSF-matched images, calculating photometry, aperture corrections, and PSF corrections. Photometric catalogs are created, EAZY is run, and M_{1500} is calculated.

The recovered catalogs are then matched against the input catalogs, resulting in a combined catalog of all recovered sources with their input and recovered properties. As the imaging depths in the 10 CEERS fields are broadly similar (Table 1), we combine these catalogs from all 10 fields into one. This final input catalog consists of 500,000 simulated sources, of which 343,196 sources are recovered by SExtractor (the ∼70% recovery fraction is expected given the larger number of very faint sources that were simulated).

While in F23 we calculated completeness only as a function of magnitude (with an assumed size distribution), here we explicitly add a size dependence, as many of the observed high-redshift galaxies are clearly resolved. For a given bin in absolute magnitude, we calculate the completeness in bins of F277W half-light radius (with a bin width of 0.5 pixels, starting with a bin centered at 1.2 pixels). For this process, we assume the intrinsic size as the half-light radius measured by SExtractor on the noiseless images, as described above. We show how the completeness depends on both UV absolute magnitude and half-light radius in Figure 7. While there is minimal dependence on size at the brightest magnitudes, as one goes fainter, the completeness decreases more steeply for larger sources, as expected.

As we might expect the recovered sizes from both the simulated and real data to be biased, we compare these intrinsic sizes to those measured from the recovered sources. We find that the intrinsic sizes are ∼50% larger. To account for this bias when we calculate the completeness, we multiply the recovered SExtractor sizes of our real sources by this scale factor of 1.53 (this quantity has a small scatter of $\sigma = 0.06$ and is independent of magnitude for $m < 29$). We then set a minimum size for real sources of $r_h = 2.7$ pixels, comparable to that expected for an unresolved source. We also set a maximum size of $r_h = 6.0$

Table 4
CEERS Rest-UV Luminosity Functions

M_{UV} (mag)	Number[a]	Number Density (10^{-5} mag^{-1} Mpc^{-3})	Effective Volume (Mpc^3)
		$z \sim 9$	
−22.5	0	<0.9	187000
−22.0	1	$1.1^{+0.7}_{-0.6}$	187000
−21.5	0	<0.9	187000
−21.0	2	$2.2^{+1.3}_{-1.0}$	193000
−20.5	7	$8.2^{+4.0}_{-3.2}$	177000
−20.0	7	$9.6^{+4.6}_{-3.6}$	161000
−19.5	17	$28.6^{+11.5}_{-9.1}$	120000
−19.0	10	$26.8^{+12.4}_{-10.0}$	77900
−18.5[b]	13	$136.0^{+61.0}_{-49.9}$	18600
		$z \sim 11$	
−21.0	0	<0.5	373000
−20.5	3	$1.8^{+1.2}_{-0.9}$	354000
−20.0	8	$5.4^{+2.7}_{-2.1}$	306000
−19.5	8	$7.6^{+3.9}_{-3.0}$	220000
−19.0[b]	5	$17.6^{+10.3}_{-7.9}$	62100
−18.5[b]	3	$26.3^{+18.2}_{-13.3}$	23800
		$z \sim 14$	
−20.5	0	<1.8	147000
−20.0	1	$2.6^{+3.3}_{-1.8}$	85400
−19.5	2	$7.3^{+6.9}_{-4.4}$	60600

Notes.
[a] This column represents the nominal number of galaxies in a magnitude bin, though in the calculation of the luminosity function we account for galaxies moving between bins due to photometric and photometric redshift uncertainties.
[b] The completeness in these bins is <20%; thus, these data points are not used to constrain the luminosity function evolution.

pixels; one object has a larger (bias-corrected) SExtractor-measured size, yet it is clear from the images that these sizes are incorrectly measured owing to the presence of a neighboring source. For this object, we assume the median size from the sample.

For our surface density analysis described in Section 4.2, we calculate a completeness per source, based on the fraction of recovered sources at the observed F277W magnitude, photometric redshift, and galaxy size. For our rest-frame UV luminosity function analysis described in Section 4.3, we calculate the completeness in bins of absolute UV magnitude. In each magnitude bin we calculate a completeness by weighting the recovery fractions in each size bin by the observed number of sources at each size. We then integrate the comoving volume element across our redshift range with these completeness values, resulting in an effective volume for our sample in a given magnitude bin (a process similar to that done in Finkelstein et al. 2015). These "weighted mean" effective volumes are shown as circles in Figure 7. They broadly trace the completeness curves for sources with $r_h \sim 3.5$ pixels, comparable to the median size of objects in our sample. One can see that assuming point sources in these simulations would lead to effective volume estimates modestly larger across $M_{UV} \sim -20$ to -19. Our final effective volumes are listed in Table 4.

4.2. The Cumulative Surface Density of Galaxies at z > 8.5

Here we explore the evolution of galaxies at $z > 8.5$ via the cumulative surface density, updating the results from the first epoch of CEERS from F23. Figure 8 shows the surface density of objects with redshifts greater than z for sources with $m_{F277W} < 28.5$. Following F23, we correct for incompleteness by counting each galaxy as one divided by the estimated completeness at the redshift and magnitude of a given galaxy, including here the size of the source (as well as the size bias correction discussed in Section 4.1). To avoid significant uncertainty introduced by objects with very low completeness values, we further restrict this analysis to objects with completeness measurements greater than 20% (this includes 58 objects of the 66 with F277W < 28.5; this exclusion was not done in F23). We note that our magnitude limit is chosen as a compromise between maximizing the sample size while minimizing the completeness correction. While 25% of our sample is fainter than this limit, the majority of these fainter sources have completeness <20%. On the other hand, increasing the limit to F277W < 28.0 would cut the sample roughly in half, reducing the constraining power of our observations.

The shaded region shows the 68% confidence range on the cumulative surface density, derived via Monte Carlo simulations inclusive of photometric and photometric redshift uncertainties, as well as sampling the Poisson uncertainty. We separately show estimated cosmic variance uncertainties at four different redshifts as the vertical error bars calculated based on the BLUETIDES simulation (Bhowmick et al. 2020, with caveats as discussed in F23). The dotted line shows the raw measurements with no correction. While not shown for clarity, the values from F23 lie at the low end of our posterior distribution here (which is consistent with our finding of ∼3.4× more galaxies in ∼2.6× more area).

We compare here to the same nine JWST model-based prelaunch predictions as in F23, including semianalytic models (SAMs; Dayal et al. 2017; Yung et al. 2019, 2020), empirical models (Behroozi & Silk 2015; Mason et al. 2015; Behroozi et al. 2019), and cosmological hydrodynamic simulations (Davé et al. 2019; Wilkins et al. 2023; Kannan et al. 2022, 2023). As discussed extensively in F23, the compilation of model predictions here is inclusive of several different modeling approaches and assumptions (see Somerville & Davé 2015 for a thorough review).

Similar to F23, we find that at $z < 10$ our observations are higher than most predictions, yet they are consistent with the Behroozi & Silk (2015) empirical and DELPHI SAM models, as well as the FLARES hydro predictions with no dust attenuation. At $z > 10$, we find that our results lie significantly above all predictions with the exception of Behroozi & Silk (2015). While this agreement is intriguing, this is not a physics-based model, but rather is based on the ansatz that the specific SFR in galaxies is proportional to the specific total mass accretion rate into halos. We thus confirm the initial result from F23 that the observed abundance of $z > 10$ galaxies discovered in CEERS lies above nearly all prelaunch predictions. Our result here is at higher confidence based on an updated sample ∼3× larger than the F23 sample.

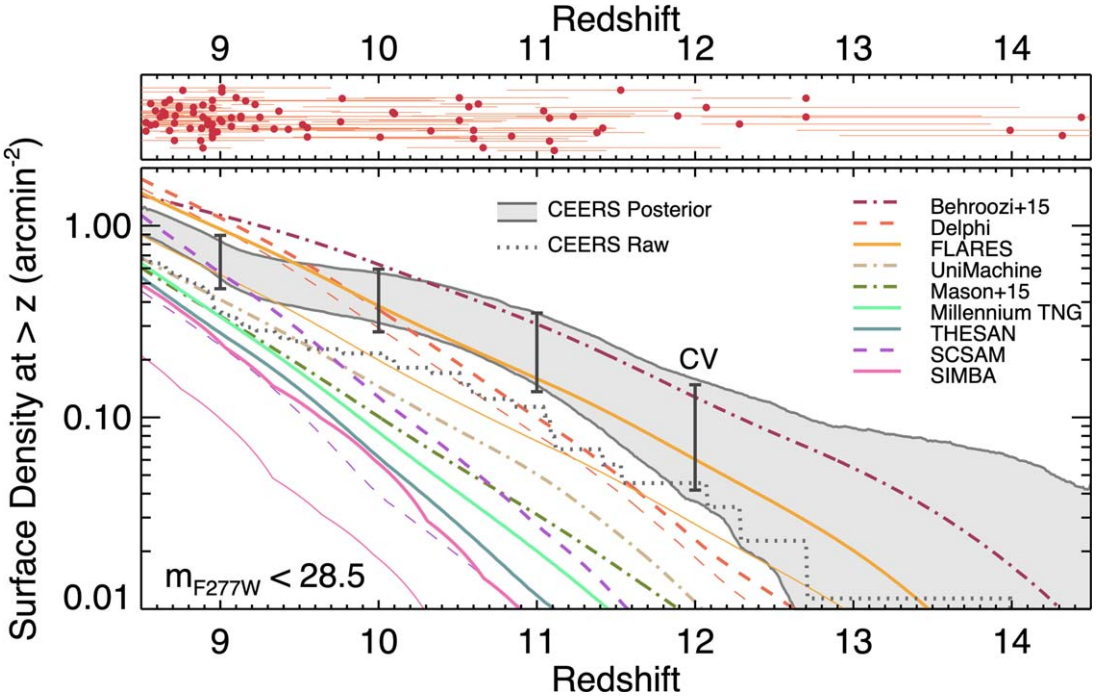

Figure 8. The top panel shows the redshift distribution of our sample (scattered vertically for clarity), while the main panel shows the cumulative surface density of galaxies per unit surface area at redshift greater than z for $m < 28.5$. The dotted line shows the raw counts from our CEERS $z > 8.5$ galaxy sample, while the shaded region shows the 68% confidence interval on the completeness-corrected surface density (including only sources with completeness estimates >20%), inclusive of photometric, photometric redshift, and Poisson uncertainties. The vertical error bars show the estimated cosmic variance uncertainty. The colored lines show predictions from a range of prelaunch simulations (including hydrodynamic, analytic, semianalytic, and semiempirical models), all also for $m < 28.5$. The observed surface density of galaxies lies above most predictions at $z > 10$, and above all except the Behroozi & Silk (2015) and FLARES models at $z > 11$. This confirms early results based on smaller samples that the observed abundance of $z \gtrsim 10$ galaxies significantly exceeds most prelaunch physically motivated expectations.

4.3. The Evolution of the Rest-UV Luminosity Function at z = 8.5–14.5

Here we present our measurements of the rest-frame UV luminosity function, measured separately for our $z \sim 9$, $z \sim 11$, and $z \sim 14$ samples, where galaxies are again placed into a sample based on their best-fitting photometric redshift (or spectroscopic redshift when available). Stacking the $\mathcal{P}(z)$ values of each sample (as shown in Figures 9 and 10), the median redshift in each bin is $z = 8.9$, 10.9, and 14.0, respectively. We note that our redshift bins become progressively wider for two reasons. First, at these redshifts, unity redshift bins become small in terms of cosmic time spanned. Second, our boundaries of $z = 9.7$ and $z = 13$ correspond to redshifts where the Lyα break falls directly between two NIRCam filters (between F115W and F150W and between F150W and F200W, respectively), thus creating natural redshift demarcations given our available data.

We measure our luminosity function following the methodology of F23, here using a bin size of 0.5 mag, with three key differences. The first is that here we use three redshift bins, and in the bin in common ($z \sim 11$) here our sample size is nearly $\sim 3\times$ larger (27, compared to 10 in F23). The second difference is our use of the size of the sources in the completeness correction, which, as shown in Section 4.1, can affect the inferred effective volumes (Figure 7). When calculating the effective volume, we first calculate the effective volume as a function of absolute magnitude and size by integrating over the comoving volume element as

$$V_{\rm eff}(M_{\rm UV}, r_h) = \int \frac{dV}{dz} C(z, M_{\rm UV}, r_h) dz, \quad (3)$$

where $C(z, M_{\rm UV}, r_h)$ is the completeness as calculated in Section 4.1. In each magnitude bin, we then calculate a final effective volume as the weighted mean of the effective volumes in all size bins weighted by the number of sources in that magnitude bin at a given size (corrected for the $\sim 1.5\times$ radius bias described in Section 4.1) as

$$V_{\rm final}(M_{\rm UV}) = \frac{\sum_i V_{\rm eff}(M_{\rm UV}, r_{h,i}) \times N(M_{\rm UV}, r_{h,i})}{\sum_i N(M_{\rm UV}, r_{h,i})}, \quad (4)$$

where i is a radius index and $N(M_{\rm UV}, r_{h,i})$ is the number of galaxies in a given UV magnitude and size bin.

The third difference comes when we estimate the number density in each bin via Markov Chain Monte Carlo (MCMC; see full details on this methodology in Finkelstein et al. 2015). We do this to sample galaxy absolute magnitude posterior distributions such that galaxies can fractionally span multiple magnitude bins. In F23 we treated each magnitude bin separately. Here, following Leung et al. (2023), each step in the MCMC chain samples the entire ensemble of galaxies for a given redshift bin, such that when a galaxy scatters out of one bin, it is accounted for in another bin (and thus is more realistic than what was done in F23).

Our measured number densities and final weighted mean effective volumes are listed in Table 4 for all three redshift bins. For bins with no galaxies, we list the 84% upper limit from the MCMC calculation. We also demarcate fainter bins with completeness values <20%; while we list these values, we caution that they are dominated by the completeness correction.

In Figure 9 we plot these luminosity function measurements compared to a wide range of literature results and

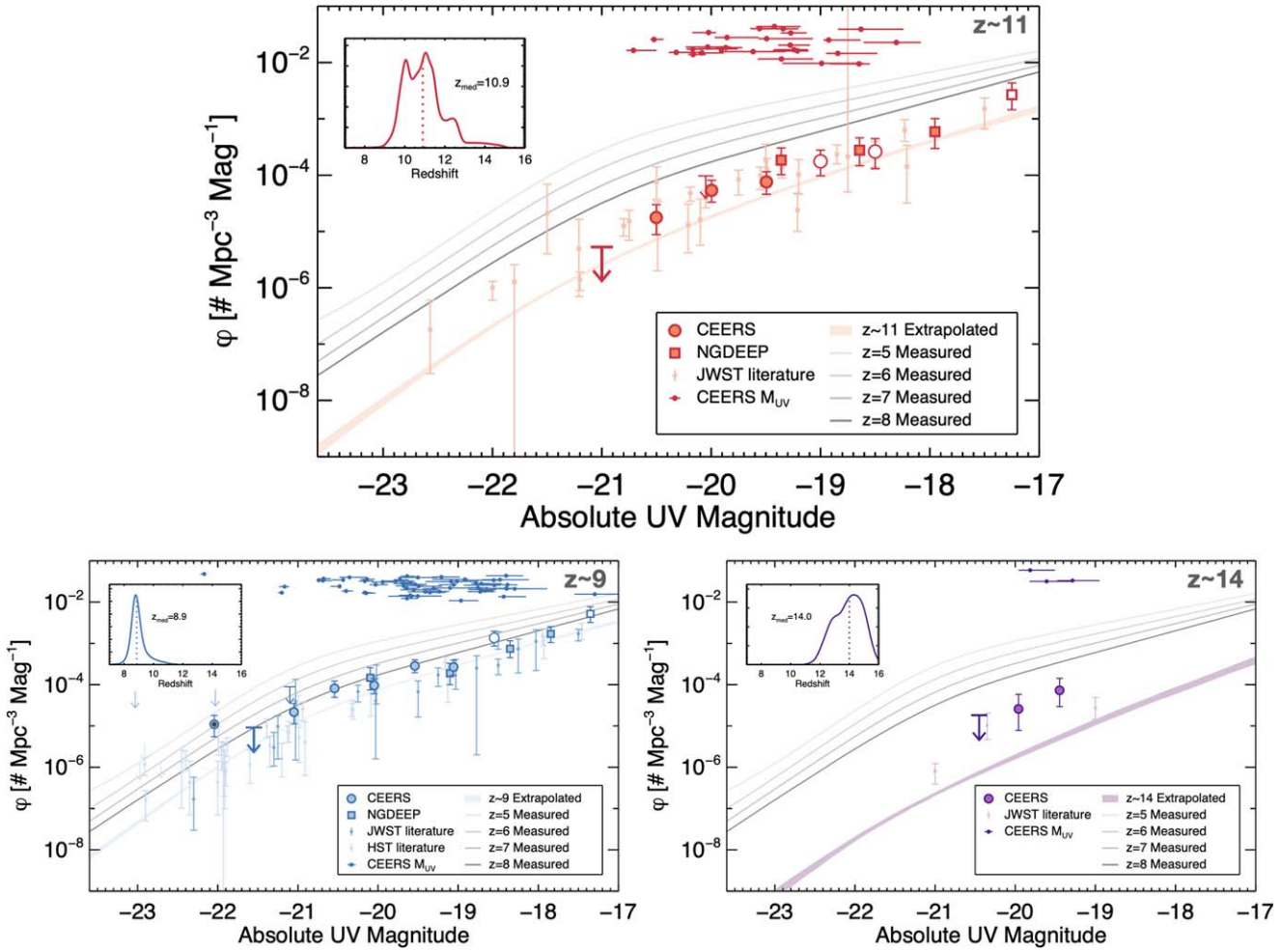

Figure 9. The evolution of the rest-frame UV luminosity function, at $z \sim 11$ ($9.7 < z_{\rm best} \leqslant 13$; top), $z \sim 9$ ($8.5 < z_{\rm best} \leqslant 9.7$; bottom left), and $z \sim 14$ ($13 < z_{\rm best} \leqslant 15$; bottom right). The large circles show the calculated number densities from our sample (the small red circles denote the magnitudes of individual galaxies, offset vertically for clarity), while the squares show the results from NGDEEP (Leung et al. 2023). The inset shows the stacked $\mathcal{P}(z)$ for each sample, with the dotted line denoting the median value of the $\mathcal{P}(z)$. Arrows show 1σ upper limits in the first bin with no galaxies, while white filled symbols denote bins that are <20% complete. The black circle in the brightest bin at $z \sim 9$ indicates that this bin has only one object, the $z = 8.7$ galaxy (which has AGN signatures) from Larson et al. (2022). Small symbols show literature results. At $z \sim 9$ the HST results are from McLeod et al. (2016), Morishita et al. (2018), Bouwens et al. (2019), Stefanon et al. (2019), Bowler et al. (2020), Rojas-Ruiz et al. (2020), Bouwens et al. (2021), Bagley et al. (2024a), and Finkelstein et al. (2022a), while the JWST results are from Harikane et al. (2023a), Bouwens et al. (2023b), Donnan et al. (2023a), Pérez-González et al. (2023b), and Adams et al. (2024). The $z \sim 11$ results shown are from Donnan et al. (2023b), Harikane et al. (2023a), Bouwens et al. (2023b), Donnan et al. (2023a), Pérez-González et al. (2023b), Adams et al. (2024), Casey et al. (2024), Castellano et al. (2023), Franco et al. (2023), and McLeod et al. (2024), while at $z \sim 14$ we compare to Donnan et al. (2023a) and Casey et al. (2024). The gray curves show the best-fitting DPL model from Finkelstein & Bagley (2022) from $z = 5$ to 8, while the light-shaded colored region shows this model empirically extrapolated to the median redshift for a given sample (where the width is the 68% uncertainty on the luminosity function at this redshift from Finkelstein & Bagley 2022). Our CEERS results are generally consistent with previous luminosity function estimates, with smaller uncertainties reflecting our larger sample size. We also note excellent agreement with the NGDEEP results where our samples overlap. Our brighter CEERS results sit above the expected number densities for the empirically expected extrapolation from Finkelstein & Bagley (2022), with this offset increasing to higher redshift.

extrapolations. In this figure we also prominently show the results from NGDEEP at fainter luminosities from Leung et al. (2023) at $z \sim 9$ and 11, as their photometry and sample selection process are nearly identical to our own (while we use the Leung et al. 2023 measured number densities here, we verified that the results would be very similar had we calculated the number densities with their sample in our slightly modified redshift bins). At $M_{\rm UV} = -19$, where our results overlap, we find excellent agreement between CEERS and NGDEEP, with the NGDEEP results then continuing on faintward at a consistent slope at both $z \sim 9$ and 11.

The small faded symbols in Figure 9 show results from the literature. At $z \sim 9$ we find broadly good agreement with these literature results (which come from HST, JWST, and ground-based studies). We note that our brightest bin is higher than previous results—this bin contains a single object, the $z \sim 8.7$ potential AGN from Larson et al. (2023a). Based on the confirmation of this object and another at a similar spectroscopic redshift, Larson et al. (2022) concluded that the EGS region is ∼4–10× denser than average at $z \sim 8.7$ (see also Whitler et al. 2024). While our unit redshift bin used here mitigates this overdensity somewhat, at the bright end, where numbers are small, our results are mildly higher than those from the literature, becoming broadly consistent at $M_{\rm UV} \gtrsim -20$. We do note that when considering the full CANDELS area (∼10× wider than we consider here), Finkelstein et al. (2022a) found a volume density ∼5× lower in the magnitude bin including this object.

At $z \sim 11$ we compare to a compilation of $z \sim 10$–12 results from the literature (Bouwens et al. 2023a; Donnan et al. 2023b;

Table 5
UV Luminosity Function Double Power-law Parameters

z	$\log_{10}\phi^*$ (Mpc^{-3})		M^* (mag)		β		α		log $\rho_{\rm UV,<-17}$ (erg s^{-1} Mpc^{-3} Hz^{-1})
	Prior	Posterior	Prior	Posterior	Prior	Posterior	Prior	Posterior	
9	$[-10,-1]$	$-4.4^{+0.6}_{-0.5}$	$[-22,-15]$	$-21.0^{+0.8}_{-0.5}$	$[-10,-3]$	$-4.9^{+1.5}_{-3.0}$	$[-5,-1]$	$-2.2^{+0.4}_{-0.3}$	$25.4^{+0.1}_{-0.1}$
11	$[-10,-1]$	$-4.4^{+0.8}_{-0.7}$	$[-22,-15]$	$-20.4^{+1.0}_{-0.7}$	$[-10,-3]$	$-5.1^{+1.6}_{-2.9}$	$[-5,-1]$	$-2.2^{+0.6}_{-0.4}$	$25.0^{+0.2}_{-0.2}$
14	$[-10,-1]$	$-4.8^{+0.3}_{-0.8}$	$M^*_{z=11}(\pm0.1)$	$-20.4^{+0.1}_{-0.1}$	$\beta_{z=11}(\pm0.1)$	$-5.1^{+0.1}_{-0.1}$	$[-5,-1]$	$-2.55^{+1.05}_{-1.40}$	$24.9^{+1.1}_{-0.7}$

Note. Constraints on the rest-UV luminosity function assuming a DPL form. We place priors on M^* and β at $z\sim14$ to match the values measured at $z\sim11$. The final column lists the specific luminosity density, obtained by integrating the luminosity functions at magnitudes brighter than -17.

Harikane et al. 2023a; Donnan et al. 2023a; Pérez-González et al. 2023b; Adams et al. 2024; Casey et al. 2024; Castellano et al. 2023; Franco et al. 2023; McLeod et al. 2024). While there is significant scatter, we find generally good agreement between our results and previously published values in the literature, though our larger sample size (than most studies) results in smaller uncertainties. We note in particular good agreement between our values and those from McLeod et al. (2024) and Adams et al. (2024), which are the only other previous studies to make use of the full CEERS area.

Each panel of Figure 9 also shows an empirical extrapolation of the UV luminosity function from Finkelstein & Bagley (2022). In this study, they fit an evolving double power-law (DPL) model to all available UV luminosity function data at $z=3$–9, assuming that the DPL parameters ϕ^*, M^*, β, and α vary smoothly with $1+z$ (they also simultaneously fit the evolution of the AGN UV luminosity function with a separate DPL, though at the magnitudes we consider here star-forming galaxies were found to dominate). In each panel we show the measured DPL fits at $z=5$–8 as the gray lines, with the extrapolation to a given redshift range shown as the light-shaded region (where for the extrapolations we used the MCMC chains from Finkelstein & Bagley 2022 to generate samples of the DPL parameters for each redshift). The upper and lower bounds show the median DPL at the upper/lower bound of the FWHM from the stacked $\mathcal{P}(z)$, as shown in the inset panels.

We show this more clearly in Figure 10, where we overplot both our measured number densities and these extrapolated luminosity functions for all three of our redshift samples. Based on prelaunch expectations of either a smoothly or rapidly declining luminosity function at $z>8$, we would expect to see our results fall either on or below these extrapolations. While the results at $z\sim9$ are consistent with this extrapolation (with the exception of the brightest points, which are affected by the known overdensity), we see clearly and significantly that our $z\sim11$ observed number densities lie modestly above this extrapolation, while the $z\sim14$ observed number densities lie even higher above their extrapolated region.

4.4. Double Power-law Fits

By combining with NGDEEP, we are able to sample 3–4 mag of dynamic range in $M_{\rm UV}$ at $z\sim9$ and $z\sim11$. We therefore fit a DPL function to our observations, following evidence that this functional form better represents the UV luminosity function at high redshifts than a Schechter function (e.g., Bowler et al. 2015, 2020; Finkelstein & Bagley 2022). We fit a DPL to each of our three redshift bins independently via an MCMC algorithm (following the methodology of Leung et al. 2023). We assign fairly uninformative priors on all

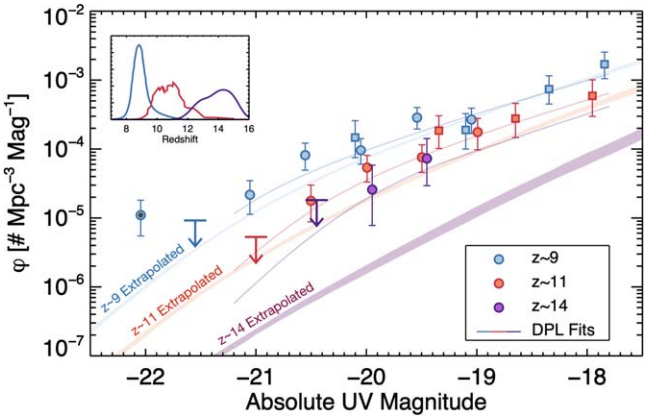

Figure 10. Our measured UV luminosity functions at $z\sim9$, 11, and 14 are shown by the large symbols (circles for our CEERS results, and squares for NGDEEP from Leung et al. 2023). The shaded regions are the same as in Figure 9, showing the extrapolated UV luminosity functions from Finkelstein & Bagley (2022). The inset panel likewise shows the same $\mathcal{P}(z)$ curves from Figure 9, here plotted on the same scale. The thin curves show the median DPL fit to the data at each redshift. This figure highlights that brighter galaxies ($M_{\rm UV}\lesssim-20$) have higher number densities than the extrapolated luminosity functions would predict. While there is a known overdensity at $z\sim8.7$ (Larson et al. 2022; Whitler et al. 2024) that could affect our lowest-redshift bin, there is no evidence for such overdensities at higher redshifts.

parameters at $z\sim9$ and 11; at $z=14$, due to our poor observational constraints, we fix M^* and β to the $z\sim11$ values (within a small tolerance). We list the priors and posterior results in Table 5. The median DPL fit is shown as the thin line in Figure 10. While this does a reasonable job of representing the data, the uncertainties, particularly on β and M^* at all redshifts and on the faint-end slope α at $z\sim14$, are currently quite large. We do note that our measured faint-end slope of -2.2 at $z=11$ is consistent with the value from Leung et al. (2023), though they imposed more restrictive priors on β and M^*, and thus our uncertainty is higher.

4.5. Evolution with Redshift

To explore the evolution in the UV luminosity function in more detail, in the left panel of Figure 11 we show our observed number densities for the CEERS bin closest to $M_{\rm UV}=-20$ at each of our three redshift bins, on top of the expectations for this number density from the Finkelstein & Bagley (2022) extrapolation. This figure clearly shows that the observed number densities diverge from the observed evolution at $z=3$–9, flattening at higher redshifts. We quantify this by measuring the slope ($d\log\phi/dz$) for both previous observations at $z=3$–9 and our results here at $z=9$–14. We find that this slope changes from $d\log\phi/dz=-0.29\pm0.03$ at $z=3$–9 to -0.11 ± 0.08 at $z=9$–14. Thus, while the abundance of

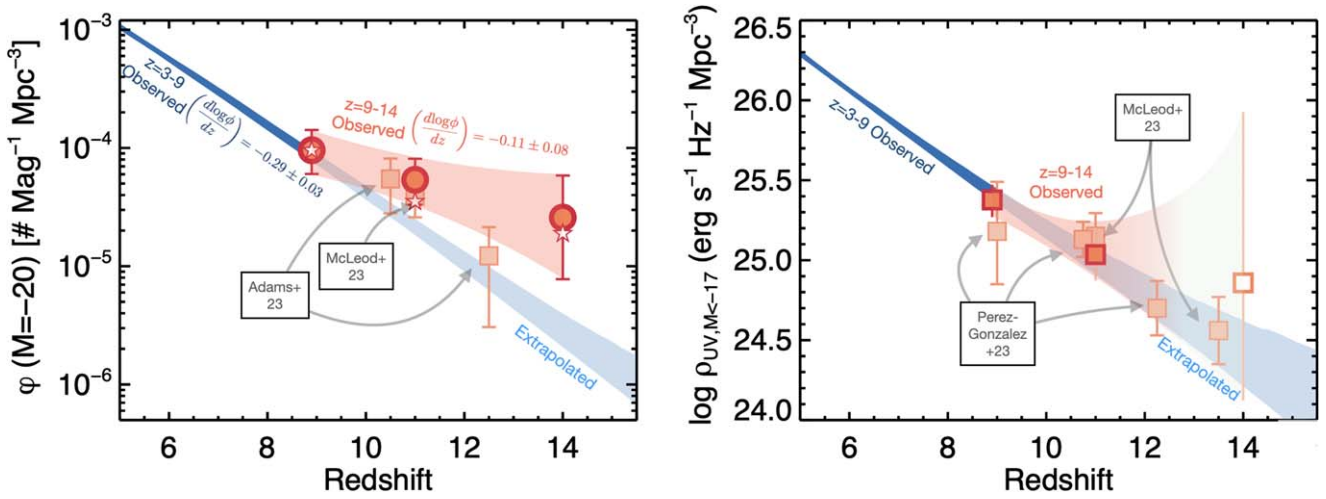

Figure 11. Left: the evolution of the observed number density at $M_{\rm UV} = -20$. The red circles show the observed number density at this absolute magnitude from CEERS (connected by the light-red shaded region; the small stars show the DPL fit values at this magnitude). The dark-blue region shows the measured value from Finkelstein & Bagley (2022), and the lighter-shaded region shows the extrapolation of the Finkelstein & Bagley (2022) results to higher redshift. While prelaunch expectations were that the number densities at $z > 9$ would either continue the observed trend at $z = 3$–9 or evolve more rapidly downward with increasing redshift, we find that the number density of bright galaxies surprisingly flattens at $z > 9$, where we measure a change in slope $d\log\phi/dz$ between $z < 9$ and $z > 9$ at 2.1σ significance. Right: the evolution of the integrated specific UV luminosity density, obtained by integrating DPL fits to our observed luminosity functions to $M_{\rm UV} = -17$. The evolution here is less clear, with increased uncertainties (particularly at $z \sim 14$, which is shown faded to represent its large uncertainty), making it less clear whether this quantity also has a flatter evolution at higher redshift.

bright ($M_{\rm UV} = -20$) galaxies evolves somewhat steeply at a constant slope at $z = 3$–9, this evolution is *flatter* toward higher redshifts at the 2.1σ significance level.

For this calculation we have used as our fiducial values the actual measured number densities at $M_{\rm UV} = -20$. In the left panel of Figure 11 we show as small stars the values of ϕ ($M = -20$) from the median DPL model at each redshift. The differences from the observed values are negligible at $z = 9$ and 14, while at $z = 11$ this parameterized value is slightly below the observed value at $z = 11$. Using these DPL values, the observed evolutionary slope steepens to $d\log\phi/dz = -0.18 \pm 0.07$ (reducing the significance of the flattening to 1.5σ).

This flattening in the observed evolution is also predicted by some recent models; as we discuss further below, the Ferrara (2024), SIMBA-EOR (Jones et al. 2024), and FIRE (Sun et al. 2023) simulations predict $z \sim 11$ UV luminosity functions consistent with our observations (Figure 12). While predictions at $z \sim 14$ are rare, the model of Ferrara et al. (2023) predicts an abundance of 10^{-5} mag^{-1} Mpc^{-3} at $M_{\rm UV} = -20$ at $z \sim 14$, consistent with our observational uncertainties.

To consider whether the evolution in the abundance of faint galaxies changes at $z > 9$, in the right panel of Figure 11 we show the specific UV luminosity density ($\rho_{\rm UV}$), obtained by integrating the UV luminosity function from our DPL fits to $M_{\rm UV} < -17$ (integrating each step of the chain to calculate the median and 68% confidence range); this quantity is dominated by the abundance of faint galaxies given the steep faint-end slopes (we note that we plot this quantity rather than the number densities at fainter magnitudes owing to the lack of constraints at $z \sim 14$, visible with the very large error at this highest redshift in the plotted integrated quantity). Interestingly, our measured specific UV luminosity densities at $z = 9$ and $z = 11$ are fully consistent with the extrapolated values (at $z \sim 14$ the poor constraints on the faint-end slope leave the uncertainty too large to reach definitive conclusions; thus, we show this as a faded data point). This can also be observed in Figure 10, as the faintest data points at $z \sim 9$ and 11 are consistent with the extrapolated luminosity function. A similar specific UV luminosity density is found by Pérez-González et al. (2023b), while McLeod et al. (2024) find a slightly elevated value, though consistent with the empirical extrapolation within the uncertainties.

Taking both panels of Figure 11 together, we find clear evidence that the evolution of the number density of bright galaxies is observed to flatten at $z > 9$, while the evolution of the integrated UV luminosity density, which is dominated by the abundance of fainter galaxies, is less clear and may possibly follow the lower-redshift evolutionary trend extrapolated to higher redshift. We discuss potential physical explanations for this intriguing result in the following section.

5. Discussion

In Section 4 we presented strong evidence that (i) the abundance of galaxies at $z > 9$ is in excess of nearly all pre-JWST launch simulation predictions, as well as above extrapolations from lower-redshift observations, and (ii) the evolution of the abundance of bright ($M_{\rm UV} = -20$) galaxies is flatter at $z = 9$–14 than at $z = 3$–9. Here we explore several potential explanations for these observations. Potential explanations could be due to galaxies being brighter than predicted or more numerous (e.g., horizontal evolution in the luminosity function rather than vertical). However, while the former is relatively easily achievable via a variety of reasonable physical modifications (as we discuss below), the latter would require major revisions to modern cosmology (e.g., more dark matter halos than expected), which we consider less likely.

5.1. Redshift Accuracy

One valid concern with early JWST studies is that selection techniques that worked well at lower redshift would begin to fail. In particular, while the physics behind Lyα-break-based selection should persist at these high redshifts, it is possible that

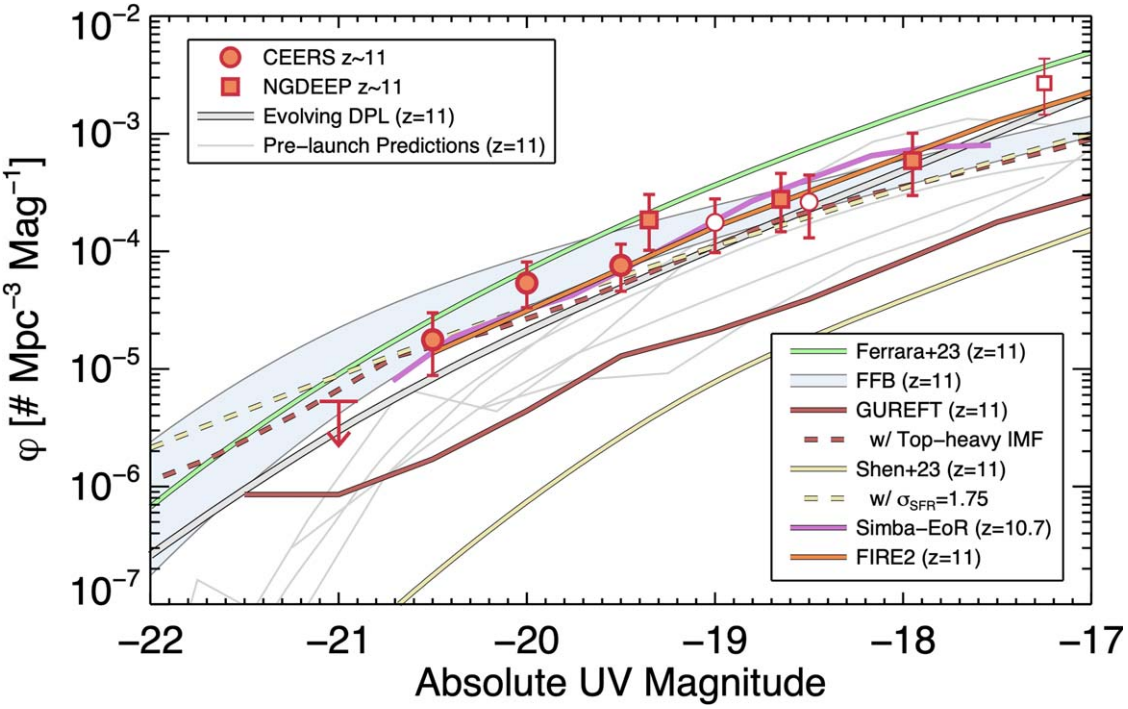

Figure 12. A comparison of the observed $z \sim 11$ UV luminosity function from CEERS and NGDEEP (symbols are the same as in the top panel of Figure 9) to model predictions. Prelaunch predictions from FLARES, DELPHI, UniverseMachine, THESAN, and BlueTides are shown as thin gray lines, while the colored lines show more recent predictions from Ferrara et al. (2023; green), Dekel et al. (2023; the blue shaded region shows a range of maximum SFE from 0.2 to 1), Shen et al. (2023; yellow; the dashed line includes a strong stochastic star formation component), Yung et al. (2024a; red; the dashed line indicates a top-heavy IMF UV luminosity enhancement of 3×), and Jones et al. (2024; purple). The thick gray line shows the empirical DPL luminosity function from Finkelstein & Bagley (2022) extrapolated to $z = 11$. These predictions show that a variety of potential physical solutions can predict a $z \sim 11$ luminosity function in agreement with observations.

heretofore-unknown populations of contaminants could have adverse affects. While one could model this contamination based on simulations, it relies on said simulations correctly modeling the colors of *all* potentially contaminating populations (e.g., Harikane et al. 2023a; Larson et al. 2023a), which is unlikely, particularly prior to JWST observations.

Spectroscopic validation of photometric redshifts is thus required. Unlike the past decade, when only the brightest HST $z > 6$ galaxies could have redshifts validated via either weak Lyα emission (e.g., Finkelstein et al. 2013; Oesch et al. 2015; Zitrin et al. 2015; Hoag et al. 2019; Jung et al. 2019, 2020; Larson et al. 2022) or Lyα breaks for the brightest sources (e.g., Oesch et al. 2016), JWST's spectroscopic capabilities allow easy rest-optical-based spectroscopic redshifts out to $z \approx 9.5$ (beyond which [O III] redshifts out of the NIRSpec window) and Lyα-continuum-based redshifts (with the NIRSpec prism mode) to arbitrarily higher redshifts (e.g., Arrabal Haro et al. 2023b; Fujimoto et al. 2023a; Arrabal Haro et al. 2023a; Fujimoto et al. 2023b; Curtis-Lake et al. 2023; Hainline et al. 2024).

As the CEERS spectroscopic component was observed in the second epoch *and* a DDT NIRSpec follow-up program was performed, a significant number of CEERS high-redshift candidates were spectroscopically observed in Cycle 1. Of our original sample of 93 candidate galaxies, 17 had NIRSpec spectroscopic observations, with redshifts originally presented in Larson et al. (2023b), Arrabal Haro et al. (2023b), Fujimoto et al. (2023a), Harikane et al. (2023a), and Arrabal Haro et al. (2023a). As discussed in Section 3.2.1, only 1 of the 17 had a "catastrophically" (defined as $|z_{\rm spec} - z_{\rm phot}|/(1 + z_{\rm spec}) > 0.3$) incorrect redshift (similar success was seen in the UNCOVER survey by Fujimoto et al. 2023b). Of the remaining 16, all had $z_{\rm spec} > 7.8$. We also note that four of the galaxies in our sample at $z_{\rm phot} > 9.7$ were spectroscopically observed by CEERS with no spectroscopic detection. For these sources, the absence of strong emission lines is plausibly consistent with $z_{\rm spec} > 9.6$. These results imply that it is unlikely that significant contamination from low-redshift galaxies is affecting our results (with the caveat that the sample of galaxies confirmed is as yet small and fairly biased toward brighter sources).

We next consider whether any smaller, yet nonnegligible, systematic offsets in redshift could play a role. A trend for the photometric redshifts to be overestimated at $z \gtrsim 8$ has been reported, with results from CEERS (Fujimoto et al. 2023a; Arrabal Haro et al. 2023a), JADES (Hainline et al. 2024) and UNCOVER (Fujimoto et al. 2023b) showing the photometric redshifts to be overestimated by $\langle \Delta z \rangle = 0.45$ (± 0.11), 0.26 (± 0.04), and 0.28 (± 0.33), respectively. As discussed in these studies, such offsets indicate a mismatch between the galaxy spectra and the adopted photometric redshift templates due to a variety of physical effects, including an increasing neutral fraction and/or enhanced DLA absorption (e.g., Heintz et al. 2023; Umeda et al. 2023).

For our specific sample of galaxies in this work (13 galaxies with $z_{\rm spec} > 8.5$), we find a median (mean) offset of $z_{\rm phot} - z_{\rm spec} = 0.1$ (0.3) with a standard deviation of 0.2. As discussed in Section 3.2.1, our sample excludes three galaxies selected with $z_{\rm phot} > 8.5$ with $z_{\rm spec} \sim 8$; including these objects does not change the median offset, but it does increase the mean offset (to 0.5) and the standard deviation (to 0.3). These three objects in particular highlight the difficulty of working at $z \lesssim 9$ within the CEERS data set due to the bluest JWST filter being F115W. Upcoming F090W imaging from PID 2234 (PI Bañados) will improve this situation, probing below the Lyα

break at $z \sim 8$. At present these larger $\Delta z \sim 1$–2 offsets affect only a small fraction (3/16) of the spectroscopic sample. Should these larger offsets exist in the rest of the nonconfirmed sample, the instances of these objects we do see imply that it would primarily affect the $z \sim 9$ results (though we note that ID = 4777 [$z_{\rm spec} = 7.993$] is in the $z \sim 11$ galaxy sample, though it has a very broad $\mathcal{P}[z]$).

We simulate the potential impact of these systematic redshift offsets by remeasuring our observed luminosity function values in the same MCMC manner as above, where in each step of the MCMC chain we assign simulated spectroscopic redshifts for each object. For objects that already have spectroscopic redshifts, we keep those values. For the remaining objects, we draw randomly from the observed Δz ($=z_{\rm phot} - z_{\rm spec}$) distribution, adding Δz to the photometric redshift to simulate a (potentially biased) spectroscopic redshift. For each new "$z_{\rm spec}$," we remeasure a new value of $M_{\rm UV}$. We perform this redshift assignment and subsequent SED-fitting-based $M_{\rm UV}$ measurement prior to running the MCMC chain, precomputing 100 random draws of Δz and the corresponding $M_{\rm UV}$, and then drawing from these precomputed values randomly at each step of the chain. Through this process we simulate both the effect of the potential redshift bias on the specific galaxy samples (as objects can move between redshift bins, potentially lowering the median redshift) and the impact on the absolute magnitudes (due to changes in the distance modulus). Both effects can combine to affect the number density, though the former is the larger effect, as the difference in the distance modulus for $\Delta z = 0.3$ (1) at $z = 11$ is only ∼0.04 (0.13) mag.

First, we examine the impact on the median redshift in each bin, which we find to be fairly minimal: $z_{\rm med} = 8.9$, 10.9, and 14.2 (unchanged for the $z \sim 9$ and $z \sim 11$ bins, and 0.2 higher in the $z \sim 14$ bin). The corresponding impact on the number densities at $M_{\rm UV} = -20$ is also modest, with these values being 12%, 14%, and 36% lower at $z \sim 9$, 11, and 14, respectively. Measuring $d\log\phi/dz$ using both these new median redshift values and the corresponding simulated number densities, we find $d\log\phi/dz = -0.14 \pm 0.09$ over $z = 9$–14, not significantly different from our fiducial value of -0.11 ± 0.08. We note that while for this exercise we restricted the Δz sample to $z_{\rm spec} > 8.5$, we found that including the three $z_{\rm spec} \sim 8$ galaxies did not change the results.

We thus conclude that the measurable redshift bias from the available spectroscopic confirmations is unlikely to be the primary cause of the observed change in slope at $z > 9$ in the evolution of the abundance of bright galaxies. We acknowledge again that the existing number of spectroscopic redshifts is small and biased toward primarily bright sources. In addition, some of these redshifts come from the Lyα break only, and these values have been measured to be up to $\Delta z \sim 0.2$ different from more secure emission-line-based redshifts (Fujimoto et al. 2023b). Larger samples of spectroscopic confirmations of galaxies in this epoch are needed to increase confidence that any redshift bias does not affect the measured number densities.

5.2. AGN Contribution

Accreting supermassive black holes, particularly when they are not obscured from view, can emit quite strongly in the rest-UV (e.g., Stevans et al. 2014). While the contribution of AGN light to the rest-UV emission from high-redshift galaxies has been fairly unconstrained, some notable examples do exist at $z \sim 7$ (e.g., Fujimoto et al. 2022; Endsley et al. 2023a). However, the evolution in the AGN UV luminosity function suggests that AGNs do not dominate the rest-UV emission in galaxies (e.g., nonquasars) at high redshift (e.g., Finkelstein & Bagley 2022). However, with JWST's spectroscopic abilities, it is worth revisiting whether AGNs could be contributing significantly to the UV emission from galaxies.

Early observations hint that growing supermassive black holes are indeed somewhat common at $z \sim 5$–9, with signs of potential AGN activity found in dozens of galaxies (e.g., Harikane et al. 2023b; Bogdan et al. 2024; Kocevski et al. 2023; Labbe et al. 2023; Larson et al. 2023a; Leung et al. 2023), with several sources containing spectroscopically confirmed broad-line AGNs (e.g., Maiolino et al. 2023; Harikane et al. 2023b; Furtak et al. 2024; Greene et al. 2024; Kocevski et al. 2023; Kokorev et al. 2023; Larson et al. 2023a; Matthee et al. 2024). While this may suggest that AGNs could contribute to the UV luminosity, many of these sources have unique two-component SEDs with fairly flat UV spectral slopes, with a change to a steeply rising red slope in the rest-UV optical (e.g., Barro et al. 2024; Kocevski et al. 2023; Labbe et al. 2023; Matthee et al. 2024). While an AGN jet could trigger enhanced star formation (e.g., Duncan et al. 2023), here we aim to assess whether the UV emission we observe is dominated by emission from an AGN accretion disk. For these red AGNs in particular, the point-source morphology in the longest-wavelength bands strongly suggests that obscured AGN light is dominating the rest-optical emission, while advanced SED modeling is needed to robustly constrain the amount of AGN contribution to the rest-frame UV. Such a contribution remains possible, as scattered UV light from a partially obscured AGN could in theory contribute to the observed UV emission (e.g., Barro et al. 2024; Greene et al. 2024; Kocevski et al. 2023; Labbe et al. 2023), though the resolved nature of the rest-UV emission in these galaxies indicates that stellar emission may dominate.

AGNs have also recently been identified in objects with more typical galaxy-like morphologies and SED slopes. Larson et al. (2023a) inferred the presence of an AGN in a $z = 8.7$ galaxy (via a 2.5σ significant broad Hβ line) and noted that the SED has a flat slope through the rest-near-infrared (aided by MIRI observations; Papovich et al. 2023), suggesting that stellar light is dominating at all observed wavelengths. Maiolino et al. (2024) inferred via extremely high gas densities that the nucleus of the well-known galaxy GN-z11 (at $z = 10.6$) likely hosts an AGN; analysis of this object by Tacchella et al. (2023a) shows that 2/3 of the rest-UV continuum emission emanates from the nucleus, hinting that this object could be AGN dominated in the UV. Harikane et al. (2023b) discuss 11 confirmed broad-line AGNs in the CEERS and found that the majority of them showed extended morphologies in the rest-UV (with most of the rest being extremely UV-faint reddened AGNs), suggesting that much of the rest-UV emission is stellar in origin. Although some of these observations indicate that the AGN contribution to the total UV luminosity is negligible, this might not always be the case, depending on the phase of the AGN duty cycle (which affects the contrast between the AGN and the host galaxy). A possible high AGN fraction has been suggested in the recent NIRSpec follow-up for lensed galaxies at $z = 8.5$–13.2 (Fujimoto et al. 2023b).

These early observations do not yet collectively paint a clear picture of the contribution of AGNs to the rest-frame UV

emission from early galaxies. It is clear that AGNs exist in these epochs, though many discovered so far appear to be primarily obscured. Deciphering the relative contribution from stars and AGNs to the emergent UV emission, including constraining the extent to which scattered UV light from obscured AGNs plays a role, will require a combination of more advanced SED modeling techniques along with deep $\sim$1–2 μm spectroscopy. Until such analyses can be conclusively done, AGNs remain a possible scenario to explain the high abundance of bright galaxies at early times.

5.3. Change in Physical Processes

The remaining explanations for the observed UV luminosity enhancement involve changes in the physical processes regulating the ratio of observed UV light to the halo masses of these galaxies. We further explore this here, aided by a variety of recent theoretical results motivated by early JWST observations of the $z > 9$ Universe, summarized in Figure 12. This figure compares our observed UV luminosity function (combined with that of NGDEEP) to recent predictions from Ferrara et al. (2023), Yung et al. (2024a), Dekel et al. (2023), Shen et al. (2023), Sun et al. (2023), and Jones et al. (2024). We also compare to prelaunch predictions from FLARES (Vijayan et al. 2021; Lovell et al. 2021; Wilkins et al. 2022), DELPHI (Dayal et al. 2017), UniverseMachine (Behroozi et al. 2020), THESAN (Kannan et al. 2022), and BlueTides (Feng et al. 2016; Wilkins et al. 2017). In this figure we compare our observations to these model predictions made at $z = 11$ when possible (when not, we interpolate the number densities in log space), as this is the median of the stacked redshift probability distribution for the galaxies that make up our luminosity function sample (see inset panel of Figure 9). We note that differences between models can be due both to the underlying methodology and/or subgrid physics and to the procedures used to generate observed luminosities.

5.3.1. Significant Evolution in Attenuation

Ferrara et al. (2023) have developed a physical model that successfully reproduces the observed $z = 7$ UV luminosity function via a dust implementation that is designed to match both the shape of the UV luminosity function and the $z \sim 7$ obscured SFR results from the ALMA REBELS survey (Bouwens et al. 2022). Evolving their model to higher redshifts, they naturally predict a slowing in the evolution of the UV luminosity function from $z \sim 9$ to 11 due to significantly reduced attenuation in galaxies. This arises in their model owing to outflows driven by very high ("super-Eddington") specific SFRs, which can efficiently drive gas (and dust) out from these galaxies (Ferrara 2024). They discuss that this is supported by the data, as early results on the colors of $z > 8$ galaxies showed that they were fairly blue (e.g., Finkelstein et al. 2022b; Topping et al. 2022; Cullen et al. 2023; Papovich et al. 2023) and thus likely contained little dust.

As shown in Figure 12, this model does significantly better than prelaunch simulations, in fact slightly overpredicting the observed UV luminosity function. We thus explore whether significant color evolution is observed, particularly in modestly bright galaxies, which could further support this model. To study potential evolution with redshift, we select a sample of galaxies from the CEERS catalog at $z \sim 6$–8. The sample selection was identical to that done here for $z > 8.5$, simply evolving the redshift cuts to lower redshift (primarily requiring $\int \mathcal{P}(z > 4) \geqslant 0.7$, $z_{\rm best} > 5.0$, and $\mathcal{S}_z = 6$, 7, or 8). The full sample of >2000 sources was visually inspected, resulting in a final sample of 1018, 574, and 224 galaxies at $z \sim 6$, 7, and 8, respectively.

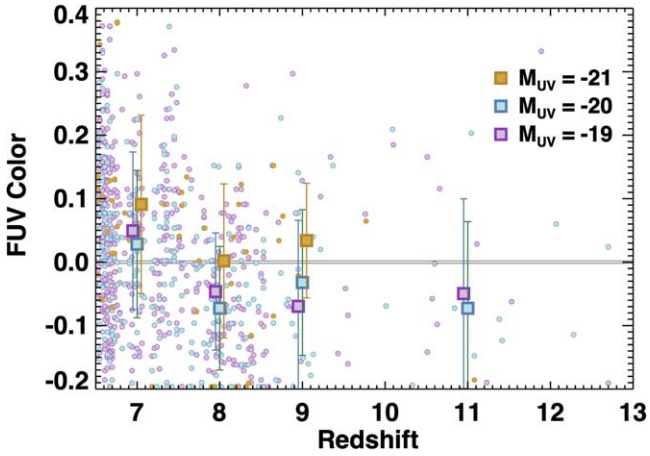

Figure 13. The evolution of the FUV color $\mathcal{C}_{\rm FUV}$ with redshift, color-coded by $M_{\rm UV}$. The large squares show median values in bins of redshift and magnitude (error bars show the 1σ spread), for bins with $\geqslant$5 sources. While reddened galaxies exist at $z \sim 7$–8, the median colors are still fairly blue. Notably, the median FUV color for $M_{\rm UV} = -20$ galaxies is similar at $z \sim 8$ to $z \sim 11$, suggesting that a significant drop in dust attenuation is unlikely to explain the high abundance of bright $z \sim 11$ galaxies.

As discussed in Section 3.3, we defined a rest-far-UV color $\mathcal{C}_{\rm FUV}$ and calculated it for galaxies in both our $z > 8.5$ and $z = 6$–8 galaxy samples. We note that a change of $\Delta\mathcal{C}_{\rm FUV} = 0.05$ is equivalent to $\Delta A_V = 0.1$ (under the assumption of a Calzetti et al. 1994 dust law). In Figure 13 we plot $\mathcal{C}_{\rm FUV}$ versus redshift, color-coded by $M_{\rm UV}$. We plot the median in bins of redshift ($z = 6.5$–7.5, 7.5–8.5, 8.5–9.7, and 9.7–13), and while there is significant scatter in color at all redshifts, the median color is fairly blue. Focusing on the middle magnitude bin ($M_{\rm UV} = -20$), where our results have the strongest constraining power (too few brighter galaxies exist at $z > 9$ to make conclusions), we see that the median FUV color does not significantly evolve from $z \sim 8$ to $z \sim 11$ ($\mathcal{C}_{\rm FUV} = -0.07$ at both redshifts, with a scatter of $\sim$0.1).

This initial exploration into the evolution of UV colors does not support rapid changes in the evolution of the attenuation at $M_{\rm UV} = -20$ between $z \sim 8$ and 11. Rather, the majority of the $z > 6$ galaxies in our sample appear to have little dust even at $z \sim 7$–8. This is consistent with the results of Papovich et al. (2023), who showed that with the inclusion of MIRI photometry typical galaxies at $z > 7$ are fairly blue. Should this mild color evolution be confirmed by larger galaxy samples, it implies that rapid dust removal is likely not the dominant cause of the observed UV luminosity function evolution, though evolution from little dust to no dust likely plays some role. We do note that finding so little dust is in itself a puzzle, as these galaxies should have made significant amounts of dust in the process of building their observed stellar masses. Though UV-faint dusty sources may indeed exist in this epoch (Rodighiero et al. 2023), in our UV-selected sources the dust must get destroyed (via, e.g., reverse shocks in supernovae), or be removed via winds even down to $z \sim 7$ in these sources. We acknowledge, however, that the scatter in $C_{\rm FUV}$ is large and that more advanced UV spectral slope

modeling with larger samples covering a wider dynamic range in stellar mass and $M_{\rm UV}$ can provide further insight.

5.3.2. Change in Conversion from Mass to UV Luminosity

If reduced attenuation is unlikely to be the dominant effect explaining the discrepancy between models and observations, then it is prudent to consider changes in the processes of star formation that could result in enhanced UV luminosities. A very straightforward potential explanation could be a change in the IMF. As discussed by F23 and Harikane et al. (2023a), a change in the characteristic stellar mass from $\sim$1 to $\sim$10 $M_{\odot}$ is expected when the cosmic microwave background temperature is higher and the gas metallicities are lower (e.g., Larson 1998; Bromm et al. 2002; Tumlinson 2006; Steinhardt et al. 2023). Such a change would decrease the mass-to-UV-light ratio by factors of up to several (e.g., Raiter et al. 2010; Zackrisson et al. 2011).

As one example of this, we show the new SAM predictions based on merger trees from the GUREFT simulation suite (Yung et al. 2024a, 2024b). This is an update to the "Santa Cruz SAM" predictions (Somerville et al. 2015; Yung et al. 2019), now using *N*-body-based merger trees constructed with finely spaced snapshots at very high redshift to better capture halo growth at early times. Their fiducial model still underpredicts the observations, implying that the extended Press–Schechter based merger trees used in the previously published models were not the sole reason for the discrepancy. However, as they discuss in their paper, the shape of their UV luminosity function appears consistent with the data. They show that if they decrease the mass-to-light ratio by a factor of $\sim$3 (dashed line), as would be plausible for a top-heavy IMF, their model becomes consistent with the observations.

A smaller UV luminosity enhancement of only $\sim$1.5$\times$ would be needed to bring the empirically extrapolated DPL UV luminosity function from Finkelstein & Bagley (2022) at $z = 11$ (thick gray line) into agreement with our observations. However, the discrepancy with this empirical extrapolation is greater for brighter galaxies than for fainter galaxies, such that a flat UV luminosity boost at all magnitudes would lead to an overprediction of the faint end owing to the empirically predicted faint-end slope being steeper ($\alpha = -2.5$) than that observed from NGDEEP ($\alpha = -2.2$). While our results cannot constrain the IMF currently, deep rest-UV spectroscopic observations could be capable of detecting high-ionization lines such as He II or [Ne V], which could indicate the presence of very massive stars in these galaxies (e.g., Tumlinson & Shull 2000; Bromm et al. 2001; Schaerer 2003; Olivier et al. 2022; Cleri et al. 2023).

One caveat to an increased light-to-mass ratio due to a top-heavy IMF would be that it would be accompanied by an increased feedback-to-mass ratio, because the massive stars that produce UV light are also those that produce energetic radiation, strong stellar winds, and Type II supernovae. Changing the IMF would also change the integrated chemical yields, which could impact cooling. The models above have yet to self-consistently model the increased feedback and modified chemical yields of a top-heavy IMF for high-redshift galaxies. However, other studies (e.g., Fontanot 2014) have found that evolving top-heavy IMFs (e.g., top-heavy IMFs for galaxies with high SFRs) have tended to decrease the mass of stars formed relative to models with universal IMFs.

5.4. High Star Formation Efficiency

Even without a change in the IMF, the UV luminosities of very high redshift galaxies could be enhanced if the rates of gas conversion into stars were increased. As discussed in F23, most models adopt fairly long gas depletion timescales, based on observations of nearby galaxies. While perhaps a coincidence, it is interesting that among the pre-JWST predictions only the Behroozi & Silk (2015) model, which assumes a negligible gas depletion timescale, can match the observations in Figure 8. The physical processes that may lead to a decrease in this timescale are not currently obvious, though as the dependence of star formation with gas density (Schmidt 1959; Kennicutt 1998) is superlinear (e.g., Vallini et al. 2024), the very high gas densities present in early-Universe halos likely play a role. Very high efficiency star formation has been observed in super star clusters in local galaxies (e.g., Turner et al. 2015; Smith et al. 2020; Costa et al. 2021). The high cloud surface densities in the environments of these super star clusters, which are rare in the nearby Universe, could be common in galaxies at $z > 9$. Theoretical work on molecular cloud scales has also shown that both stellar winds and radiation feedback may become ineffective at very high cloud surface densities, leading to higher cloud-scale star formation efficiencies (Grudić et al. 2020; Lancaster et al. 2021; Menon et al. 2023).

In this context, we explore two additional predictions. The first is an updated version of the SIMBA model (Davé et al. 2019) known as SIMBA-EOR (Jones et al. 2024). This simulation includes a new subgrid ISM model that coevolves dust and H_2 by explicitly tracking all formation and destruction mechanisms, which turns out to yield more H_2 at low metallicities relative to SIMBA. This leads to earlier star formation in halos, increasing the luminosities of early galaxies compared to SIMBA (which, as shown in Figure 8, significantly underpredicts $z > 9$ observations). The SIMBA-EOR predictions are well matched to the CEERS observations, despite no specific tuning to EoR data, though the faint-end slope appears higher than that observed. It is worth noting that the galaxies are not predicted to be dust-free; without accounting for extinction, the Simba-EoR predictions would be clearly above the observations.

We also compare to the Feedback-Free Starburst (FFB) physical model introduced by Dekel et al. (2023), using the luminosity function, including a dust attenuation prescription, presented in Li et al. (2023). This model predicts that in massive galaxies at $z \sim 10$, where the gas density is above a threshold of $\sim 3 \times 10^3$ cm^{-3} and the gas-phase metallicity is below $\sim$0.2 $Z_{\odot}$, star formation in thousands of globular-cluster-like clouds is expected to proceed on a freefall timescale shorter than the $\sim$2 Myr interval between a starburst and the onset of effective stellar and supernova feedback, thus allowing high SFE free of suppression by feedback.[47] In Figure 12 we show as the blue shaded region the predictions of this model with a maximum SFE ranging from 20% (lower bound) to 100% (upper bound). These predictions match our observations reasonably well over the range where we detect galaxies. This model predicts an enhanced bright end owing to the predicted high SFE preferentially at high halo masses, aided by the fairly

[47] See also Renzini (2023), who proposes a related picture in which stars above 20 $M_{\odot}$ collapse directly to black holes, thereby failing to deposit energy in the ISM.

low levels of dust attenuation and the high level of star formation stochasticity predicted in the FFB phase.

5.4.1. Stochastic Star Formation

In Section 4 we presented Figure 11, which showed that the evolution of the abundance of bright galaxies appears to flatten at $z > 9$, while the specific UV luminosity density (integrated to $M_{\rm UV} = -17$) is not inconsistent with evolution with a consistent slope from lower redshift. It is important to note that currently these integrals are uncertain—the observations are also consistent with an elevated value at the faint end within the uncertainties. Future work combining the available deep fields (NGDEEP, MIDIS, JADES, etc.) will soon improve these constraints. Should these future studies conclude that any flattening evolution is observed primarily at brighter luminosities, we comment here on possible physical drivers of such a differential evolution. First, should any of the processes discussed above be at play primarily in more massive halos, it could lead to a preferentially enhanced abundance of bright galaxies. However, it seems unlikely that there would be dramatic differences in the SFE or IMF across a fairly limited dynamic range of UV absolute magnitudes (and thus presumably halo mass).

One plausible explanation for the observed behavior could be a significant increase in the stochasticity of star formation (e.g., Mirocha & Furlanetto 2023; Shen et al. 2023; Sun et al. 2023). As shown by Shen et al. (2023), introducing a variability in the conversion from halo mass to UV luminosity (which could encompass both star formation stochasticity and variations of dust attenuation, metallicity, etc.) leads to an "upscattering" in the UV luminosity function. Due to the steep faint-end slope, more galaxies will scatter from faint to bright luminosities than from bright to faint luminosities, which can lead to a shallower bright end (in an effect similar to Eddington bias). They explore a range of scatter values (encompassed by the variable $\sigma_{\rm UV}$, which describes the Gaussian width of the kernel scattering the UV luminosities). As we show in Figure 12, $\sigma_{\rm UV} = 1.75$ yields a predicted UV luminosity function in good agreement with our observations, though it does overpredict abundances at $M_{\rm UV} \leqslant -21$. Pallottini & Ferrara (2023) explored the level of stochasticity present within their high-resolution hydrodynamic simulations and found that while stochasticity was present, it was at a lower level, equivalent to $\sigma_{\rm UV} \sim 0.6$. This is just one simulation, so it remains to be seen whether higher levels of stochasticity are plausible. We also note that when stochasticity is not included, the fiducial UV luminosity function of the empirical Shen et al. (2023) model is quite low (solid gold line in Figure 12). Taking, for example, the UV luminosity function from the physics-based Santa Cruz GUREFT SAMs (Yung et al. 2024a), lower levels of UV scatter would be needed to match the observations, plausibly more consistent with simulation results.

In Figure 12, we also include predictions from Sun et al. (2023) from the FIRE simulation, which are in excellent agreement with our observations. In these simulations, intrinsic mass- and redshift-dependent burstiness arises naturally owing to their self-consistent modeling of stellar feedback. Rather than fine-tuning a specific burstiness parameter, they find that the distribution of UV luminosities at fixed galaxy stellar mass significantly widens at lower masses. Interestingly, this paper is based on the models from Ma et al. (2018), which were run prior to JWST observations; thus, this model was not tuned to match observations like those presented here.

Observational evidence is emerging that high-redshift galaxies have significant variability in their SFRs. Looser et al. (2024) discovered a surprisingly quiescent galaxy at $z = 7.3$, which shows evidence for a ∼10–20 yr lull in star formation activity after a recent burst. They extended this study in Looser et al. (2023), finding with a spectroscopic analysis that lower-mass galaxies at high redshift have particularly bursty star formation histories. Endsley et al. (2023b) came to a similar conclusion after analyzing the photometry of a much larger sample of galaxies, finding that fainter galaxies at higher redshifts show lower [O III] equivalent widths than their brighter counterparts, which they interpret as evidence that the brightest galaxies are frequently experiencing a recent upturn in star formation activity (see also Tacchella et al. 2023b). Ciesla et al. (2024) also found evidence for increased stochasticity at high redshift, finding that galaxies in the JADES field appear to transition from predominantly secular modes of star formation to stochastic at $z \gtrsim 6$. Their observed $\sigma_{\rm UV} \sim 1.2$ is less than that needed to reconcile the models of Shen et al. (2023), though it is larger than the values predicted by Pallottini & Ferrara (2023). Lastly, Cole et al. (2023) found evidence for increased scatter in the star-forming main sequence at $z = 5$–9, also consistent with increasing levels of star formation stochasticity.

While evidence thus far indicates that galaxies at higher redshifts and lower masses may host more variable star formation histories, we cannot yet conclude whether this is the major physical driver of the slower-than-expected evolution of the UV luminosity function at brighter luminosities. Deep JWST/PRISM spectroscopy could yield a data set capable of constraining star formation histories via SED modeling. Another interesting test to constrain this possibility was proposed by Muñoz et al. (2023), who noted that if variability in the ratio of UV luminosity to halo mass was significant, many UV-bright galaxies would exist in lower-mass halos, which could be distinguishable via a weaker clustering strength than if there were a more direct correlation between UV luminosity and halo mass. Such a measurement would require a wide and deep photometric survey capable of identifying a sufficient source density of $z > 10$ galaxies. This may be possible with COSMOS-Web (PID 1727, PIs Kartaltepe & Casey; Casey et al. 2023) and will certainly be possible with deep-field observations with the Nancy Grace Roman Space Telescope (in particular with the added K_s filter).

6. Conclusions

We have presented the results of a comprehensive search for $z > 8.5$ galaxies in the full NIRCam data set from the Cosmic Evolution Early Release Science survey. We created a new photometric catalog aimed at measuring accurate colors for faint galaxies, as well as robust estimates of the total flux, implementing multiple key improvements over our previous work (Finkelstein et al. 2023). We identify a sample of 88 candidate $z > 8.5$ galaxies, with 55 galaxies in our $z \sim 9$ sample (selected over $8.5 < z < 9.7$), 27 galaxies in our $z \sim 11$ sample (selected over $9.7 < z < 13$), and 3 galaxies in our $z \sim 14$ sample (selected over $13 < z < 15$). Notably, 13 of our galaxies are spectroscopically confirmed: 8 in the $z \sim 9$ sample ($z_{\rm spec}$ =8.63–9.00), and 5 in the $z \sim 11$ sample ($z_{\rm spec}$ = 9.77–11.42).

We perform advanced source injection simulations to assess our source completeness, accounting for both photometric and photometric redshift recovery, explicitly accounting for the sizes of our sources. While the impact of this update is minimal for bright ($M_{\rm UV}\sim -21$) galaxies, it does result in modestly (10%–30%) lower effective volumes than the assumption of a point source at fainter ($M_{\rm UV}\sim -19.5$) luminosities.

We use these completeness estimates to first compare the cumulative surface density of galaxies in our sample to a variety of pre-JWST-launch simulation predictions, finding that the observed abundance of galaxies is higher than any physical model prediction at $z>10$, with this tension increasing with increasing redshift. Our results are in the least tension with the empirical model of Behroozi & Silk (2015), which posits that the specific SFR tracks the specific halo accretion rate; at these high redshifts this would imply very short timescales for star formation. While it remains to be seen whether this is physical, it would be consistent with the observed abundance of UV-bright galaxies.

We calculate the rest-UV luminosity function in our three redshift bins. Comparing to previous results, we find general agreement, though our uncertainties are typically smaller owing to our larger sample sizes. Notably, we see evidence of the known $z\sim 8.7$ overdensity in the EGS field (Finkelstein et al. 2022a; Larson et al. 2022; Whitler et al. 2024) in the brighter bins of our $z\sim 9$ UV luminosity function.

We analyze the evolution of the UV luminosity function from $z\sim 9$ to $z\sim 14$ in two ways. First, we examine the evolution of galaxies at $M_{\rm UV}=-20$. While the abundance of galaxies at this fixed UV luminosity has been conclusively measured to rise smoothly from $z=9$ to 3, we find evidence for a significant flattening. Extrapolating the observed evolution from $z=9$ to 3 to higher redshifts, one would expect the abundance of galaxies to rise by a factor of $\gtrsim$20 from $z\sim 14$ to $z\sim 9$. Conversely, we measure a rise of 4.3 ($\pm$3.7) over this epoch. Phrasing this another way, $d\log\phi/dz=-0.29\pm 0.03$ at $z=3$–9, while we find -0.11 ± 0.08 at $z=9$–14. We also explore the total integrated specific UV luminosity density, fitting DPL models to our observed luminosity functions and integrating to $M_{\rm UV}=-17$. Interestingly, we find that this quantity *follows* the observed extrapolation at $z>9$. This hints that whatever new physical processes are in play at these epochs may primarily affect bright galaxies, though the uncertainty in the integrated specific UV luminosity density at $z\gtrsim 11$ is currently high.

We discuss a variety of potential physical causes for the observed results. The high yield of spectroscopic confirmations implies that significant sample contamination is unlikely, though confirmation of a larger fraction of our galaxy sample would increase confidence in this claim. We find, based on blue colors for not only our galaxies but also galaxies at similar UV luminosities at $z=6$–9, that a significant drop in dust attenuation at earlier times is unlikely to be the dominant explanation. Rather, we find that models that implement a combination of increased SFE and/or an increased degree of bursty, stochastic star formation at these redshifts are more consistent with our observations. A change in the underlying IMF may also play a role.

We find slight evidence that the physics at play may be more important in bright galaxies than faint galaxies. Should this represent a dependence of SFE on halo mass, it would be expected to imprint signatures into a broad range of other cosmological probes. A key example is the topology of neutral hydrogen 21 cm intensity maps, where such a differential SFE effect would introduce an additional nonlinear bias in the power-spectrum analysis. This signature may be detectable with ongoing and upcoming experiments, such as the Hydrogen Epoch of Reionization Array (HERA; Liu & Parsons 2016) and the Square Kilometer Array (SKA; Thélie et al. 2023), thus providing independent cross-checks on our results.

Our results show that the abundance of bright galaxies at $z>9$ robustly exceeds expectations based on prelaunch observations. While many possibilities exist to explain these observations, each of them is directly empirically testable with a modest investment in further JWST spectroscopy. Deep NIRSpec follow-up can not only confirm the redshifts of all galaxies in this sample but also probe diagnostic emission lines for either AGN activity or the presence of very massive stars. Such observations could empirically measure the star formation histories, testing models of stochasticity. As we are still very early in the JWST mission, it is highly likely that such observations will become available in the near future, answering these key questions about star and galaxy formation at early times.

Acknowledgments

We thank Andrea Ferrara and Nathan Adams for sharing their data. We also thank Andrea Ferrara, Pawan Kumar, Om Gupta, Julian Muñoz, Chris Hayward, and Jason Sun for helpful conversations. We acknowledge that the location where this work took place, the University of Texas at Austin, sits on indigenous land. The Tonkawa lived in central Texas, and the Comanche and Apache moved through this area. We pay our respects to all the American Indian and Indigenous Peoples and communities who have been or have become a part of these lands and territories in Texas, on this piece of Turtle Island. We acknowledge support from NASA through STScI ERS award JWST-ERS-1345. P.G.P.-G. acknowledges support from grants PGC2018-093499-B-I00 and PID2022-139567NB-I00 funded by Spanish Ministerio de Ciencia e Innovación MCIN/AEI/10.13039/501100011033, FEDER, UE. R.A. acknowledges support from ANID Fondecyt 1202007.

Facility: HST (ACS, WFC3), JWST (NIRCam).

Appendix A
Table of $8.5\leqslant z\leqslant 10$ Sources

Here we include a table of galaxies in our sample at $8.5<z<9.7$, split into Tables 6 and 7.

Table 6
Summary of $8.5 \lesssim z \lesssim 9.5$ Candidate Galaxies

ID	R.A. (J2000)	Decl. (J2000)	$m_{\rm F277W}$ (mag)	M_{1500} (mag)	$\mathcal{C}_{\rm FUV}$ (mag)	$\int_7^{20} \mathcal{P}(z)$	$\Delta\chi^2$	Photometric Redshift	Spectroscopic Redshift
CEERS-13452	214.861602	52.904604	28.2	$-19.4^{+0.1}_{-0.2}$	$-0.16^{+0.11}_{-0.01}$	1.00	12.1	$9.55^{+0.78}_{-0.09}$	Nz
CEERS-76575	215.015299	52.913706	28.5	$-19.1^{+0.0}_{-0.2}$	$-0.08^{+0.09}_{-0.03}$	1.00	30.3	$9.55^{+0.33}_{-0.06}$	⋯
CEERS-100239	214.800532	52.725500	29.0	$-18.5^{+0.1}_{-0.4}$	$-0.04^{+0.14}_{-0.07}$	0.97	5.6	$9.52^{+1.05}_{-0.33}$	⋯
CEERS-26109	214.809675	52.858695	28.5	$-19.2^{+0.1}_{-0.2}$	$-0.14^{+0.15}_{-0.00}$	0.98	6.8	$9.43^{+0.78}_{-0.27}$	⋯
CEERS-91724	214.902804	52.794311	27.1	$-20.4^{+0.2}_{-0.1}$	$0.15^{+0.09}_{-0.19}$	0.92	5.1	$9.37^{+0.39}_{-0.51}$	⋯
CEERS-99689	214.802248	52.730517	28.4	$-19.1^{+0.1}_{-0.3}$	$0.17^{+0.09}_{-0.17}$	0.91	4.6	$9.34^{+1.17}_{-0.39}$	⋯
CEERS-90326	214.889422	52.793006	29.1	$-18.4^{+0.1}_{-0.3}$	$-0.10^{+0.05}_{-0.06}$	0.99	8.8	$9.25^{+0.30}_{-0.27}$	⋯
CEERS-45970	214.977355	52.926497	27.0	$-20.4^{+0.1}_{-0.1}$	$0.02^{+0.12}_{-0.07}$	1.00	27.0	$9.22^{+0.12}_{-0.15}$	⋯
CEERS-17198	214.858821	52.881221	28.5	$-18.9^{+0.0}_{-0.4}$	$0.10^{+0.00}_{-0.22}$	0.94	4.6	$9.22^{+1.32}_{-0.12}$	⋯
CEERS-88331	214.954423	52.852402	28.4	$-18.4^{+0.1}_{-0.4}$	$0.05^{+0.29}_{-0.04}$	0.99	5.4	$9.16^{+1.26}_{-0.21}$	⋯
CEERS-74442	214.958350	52.872526	28.3	$-19.5^{+0.3}_{-0.2}$	$0.04^{+0.09}_{-0.13}$	0.96	5.7	$9.13^{+1.23}_{-0.42}$	⋯
CEERS-42447	214.795552	52.767286	28.3	$-19.7^{+0.1}_{-0.1}$	$-0.15^{+0.03}_{-0.04}$	0.99	8.1	$9.13^{+0.15}_{-0.21}$	Nz
CEERS-58138	214.876471	52.844055	28.2	$-19.6^{+0.1}_{-0.1}$	$-0.18^{+0.11}_{-0.00}$	0.99	7.0	$9.10^{+0.18}_{-0.33}$	⋯
CEERS-17898	214.873638	52.887711	29.1	$-18.4^{+0.3}_{-0.1}$	$-0.04^{+0.14}_{-0.10}$	0.90	4.5	$9.07^{+0.15}_{-2.73}$	⋯
CEERS-39128	214.746942	52.747625	27.9	$-19.6^{+0.3}_{-0.2}$	$-0.16^{+0.23}_{-0.01}$	0.86	4.7	$9.07^{+0.30}_{-1.26}$	⋯
CEERS-64676	215.125148	52.986537	28.9	$-18.3^{+0.4}_{-0.2}$	$-0.02^{+0.32}_{-0.00}$	0.96	6.7	$9.01^{+0.69}_{-0.72}$	⋯
CEERS-56878	214.888127	52.858988	27.7	$-19.9^{+0.2}_{-0.1}$	$-0.15^{+0.12}_{-0.02}$	0.98	7.4	$9.01^{+0.30}_{-0.30}$	Nz
CEERS-1398	214.937205	52.965351	29.2	$-17.3^{+1.4}_{-0.3}$	$0.49^{+0.76}_{-0.05}$	0.96	4.3	$9.01^{+0.27}_{-1.53}$	⋯
CEERS-61419	214.897231	52.843854	28.1	$-19.3^{+0.1}_{-0.1}$	$0.13^{+0.04}_{-0.07}$	1.00	15.3	$8.95^{+1.65}_{-0.06}$	$8.998^{+0.001}_{-0.001}$
CEERS-5007	214.966722	52.968284	28.5	$-19.2^{+0.2}_{-0.1}$	$-0.16^{+0.11}_{-0.04}$	0.96	6.7	$8.98^{+0.27}_{-0.36}$	⋯
CEERS-47105	214.919100	52.877077	28.8	$-18.4^{+0.2}_{-0.3}$	$0.19^{+0.04}_{-0.22}$	1.00	16.1	$8.95^{+0.90}_{-0.24}$	⋯
CEERS-64887	215.059748	52.939334	27.3	$-20.1^{+0.1}_{-0.1}$	$-0.01^{+0.08}_{-0.05}$	0.99	7.8	$8.95^{+0.12}_{-0.18}$	⋯
CEERS-44441	214.968699	52.929650	26.9	$-20.7^{+0.1}_{-0.0}$	$-0.02^{+0.04}_{-0.04}$	1.00	52.6	$8.95^{+0.06}_{-0.09}$	⋯
CEERS-13388	214.846175	52.894002	28.4	$-19.5^{+0.3}_{-0.3}$	$0.08^{+0.10}_{-0.13}$	0.94	6.0	$8.95^{+1.38}_{-0.66}$	⋯
CEERS-19548	214.876146	52.880826	27.4	$-19.6^{+0.1}_{-0.1}$	$0.14^{+0.04}_{-0.06}$	1.00	64.5	$8.95^{+0.15}_{-0.24}$	⋯
CEERS-30173	214.781164	52.817432	28.0	$-19.6^{+0.2}_{-0.3}$	$-0.02^{+0.14}_{-0.01}$	1.00	16.7	$8.95^{+1.71}_{-0.36}$	⋯
CEERS-48308	214.989485	52.919175	28.2	$-19.5^{+0.1}_{-0.1}$	$-0.12^{+0.16}_{-0.02}$	0.95	6.6	$8.92^{+0.15}_{-0.36}$	⋯
CEERS-65503	215.079067	52.949637	28.6	$-19.0^{+0.2}_{-0.2}$	$0.08^{+0.07}_{-0.10}$	1.00	36.6	$8.92^{+0.39}_{-0.33}$	⋯
CEERS-78591	214.994190	52.876475	27.6	$-19.8^{+0.2}_{-0.2}$	$0.08^{+0.07}_{-0.10}$	1.00	16.2	$8.92^{+0.18}_{-0.36}$	⋯

Note. A summary of the key properties for the first half of the 55 galaxies in our sample with $8.5 \leqslant z \leqslant 9.7$. Spectroscopic redshifts come from Arrabal Haro et al. (2023b), Fujimoto et al. (2023a), Arrabal Haro et al. (2023a), Larson et al. (2023a), and Tang et al. (2023).

(This table is available in machine-readable form.)

Table 7
Summary of $8.5 \lesssim z \lesssim 9.5$ Candidate Galaxies

ID	R.A. (J2000)	Decl. (J2000)	$m_{\rm F277W}$ (mag)	M_{1500} (mag)	$\mathcal{C}_{\rm FUV}$ (mag)	$\int_7^{20} \mathcal{P}(z)$	$\Delta\chi^2$	Photometric Redshift	Spectroscopic Redshift
CEERS-6184	214.950081	52.949266	28.0	$-19.5^{+0.3}_{-0.0}$	$0.08^{+0.07}_{-0.04}$	1.00	14.3	$8.92^{+0.03}_{-0.57}$	⋯
CEERS-89895	214.885377	52.792716	27.9	$-20.0^{+0.2}_{-0.1}$	$-0.20^{+0.04}_{-0.00}$	0.97	5.6	$8.89^{+0.18}_{-0.21}$	⋯
CEERS-11960	214.907630	52.944612	29.1	$-18.7^{+0.3}_{-0.0}$	$-0.07^{+0.07}_{-0.04}$	1.00	31.9	$8.89^{+0.12}_{-0.48}$	⋯
CEERS-10545	214.997038	52.960082	28.2	$-19.6^{+0.1}_{-0.0}$	$-0.20^{+0.07}_{-0.00}$	0.99	6.6	$8.89^{+0.06}_{-0.30}$	⋯
CEERS-61381	214.901253	52.846996	28.5	$-18.7^{+0.2}_{-0.2}$	$0.30^{+0.04}_{-0.21}$	1.00	11.0	$11.29^{+0.21}_{-1.56}$	$8.881^{+0.001}_{-0.001}$
CEERS-7078	215.011708	52.988303	27.1	$-20.4^{+0.0}_{-0.1}$	$-0.10^{+0.09}_{-0.00}$	1.00	75.9	$8.98^{+0.06}_{-0.06}$	$8.876^{+0.002}_{-0.002}$
CEERS-96512	214.800253	52.749561	28.6	$-18.7^{+0.2}_{-0.2}$	$-0.07^{+0.17}_{-0.03}$	0.87	4.5	$8.83^{+0.15}_{-0.75}$	⋯
CEERS-82881	214.996399	52.854157	27.9	$-19.7^{+0.1}_{-0.1}$	$-0.06^{+0.09}_{-0.06}$	1.00	19.9	$8.83^{+0.18}_{-0.24}$	⋯
CEERS-4702	214.994404	52.989378	27.5	$-20.2^{+0.1}_{-0.0}$	$-0.07^{+0.07}_{-0.03}$	1.00	22.0	$8.98^{+0.12}_{-0.12}$	$8.809^{+0.003}_{-0.003}$
CEERS-43833	214.938642	52.911749	26.8	$-20.7^{+0.1}_{-0.0}$	$0.07^{+0.04}_{-0.06}$	1.00	80.3	$9.01^{+0.09}_{-0.09}$	$8.763^{+0.001}_{-0.001}$
CEERS-83492	215.079631	52.909565	27.8	$-19.6^{+0.0}_{-0.1}$	$-0.02^{+0.09}_{-0.08}$	1.00	22.6	$8.74^{+0.15}_{-0.18}$	⋯
CEERS-13544	214.844768	52.892103	26.6	$-20.5^{+0.0}_{-0.1}$	$0.23^{+0.00}_{-0.04}$	1.00	81.5	$8.74^{+0.12}_{-0.12}$	⋯
CEERS-43725	214.967532	52.932953	26.3	$-21.2^{+0.0}_{-0.0}$	$0.03^{+0.00}_{-0.04}$	1.00	69.2	$8.68^{+0.06}_{-0.09}$	$8.715^{+0.001}_{-0.001}$
CEERS-65379	215.137032	52.991109	28.6	$-19.0^{+0.3}_{-0.2}$	$0.06^{+0.12}_{-0.13}$	0.90	4.3	$8.71^{+0.57}_{-0.60}$	⋯
CEERS-89295	214.883206	52.794364	28.7	$-19.4^{+0.2}_{-0.1}$	$-0.19^{+0.07}_{-0.00}$	0.99	9.1	$8.71^{+0.12}_{-0.33}$	⋯
CEERS-37891	214.745310	52.753653	28.0	$-19.7^{+0.2}_{-0.1}$	$-0.19^{+0.14}_{-0.00}$	0.89	4.0	$8.68^{+0.24}_{-0.63}$	⋯
CEERS-81061	215.035392	52.890667	25.0	$-22.2^{+0.0}_{-0.0}$	$0.19^{+0.00}_{-0.04}$	1.00	104.0	$8.68^{+0.06}_{-0.03}$	$8.679^{+0.001}_{-0.001}$
CEERS-66635	215.120033	52.972564	27.3	$-20.2^{+0.1}_{-0.1}$	$-0.10^{+0.13}_{-0.03}$	1.00	28.8	$8.65^{+0.15}_{-0.18}$	⋯
CEERS-79589	214.989581	52.866557	26.5	$-20.7^{+0.1}_{-0.0}$	$0.15^{+0.04}_{-0.00}$	1.00	60.1	$8.65^{+0.12}_{-0.09}$	⋯
CEERS-81784	215.008674	52.868309	26.3	$-21.2^{+0.1}_{-0.1}$	$-0.08^{+0.10}_{-0.02}$	1.00	11.3	$8.65^{+0.12}_{-0.12}$	⋯
CEERS-25535	214.838706	52.882221	29.1	$-18.4^{+0.3}_{-0.2}$	$0.00^{+0.13}_{-0.09}$	0.98	8.2	$8.65^{+0.51}_{-0.39}$	⋯
CEERS-90671	214.961276	52.842364	28.1	$-18.8^{+0.2}_{-0.1}$	$0.15^{+0.09}_{-0.02}$	1.00	18.8	$8.68^{+0.21}_{-0.27}$	$8.638^{+0.001}_{-0.001}$
CEERS-12240	214.902237	52.939370	28.4	$-18.6^{+0.1}_{-0.4}$	$0.51^{+0.00}_{-0.43}$	1.00	23.4	$8.62^{+0.30}_{-0.21}$	⋯
CEERS-88342	214.961212	52.857134	28.7	$-18.5^{+0.4}_{-0.2}$	$0.26^{+0.11}_{-0.15}$	0.99	8.3	$8.59^{+0.51}_{-0.45}$	⋯
CEERS-61620	214.904392	52.848203	29.2	$-18.7^{+0.1}_{-0.1}$	$-0.20^{+0.00}_{-0.00}$	0.97	4.7	$8.59^{+0.15}_{-0.27}$	⋯
CEERS-88518	214.942159	52.842306	28.2	$-19.1^{+0.4}_{-0.2}$	$0.08^{+0.15}_{-0.13}$	0.97	7.0	$8.56^{+0.42}_{-0.57}$	⋯
CEERS-20174	214.885146	52.883650	28.5	$-18.8^{+0.1}_{-0.1}$	$-0.08^{+0.12}_{-0.04}$	0.89	4.8	$8.56^{+0.21}_{-0.51}$	⋯
CEERS-88437	214.943826	52.844229	27.5	$-20.1^{+0.1}_{-0.1}$	$0.04^{+0.00}_{-0.13}$	1.00	11.6	$8.53^{+0.18}_{-0.12}$	⋯
CEERS-78984	214.984209	52.866090	27.8	$-19.6^{+0.1}_{-0.1}$	$0.02^{+0.00}_{-0.05}$	1.00	30.4	$8.53^{+0.15}_{-0.15}$	⋯

Note. A summary of the key properties for the second half of the sample of galaxies in our sample with $8.5 \leqslant z \leqslant 9.7$. Spectroscopic redshifts come from Arrabal Haro et al. (2023b), Fujimoto et al. (2023a), Arrabal Haro et al. (2023a), Larson et al. (2023a), and Tang et al. (2023).

(This table is available in machine-readable form.)

Appendix B
Removed Sources

In Section 3.2 we described our visual inspection process to ensure a clean, robust sample of high-redshift galaxies. As discussed, 91 sources were removed. Here we present a table (Table 8) of these removed sources, along with 5″ cutout images in the F200W and F277W filters (Figures 14, 15, 16, 17, and 18). We also include a table of the five sources removed in Section 3.2.1: four due to having $z_{\rm spec} < 8.5$, and one with similar colors to the $z \sim 16$ candidate confirmed at $z_{\rm spec} = 4.9$ (Table 9).

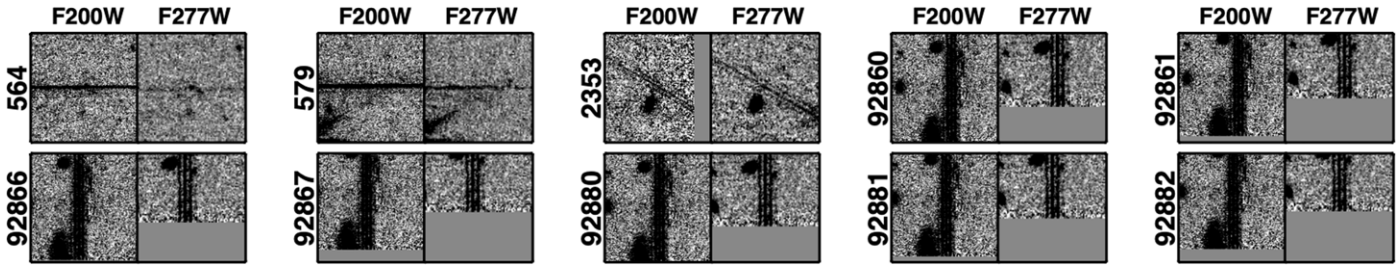

Figure 14. Cutout images, 5″ on a side, of objects originally selected, but identified via visual inspection as being diffraction spikes.

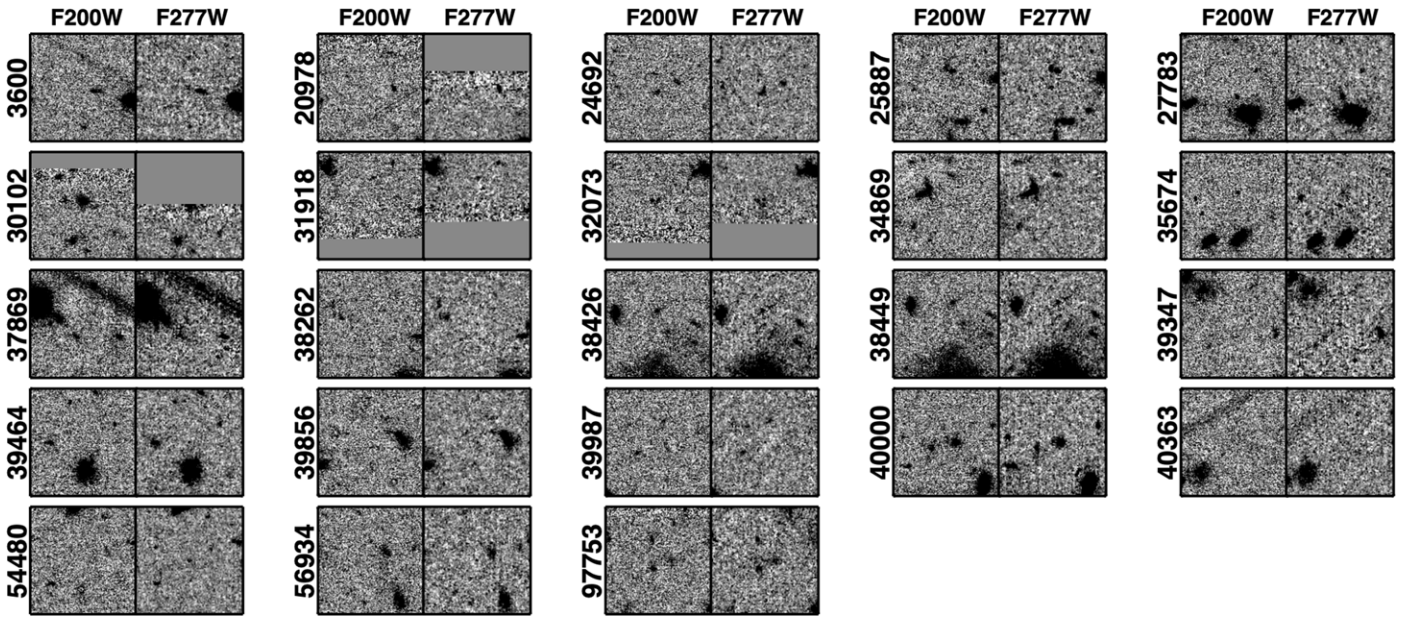

Figure 15. Same as Figure 14, but for objects identified as bad pixels.

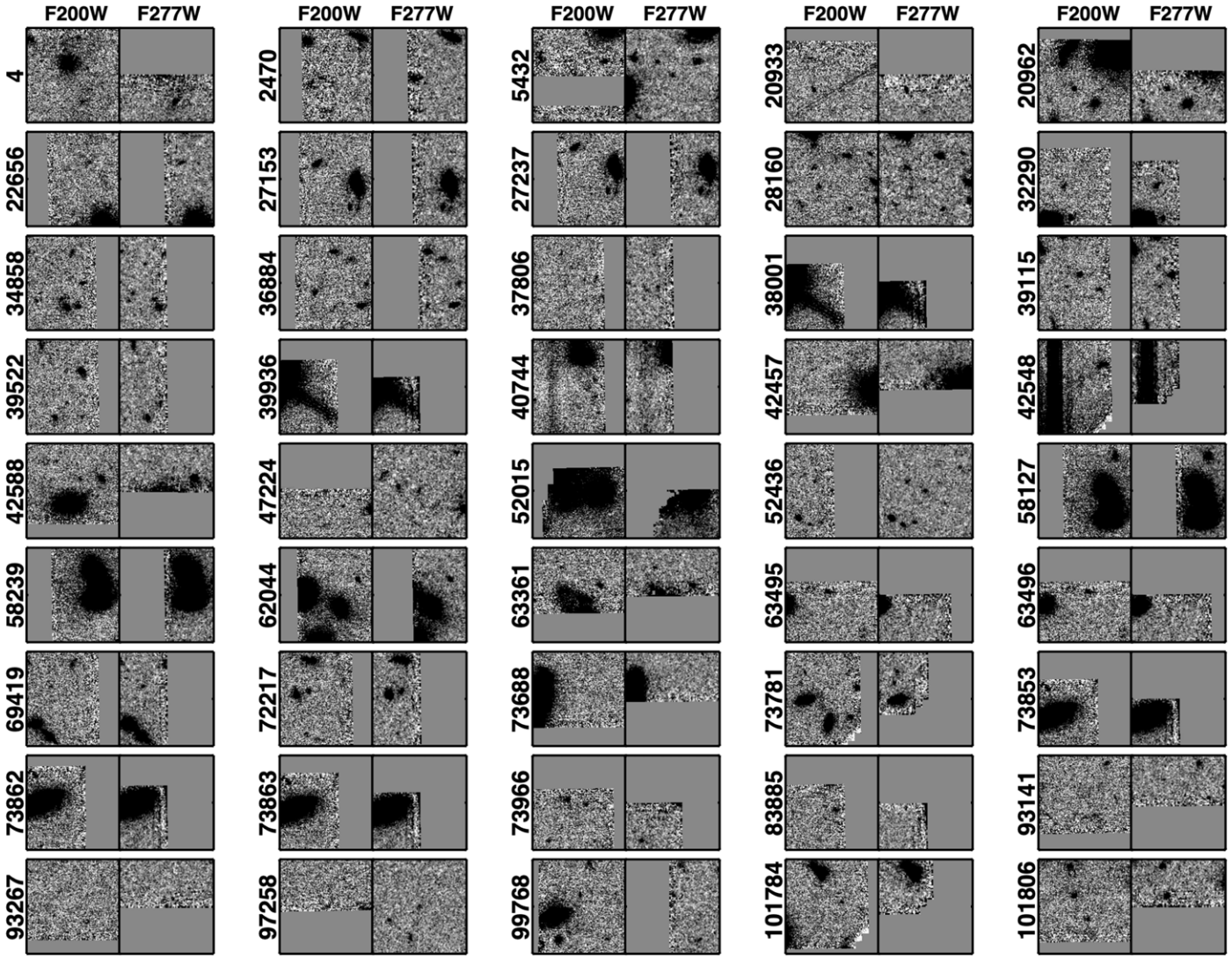

Figure 16. Same as Figure 14, but for objects identified as being associated with chip edges.

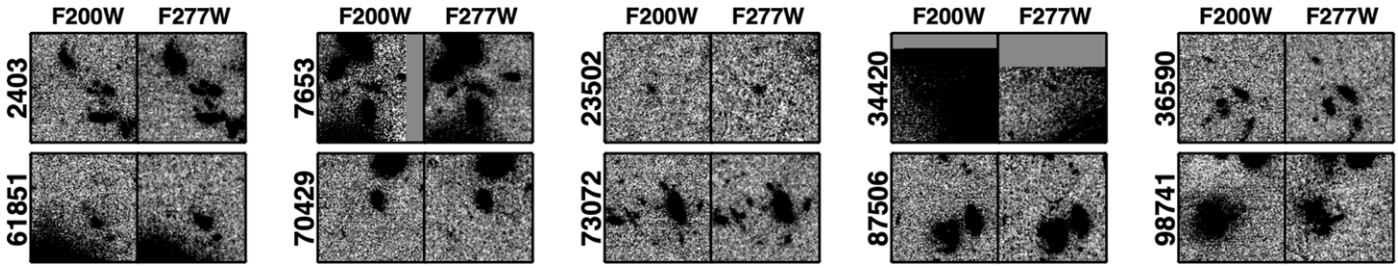

Figure 17. Same as Figure 14, but for objects identified as oversplit portions of nearby brighter galaxies.

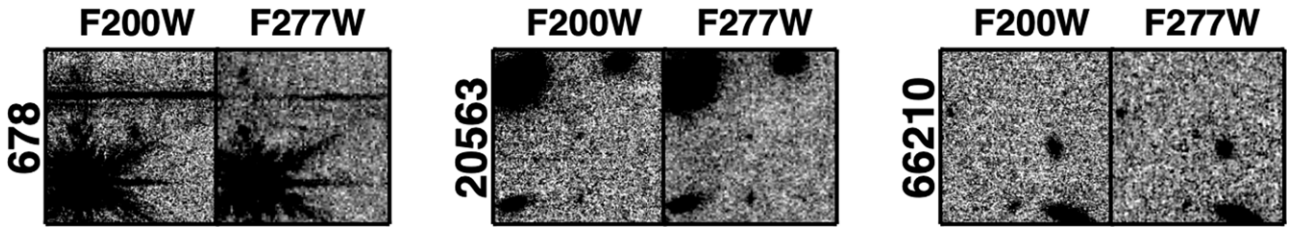

Figure 18. Same as Figure 14, but for objects identified as being affected by bad photometry.

Table 8
Objects Removed from the Sample during Visual Inspection

ID	R.A. (J2000)	Decl. (J2000)	Notes
4	214.947775	52.980444	Edge
564	215.005249	53.017773	Diffraction spike
579	215.006814	53.018834	Diffraction spike
678	215.007828	53.019061	Bad photometry (affected by diffraction spike)
2353	214.945032	52.966213	Diffraction spike
2403	215.012421	53.014295	Oversplit (possibly unique source)
2470	214.964578	52.979483	Edge
3600	214.943365	52.959006	Bad pixels(s)
5432	215.000777	52.989639	Edge
7653	215.021371	52.990815	Oversplit
20563	214.958980	52.933775	Bad photometry (flux visible in F115W)
20933	214.767704	52.854815	Edge
20962	214.735949	52.832000	Edge
20978	214.768561	52.855113	Bad pixels(s)
22656	214.780702	52.854494	Edge
23502	214.766563	52.840230	Oversplit (spurious signal near bright object)
24692	214.755849	52.827409	Bad pixels(s)
25887	214.775760	52.838390	Bad pixels(s)
27153	214.798863	52.844780	Edge
27237	214.799254	52.844685	Edge
27783	214.779457	52.827965	Bad pixels(s)
28160	214.780257	52.826895	Edge
30102	214.749567	52.841891	Bad pixels(s)
31918	214.811074	52.829806	Bad pixels(s)
32073	214.834670	52.845385	Bad pixels(s)
32290	214.743795	52.784616	Edge
34420	214.772999	52.805015	Oversplit
34858	214.755731	52.778280	Edge
34869	214.782948	52.797710	Bad pixels(s)
35674	214.766152	52.781819	Bad pixels(s) (plausibly real source)
36590	214.723366	52.746324	Oversplit
36884	214.802322	52.801134	Edge
37806	214.769166	52.771157	Edge
37869	214.783779	52.781243	Bad pixels(s)
38001	214.690385	52.748166	Edge

Table 8
(Continued)

ID	R.A. (J2000)	Decl. (J2000)	Notes
38262	214.799921	52.790796	Bad pixels(s)
38426	214.792791	52.784917	Bad pixels(s)
38449	214.793033	52.784921	Bad pixels(s)
39115	214.774698	52.768211	Edge
39347	214.792824	52.779987	Bad pixels(s)
39464	214.808944	52.790945	Bad pixels(s)
39522	214.776287	52.767365	Edge
39856	214.811602	52.791096	Bad pixels(s)
39936	214.690515	52.748090	Edge
39987	214.807915	52.787863	Bad pixels(s)
40000	214.800141	52.786022	Bad pixels(s) (plausibly real source)
40363	214.796309	52.777817	Bad pixels(s)
40744	214.780832	52.764953	Edge
42457	214.762724	52.743756	Edge
42548	214.788142	52.761069	Edge
42588	214.824026	52.786252	Edge
47224	214.982491	52.920795	Edge
52015	214.878570	52.875991	Edge
52436	214.861696	52.861844	Edge (plausibly real source)
54480	214.872931	52.859585	Bad pixels(s)
56934	214.819248	52.809749	Bad pixels(s)
58127	214.851212	52.826107	Edge
58239	214.851631	52.825884	Edge
61851	214.840216	52.801356	Oversplit
62044	214.865103	52.818660	Edge
63361	214.917040	52.847539	Edge
63495	215.092356	52.969912	Edge
63496	215.092471	52.969992	Edge
66210	215.112944	52.969707	Bad photometry (only significant flux visible in one filter)
69419	215.118348	52.955698	Edge
70429	215.152240	52.974036	Oversplit (plausibly real source)
72217	215.129726	52.949675	Edge
73072	215.108332	52.929579	Oversplit (plausibly real source)
73688	215.111283	52.928601	Edge
73781	215.136874	52.945927	Edge
73853	214.946038	52.869056	Edge
73862	214.946343	52.868885	Edge
73863	214.946212	52.868955	Edge
73966	214.999418	52.905737	Edge
83885	214.852858	52.806349	Edge
87506	214.932964	52.841802	Oversplit (plausibly real source)
92860	214.965779	52.829727	Diffraction spike
92861	214.965915	52.829654	Diffraction spike
92866	214.965694	52.829574	Diffraction spike
92867	214.965862	52.829489	Diffraction spike
92880	214.965712	52.829665	Diffraction spike
92881	214.965845	52.829598	Diffraction spike
92882	214.965961	52.829537	Diffraction spike
93141	214.915928	52.795313	Edge
93267	214.956713	52.822962	Edge
97258	214.787857	52.736119	Edge
97753	214.842961	52.771072	Bad pixels(s)
98741	214.853712	52.773300	Oversplit
99768	214.833470	52.752889	Edge
101784	214.858663	52.756439	Edge
101806	214.864006	52.760037	Edge

Note. Properties of objects removed from the sample during visual inspection. The Notes column gives the primary reason, as well as indicating which objects plausibly still could be real candidates but were conservatively removed owing to the stated concerns.

(This table is available in machine-readable form.)

Table 9
Objects Removed due to NIRSpec Information

ID	R.A. (J2000)	Decl. (J2000)	$m_{\rm F277W}$ (mag)	$\int_7^{20} \mathcal{P}(z)$	Photometric Redshift	Spectroscopic Redshift
CEERS-4774	215.005185	52.996577	27.0	0.92	$8.92^{1.35}_{0.66}$	8.005 ± 0.001
CEERS-4777	215.005366	52.996697	28.0	0.99	$10.12^{0.93}_{0.69}$	7.993 ± 0.001
CEERS-13256	214.914550	52.943023	26.5	1.00	$16.45^{0.18}_{0.45}$	4.912 ± 0.001
CEERS-23084	214.830688	52.887770	28.2	0.98	$8.77^{0.45}_{0.69}$	7.769 ± 0.003
CEERS-43382	214.951146	52.923539	28.8	0.94	$16.84^{2.34}_{0.93}$	⋯

Note. Properties of objects removed from the sample. The first four have spectroscopic redshifts of $z < 8.5$. The final object was not spectroscopically confirmed but has a photometric redshift of $z > 16$ and exhibits an observed SED extremely similar to CEERS-13256, which is confirmed by Arrabal Haro et al. (2023b) to be at $z = 4.912$.

(This table is available in machine-readable form.)

ORCID iDs

Steven L. Finkelstein https://orcid.org/0000-0001-8519-1130
Gene C. K. Leung https://orcid.org/0000-0002-9393-6507
Micaela B. Bagley https://orcid.org/0000-0002-9921-9218
Mark Dickinson https://orcid.org/0000-0001-5414-5131
Henry C. Ferguson https://orcid.org/0000-0001-7113-2738
Casey Papovich https://orcid.org/0000-0001-7503-8482
Hollis B. Akins https://orcid.org/0000-0003-3596-8794
Pablo Arrabal Haro https://orcid.org/0000-0002-7959-8783
Romeel Davé https://orcid.org/0000-0003-2842-9434
Avishai Dekel https://orcid.org/0000-0003-4174-0374
Jeyhan S. Kartaltepe https://orcid.org/0000-0001-9187-3605
Dale D. Kocevski https://orcid.org/0000-0002-8360-3880
Anton M. Koekemoer https://orcid.org/0000-0002-6610-2048
Nor Pirzkal https://orcid.org/0000-0003-3382-5941
Rachel S. Somerville https://orcid.org/0000-0002-6748-6821
L. Y. Aaron Yung https://orcid.org/0000-0003-3466-035X
Ricardo O. Amorín https://orcid.org/0000-0001-5758-1000
Bren E. Backhaus https://orcid.org/0000-0001-8534-7502
Peter Behroozi https://orcid.org/0000-0002-2517-6446
Laura Bisigello https://orcid.org/0000-0003-0492-4924
Volker Bromm https://orcid.org/0000-0003-0212-2979
Caitlin M. Casey https://orcid.org/0000-0002-0930-6466
Óscar A. Chávez Ortiz https://orcid.org/0000-0003-2332-5505
Yingjie Cheng https://orcid.org/0000-0001-8551-071X
Katherine Chworowsky https://orcid.org/0000-0003-4922-0613
Nikko J. Cleri https://orcid.org/0000-0001-7151-009X
M. C. Cooper https://orcid.org/0000-0003-1371-6019
Kelcey Davis https://orcid.org/0000-0001-8047-8351
Alexander de la Vega https://orcid.org/0000-0002-6219-5558
David Elbaz https://orcid.org/0000-0002-7631-647X
Maximilien Franco https://orcid.org/0000-0002-3560-8599
Adriano Fontana https://orcid.org/0000-0003-3820-2823
Seiji Fujimoto https://orcid.org/0000-0001-7201-5066
Mauro Giavalisco https://orcid.org/0000-0002-7831-8751
Norman A. Grogin https://orcid.org/0000-0001-9440-8872
Benne W. Holwerda https://orcid.org/0000-0002-4884-6756
Marc Huertas-Company https://orcid.org/0000-0002-1416-8483
Michaela Hirschmann https://orcid.org/0000-0002-3301-3321
Kartheik G. Iyer https://orcid.org/0000-0001-9298-3523
Shardha Jogee https://orcid.org/0000-0002-1590-0568
Intae Jung https://orcid.org/0000-0003-1187-4240
Rebecca L. Larson https://orcid.org/0000-0003-2366-8858
Ray A. Lucas https://orcid.org/0000-0003-1581-7825
Bahram Mobasher https://orcid.org/0000-0001-5846-4404
Alexa M. Morales https://orcid.org/0000-0003-4965-0402
Caroline V. Morley https://orcid.org/0000-0002-4404-0456
Sagnick Mukherjee https://orcid.org/0000-0003-1622-1302
Pablo G. Pérez-González https://orcid.org/0000-0003-4528-5639
Swara Ravindranath https://orcid.org/0000-0002-5269-6527
Giulia Rodighiero https://orcid.org/0000-0002-9415-2296
Melanie J. Rowland https://orcid.org/0000-0003-4225-6314
Sandro Tacchella https://orcid.org/0000-0002-8224-4505
Anthony J. Taylor https://orcid.org/0000-0003-1282-7454
Jonathan R. Trump https://orcid.org/0000-0002-1410-0470
Stephen M. Wilkins https://orcid.org/0000-0003-3903-6935

References

Adams, N. J., Conselice, C. J., Austin, D., et al. 2024, ApJ, 965, 169
Arrabal Haro, P., Dickinson, M., Finkelstein, S. L., et al. 2023a, ApJL, 951, L22
Arrabal Haro, P., Dickinson, M., Finkelstein, S. L., et al. 2023b, Natur, 622, 707
Bagley, M., Finkelstein, S. L., Rojas-Ruiz, S., et al. 2024a, ApJ, 961, 209
Bagley, M. B., Finkelstein, S. L., Koekemoer, A. M., et al. 2023, ApJL, 946, 12
Bagley, M. B., Pirzkal, N., Finkelstein, S. L., et al. 2024b, ApJL, 965, L6
Barro, G., Perez-Gonzalez, P. G., Kocevski, D. D., et al. 2024, ApJ, 963, 128
Behroozi, P., Conroy, C., Wechsler, R. H., et al. 2020, MNRAS, 499, 5702
Behroozi, P., Wechsler, R. H., Hearin, A. P., & Conroy, C. 2019, MNRAS, 488, 3143
Behroozi, P. S., & Silk, J. 2015, ApJ, 799, 32
Bertin, E., & Arnouts, S. 1996, A&AS, 117, 393
Bhowmick, A. K., Somerville, R. S., Di Matteo, T., et al. 2020, MNRAS, 496, 754
Bisigello, L., Gandolfi, G., Grazian, A., et al. 2023, A&A, 676, A76
Bogdan, A., Goulding, A., Natarajan, P., et al. 2024, NatAs, 8, 126
Boucaud, A., Bocchio, M., Abergel, A., et al. 2016, PyPHER: Python-based PSF Homogenization kERnels, Astrophysics Source Code Library, ascl:1609.022
Bouwens, R., Illingworth, G., Oesch, P., et al. 2023a, MNRAS, 523, 1009
Bouwens, R. J., Illingworth, G. D., Oesch, P. A., et al. 2015, ApJ, 803, 34

Bouwens, R. J., Oesch, P. A., Stefanon, M., et al. 2021, AJ, 162, 47
Bouwens, R. J., Smit, R., Schouws, S., et al. 2022, ApJ, 931, 160
Bouwens, R. J., Stefanon, M., Brammer, G., et al. 2023b, MNRAS, 523, 1036
Bouwens, R. J., Stefanon, M., Oesch, P. A., et al. 2019, ApJ, 880, 25
Bowler, R. A. A., Dunlop, J. S., McLure, R. J., et al. 2015, MNRAS, 452, 181
Bowler, R. A. A., Jarvis, M. J., Dunlop, J. S., et al. 2020, MNRAS, 493, 2059
Boyer, M. L., Anderson, J., Gennaro, M., et al. 2022, RNAAS, 6, 191
Boylan-Kolchin, M. 2023, NatAs, 7, 731
Brammer, G. B., van Dokkum, P. G., & Coppi, P. 2008, ApJ, 686, 1503
Bromm, V., Coppi, P. S., & Larson, R. B. 2002, ApJ, 564, 23
Bromm, V., Kudritzki, R. P., & Loeb, A. 2001, ApJ, 552, 464
Bruzual, G., & Charlot, S. 2003, MNRAS, 344, 1000
Bushouse, H., Eisenhamer, J., Dencheva, N., et al. 2022, JWST Calibration Pipeline, v1.6.2, Zenodo, doi:10.5281/zenodo.7041998
Calzetti, D., Kinney, A. L., & Storchi-Bergmann, T. 1994, ApJ, 429, 582
Cardelli, J. A., Clayton, G. C., & Mathis, J. S. 1989, ApJ, 345, 245
Casey, C. M., Akins, H. B., Shuntov, M., et al. 2024, ApJ, 965, 98
Casey, C. M., Kartaltepe, J. S., Drakos, N. E., et al. 2023, ApJ, 954, 31
Castellano, M., Fontana, A., Treu, T., et al. 2022, ApJL, 938, L15
Castellano, M., Fontana, A., Treu, T., et al. 2023, ApJL, 948, L14
Ciesla, L., Elbaz, D., Ilbert, O., et al. 2024, A&A, 686, A128
Cleri, N. J., Olivier, G. M., Hutchison, T. A., et al. 2023, ApJ, 953, 10
Cole, J. W., Papovich, C., Finkelstein, S. L., et al. 2023, arXiv:2312.10152
Conroy, C., & Gunn, J. E. 2010, FSPS: Flexible Stellar Population Synthesis, Astrophysics Source Code Library, ascl:1010.043
Costa, A. H., Johnson, K. E., Indebetouw, R., et al. 2021, ApJ, 918, 76
Cullen, F., McLure, R. J., McLeod, D. J., et al. 2023, MNRAS, 520, 14
Curtis-Lake, E., Carniani, S., Cameron, A., et al. 2023, NatAs, 7, 622
Davé, R., Anglés-Alcázar, D., Narayanan, D., et al. 2019, MNRAS, 486, 2827
Davis, M., Guhathakurta, P., Konidaris, N. P., et al. 2007, ApJL, 660, L1
Dayal, P., Choudhury, T. R., Bromm, V., & Pacucci, F. 2017, ApJ, 836, 16
Dekel, A., Sarkar, K. C., Birnboim, Y., Mandelker, N., & Li, Z. 2023, MNRAS, 523, 3201
Donnan, C. T., McLeod, D. J., Dunlop, J. S., et al. 2023a, MNRAS, 518, 6011
Donnan, C. T., McLeod, D. J., McLure, R. J., et al. 2023b, MNRAS, 520, 4554
Duncan, K. J., Windhorst, R. A., Koekemoer, A. M., et al. 2023, MNRAS, 522, 4548
Endsley, R., Stark, D. P., Lyu, J., et al. 2023a, MNRAS, 520, 4609
Endsley, R., Stark, D. P., Whitler, L., et al. 2023b, arXiv:2306.05295
Feng, Y., Di-Matteo, T., Croft, R. A., et al. 2016, MNRAS, 455, 2778
Ferrara, A. 2024, A&A, 684, A207
Ferrara, A., Pallottini, A., & Dayal, P. 2023, MNRAS, 522, 3986
Finkelstein, S. L. 2016, PASA, 33, e037
Finkelstein, S. L., Bagley, M., Song, M., et al. 2022a, ApJ, 928, 52
Finkelstein, S. L., & Bagley, M. B. 2022, ApJ, 938, 25
Finkelstein, S. L., Bagley, M. B., Arrabal Haro, P., et al. 2022b, ApJL, 940, L55
Finkelstein, S. L., Bagley, M. B., Ferguson, H. C., et al. 2023, ApJL, 946, L13
Finkelstein, S. L., D'Aloisio, A., Paardekooper, J.-P., et al. 2019, ApJ, 879, 36
Finkelstein, S. L., Papovich, C., Dickinson, M., et al. 2013, Natur, 502, 524
Finkelstein, S. L., Papovich, C., Giavalisco, M., et al. 2010, ApJ, 719, 1250
Finkelstein, S. L., Ryan, R. E., Jr, Papovich, C., et al. 2015, ApJ, 810, 71
Fontanot, F. 2014, MNRAS, 442, 3138
Franco, M., Akins, H. B., Casey, C. M., et al. 2023, arXiv:2308.00751
Fujimoto, S., Arrabal Haro, P., Dickinson, M., et al. 2023a, ApJL, 949, L25
Fujimoto, S., Brammer, G. B., Watson, D., et al. 2022, Natur, 604, 261
Fujimoto, S., Wang, B., Weaver, J., et al. 2023b, arXiv:2308.11609
Furtak, L. J., Labbé, I., Zitrin, A., et al. 2024, Natur, 628, 57
Gawiser, E., van Dokkum, P. G., Herrera, D., et al. 2006, ApJS, 162, 1
Greene, J. E., Labbe, I., Goulding, A. D., et al. 2024, ApJ, 964, 39
Grogin, N. A., Kocevski, D. D., Faber, S. M., et al. 2011, ApJS, 197, 35
Grudić, M. Y., Boylan-Kolchin, M., Faucher-Giguère, C.-A., & Hopkins, P. F. 2020, MNRAS, 496, L127
Hainline, K. N., Johnson, B. D., Robertson, B., et al. 2024, ApJ, 964, 71
Harikane, Y., Ouchi, M., Oguri, M., et al. 2023a, ApJS, 265, 5
Harikane, Y., Zhang, Y., Nakajima, K., et al. 2023b, ApJ, 959, 39
Heintz, K. E., Watson, D., Brammer, G., et al. 2023, arXiv:2306.00647
Hoag, A., Bradač, M., Huang, K., et al. 2019, ApJ, 878, 12
Hsiao, T. Y.-Y., Abdurro'uf, Coe, D., et al. 2023, arXiv:2305.03042
Jones, E., Smith, B., Davé, R., Narayanan, D., & Li, Q. 2024, arXiv:2402.06728
Jung, I., Finkelstein, S. L., Dickinson, M., et al. 2019, ApJ, 877, 146
Jung, I., Finkelstein, S. L., Dickinson, M., et al. 2020, ApJ, 904, 144
Kannan, R., Garaldi, E., Smith, A., et al. 2022, MNRAS, 511, 4005
Kannan, R., Springel, V., Hernquist, L., et al. 2023, MNRAS, 524, 2594
Kennicutt, R. C., Jr 1998, ApJ, 498, 541
Kocevski, D. D., Onoue, M., Inayoshi, K., et al. 2023, ApJL, 954, L4
Koekemoer, A. M., Faber, S. M., Ferguson, H. C., et al. 2011, ApJS, 197, 36
Kokorev, V., Fujimoto, S., Labbe, I., et al. 2023, ApJ, 957, L7
Labbe, I., Greene, J. E., Bezanson, R., et al. 2023, arXiv:2306.07320
Lancaster, L., Ostriker, E. C., Kim, J.-G., & Kim, C.-G. 2021, ApJL, 922, L3
Larson, R. B. 1998, MNRAS, 301, 569
Larson, R. L., Finkelstein, S. L., Hutchison, T. A., et al. 2022, ApJ, 930, 104
Larson, R. L., Finkelstein, S. L., Kocevski, D. D., et al. 2023a, ApJL, 953, L29
Larson, R. L., Hutchison, T. A., Bagley, M., et al. 2023b, ApJ, 958, 141
Leung, G. C. K., Bagley, M. B., Finkelstein, S. L., et al. 2023, ApJL, 954, L46
Li, Z., Dekel, A., Sarkar, K. C., et al. 2023, arXiv:2311.14662
Liu, A., & Parsons, A. R. 2016, MNRAS, 457, 1864
Liu, B., & Bromm, V. 2022, ApJL, 937, L30
Looser, T. J., D'Eugenio, F., Maiolino, R., et al. 2023, arXiv:2306.02470
Looser, T. J., D'Eugenio, F., Maiolino, R., et al. 2024, Natur, 629, 53
Lovell, C. C., Vijayan, A. P., Thomas, P. A., et al. 2021, MNRAS, 500, 2127
Ma, X., Hopkins, P. F., Garrison-Kimmel, S., et al. 2018, MNRAS, 478, 1694
Maiolino, R., Scholtz, J., Curtis-Lake, E., et al. 2023, arXiv:2308.01230
Maiolino, R., Scholtz, J., Witstok, J., et al. 2024, Natur, 627, 59
Marley, M. S., Saumon, D., Visscher, C., et al. 2021, ApJ, 920, 85
Mason, C. A., Trenti, M., & Treu, T. 2023, MNRAS, 521, 497
Mason, C. A., Treu, T., Schmidt, K. B., et al. 2015, ApJ, 805, 79
Matthee, J., Naidu, R. P., Brammer, G., et al. 2024, ApJ, 963, 129
McLeod, D. J., Donnan, C. T., McLure, R. J., et al. 2024, MNRAS, 527, 5004
McLeod, D. J., McLure, R. J., & Dunlop, J. S. 2016, MNRAS, 459, 3812
Meisner, A. M., Schneider, A. C., Burgasser, A. J., et al. 2021, ApJ, 915, 120
Menon, S. H., Federrath, C., & Krumholz, M. R. 2023, MNRAS, 521, 5160
Mirocha, J., & Furlanetto, S. R. 2023, MNRAS, 519, 843
Momcheva, I. G., Brammer, G. B., van Dokkum, P. G., et al. 2016, ApJS, 225, 27
Morales, A. M., Finkelstein, S. L., Leung, G. C. K., et al. 2024, ApJL, 964, L24
Morishita, T., Trenti, M., Stiavelli, M., et al. 2018, ApJ, 867, 150
Morley, C. V., Mukherjee, S., Marley, M. S., et al. 2024, arXiv:2402.00758
Muñoz, J. B., Mirocha, J., Furlanetto, S., & Sabti, N. 2023, MNRAS, 526, L47
Naidu, R. P., Oesch, P. A., Setton, D. J., et al. 2022a, arXiv:2208.02794
Naidu, R. P., Oesch, P. A., van Dokkum, P., et al. 2022b, ApJL, 940, L14
Oesch, P. A., Bouwens, R. J., Illingworth, G. D., Labbé, I., & Stefanon, M. 2018, ApJ, 855, 105
Oesch, P. A., Brammer, G., van Dokkum, P. G., et al. 2016, ApJ, 819, 129
Oesch, P. A., van Dokkum, P. G., Illingworth, G. D., et al. 2015, ApJL, 804, L30
Oke, J. B., & Gunn, J. E. 1983, ApJ, 266, 713
Olivier, G. M., Berg, D. A., Chisholm, J., et al. 2022, ApJ, 938, 16
Pallottini, A., & Ferrara, A. 2023, A&A, 677, L4
Papovich, C., Cole, J. W., Yang, G., et al. 2023, ApJL, 949, L18
Peng, C. Y., Ho, L. C., Impey, C. D., & Rix, H.-W. 2002, AJ, 124, 266
Pérez-González, P. G., Barro, G., Annunziatella, M., et al. 2023a, ApJL, 946, L16
Pérez-González, P. G., Costantin, L., Langeroodi, D., et al. 2023b, ApJL, 951, L1
Planck Collaboration, Aghanim, N., Akrami, Y., et al. 2020, A&A, 641, A6
Raiter, A., Schaerer, D., & Fosbury, R. A. E. 2010, A&A, 523, A64
Renzini, A. 2023, MNRAS, 525, L117
Rodighiero, G., Bisigello, L., Iani, E., et al. 2023, MNRAS, 518, L19
Rojas-Ruiz, S., Finkelstein, S. L., Bagley, M. B., et al. 2020, ApJ, 891, 146
Ronayne, K., Papovich, C., Yang, G., et al. 2023, arXiv:2310.07766
Schaerer, D. 2003, A&A, 397, 527
Schmidt, M. 1959, ApJ, 129, 243
Shen, X., Vogelsberger, M., Boylan-Kolchin, M., Tacchella, S., & Kannan, R. 2023, MNRAS, 525, 3254
Smith, L. J., Bajaj, V., Ryon, J., & Sabbi, E. 2020, ApJ, 896, 84
Somerville, R. S., & Davé, R. 2015, ARA&A, 53, 31
Somerville, R. S., Popping, G., & Trager, S. C. 2015, MNRAS, 453, 4337
Stefanon, M., Labbé, I., Bouwens, R. J., et al. 2019, ApJ, 883, 99
Steinhardt, C. L., Kokorev, V., Rusakov, V., Garcia, E., & Sneppen, A. 2023, ApJL, 951, L40
Stevans, M. L., Shull, J. M., Danforth, C. W., & Tilton, E. M. 2014, ApJ, 794, 75
Sun, G., Faucher-Giguère, C.-A., Hayward, C. C., et al. 2023, ApJL, 955, L35
Tacchella, S., Eisenstein, D. J., Hainline, K., et al. 2023a, ApJ, 952, 74
Tacchella, S., Johnson, B. D., Robertson, B. E., et al. 2023b, MNRAS, 522, 6236
Tang, M., Stark, D. P., Chen, Z., et al. 2023, MNRAS, 526, 1657
Thélie, E., Aubert, D., Gillet, N., Hiegel, J., & Ocvirk, P. 2023, A&A, 672, A184

Topping, M. W., Stark, D. P., Endsley, R., et al. 2022, ApJ, 941, 153
Tumlinson, J. 2006, ApJ, 641, 1
Tumlinson, J., & Shull, J. M. 2000, ApJL, 528, L65
Turner, J. L., Beck, S. C., Benford, D. J., et al. 2015, Natur, 519, 331
Umeda, H., Ouchi, M., Nakajima, K., et al. 2023, arXiv:2306.00487
Vallini, L., Witstok, J., Sommovigo, L., et al. 2024, MNRAS, 527, 10
Vega-Ferrero, J., Huertas-Company, M., Costantin, L., et al. 2024, ApJ, 961, 51
Vijayan, A. P., Lovell, C. C., Wilkins, S. M., et al. 2021, MNRAS, 501, 3289
Whitler, L., Stark, D. P., Endsley, R., et al. 2024, MNRAS, 529, 855
Wilkins, S. M., Feng, Y., Di Matteo, T., et al. 2017, MNRAS, 469, 2517
Wilkins, S. M., Stanway, E. R., & Bremer, M. N. 2014, MNRAS, 439, 1038
Wilkins, S. M., Vijayan, A. P., Lovell, C. C., et al. 2023, MNRAS, 519, 3118
Wilkins, S. M., Vijayan, A. P., Lovell, C. C., et al. 2022, MNRAS, 517, 3227
Yung, L. Y. A., Somerville, R. S., Finkelstein, S. L., Popping, G., & Davé, R. 2019, MNRAS, 483, 2983
Yung, L. Y. A., Somerville, R. S., Finkelstein, S. L., Wilkins, S. M., & Gardner, J. P. 2024a, MNRAS, 527, 5929
Yung, L. Y. A., Somerville, R. S., Finkelstein, S. L., et al. 2020, MNRAS, 496, 4574
Yung, L. Y. A., Somerville, R. S., Nguyen, T., et al. 2024b, MNRAS, 530, 4868
Zackrisson, E., Rydberg, C.-E., Schaerer, D., Östlin, G., & Tuli, M. 2011, ApJ, 740, 13
Zavala, J. A., Buat, V., Casey, C. M., et al. 2023, ApJL, 943, L9
Zitrin, A., Labbé, I., Belli, S., et al. 2015, ApJL, 810, L12